Development of Gold Nanoparticles for Photodynamic Therapy

Thesis submitted in accordance with the requirements of the University of Liverpool for the degree of Doctor in Philosophy by:

Matthew David Broadbent

August 2022

Acknowledgments

I would like to extend a huge amount of gratitude to everyone who has helped and supported me during my PhD. This project has had its ups and downs but has been immensely rewarding.

Firstly, I would like state my appreciation to my supervisory team; Martin Volk and Mathias Brust. Martin has given me a huge amount of support, not only scientifically but in supporting me through the impact COVID had on my PhD. I will remember fondly our long Zoom calls during the initial lockdowns which helped to keep me sane.

I'd like to thank all the members of the Volk group over the years: Tiago, Matt Z, Matty O, Amy, Nicola, Harriet and all the other project students. Their work has contributed immensely to the direction of my project.

Thanks to all the various members of the SSRC who made coming to University entertaining, even when results were frustrating. In no particular order: Dom, Sam, Haitham, Marta, Kallum and Sean. I'd like to extend my thanks to Jamie for our scientific discussions and as well as my larger support network.

Thank you to my family for supporting me through some tumultuous times. Finally, I'd like to thank Louisa for seemingly endless support through both the experimental and writing phases of my PhD.

Contents

List of Abbreviations

PDT	Photodynamic Therapy
AuNP	Spherical Gold Nanoparticle
AuNR	Gold Nanorod
AuNP@cit	Citrate stabilised Gold Nanoparticle
AuNP@CALNN	CALNN stabilised Gold Nanoparticle
PAH	Poly(allylamine)
PSS	Poly(styrene sulfonate)
PAH-RB	Poly(allylamine)-Rose Bengal
AuNP@PAH	Poly(allylamine) stabilised Gold Nanoparticle
AuNP@PAH@PSS	Poly(styrene sulfonate)-Poly(allylamine) stabilised Gold Nanoparticle
AuNP@PAH-RB	Poly(allylamine)-Rose Bengal stabilised Gold Nanoparticle
AuNP@PAH-RB@PSS	Poly(styrene sulfonate)Poly(allylamine)-Rose Bengal stabilised Gold Nanoparticle
PEG	Polyethylene glycol
$^1O_2$	Singlet Oxygen
Φ	Quantum yield of Singlet Oxygen generation
ε	Maximum Absorption Coefficient
σ	Absorption Cross Section
A	Absorbance
N_A	Avogadro Constant
MTT	3-(4,5-dimethylthiazol-2-yl)-2,5-diphenyltetrazolium bromide
TEM	Transmission Electron Microscopy
DCS	Differential Centrifugal Sedimentation
ICP-OES	Inductively Coupled Plasma Optical Emission spectroscopy
	Single cell Inductively Coupled Plasma spectroscopy

SC-ICP	Reactive Oxygen Species
ROS	Milli-Q water
MQ-H_2O	Photosensitiser
PS	Singlet oxygen quantum yield
SOQY	

Abstract

Development of Gold Nanoparticles for Photodynamic Therapy

Matthew Broadbent

The mechanistic properties determining whether gold nanoparticle mediated light therapy in human fibroblast cells (HeLa) takes place via a photothermal or photodynamic mechanism are investigated and discussed. The effect of cell size on AuNP uptake is shown, with smaller cells taking up less gold nanoparticles, this leads to a smaller photodynamic dose and lower efficacy of treatment. A new protocol for the investigation of photodynamic efficiency had to be developed for investigating isogenic cell lines UM-SCC-1, UM-SCC-1 pBABE and UM-SCC-1 p53 WT, which have high motility. This protocol was first tested against HeLa cells using citrate-gold nanoparticles, and similar results were obtained as with the original protocol.

Due to the extremely low quantum yield for singlet oxygen photogeneration of citrate-gold nanoparticles they are difficult to apply in realistic conditions. Therefore, Gold nanoparticles were loaded with Rose Bengal via a polyelectrolyte layer-by-layer coating. These nanoparticles were characterised and applied as a photodynamic agent. Irradiation of HeLa cells containing these nanoparticles showed increased efficacy compared to citrate-gold nanoparticles, and the effect was successfully modelled to account for beam inhomogeneity, the heterogenous uptake of AuNPs and the photobleaching of Rose Bengal.

Rose Bengal loaded gold nanoparticles showed killing in a realistic cell model UM-SCC-1, directly derived from Head-and-Neck cancer cells. When used against isogenic cells lines UM-SCC-1, UM-SCC-1 pBABE (both of which lack the p53 gene, an important regulator of cell metabolism and UM-SCC-1 p53 WT (where the p53 gene has been restored), cells with p53 function were significantly more affected by $^1O_2$. This is consistent with expectations and with dye-mediated photodynamic therapy results reported in literature and confirms the importance of considering the loss of the p53 function which is often encountered in cancerous cells. However, it was also shown that the loss of the p53 function increases gold nanoparticle uptake, counterbalancing the detrimental effect on PDT efficiency.

1 Introduction

Cancer is a leading cause of mortality worldwide, with nearly 20 million cases diagnosed worldwide in 2020 and despite extensive research of new treatments there were over 10 million cancer related deaths across the world. While absolute incidence numbers are important, it is significant that from this data 20% of people will be diagnosed with cancer before the age of 75 and 10% of people will die from cancer.[1] Cancer rates continue to increase worldwide, partly due to the aging of the world population and the adoption of cancer causing behaviours in economically developing countries.[2] Due to the widespread incidence of cancer a key goal in improving worldwide health is developing effective anti-cancer treatments that not only reduce the likelihood of death but also improve treatments to increase the quality of life of patients following treatment. Despite significant investment in developing new cancer treatments and diagnostic techniques, the most used therapeutic strategies are still surgery, chemotherapy and radiotherapy.[3]

Due to the diverse nature of cancer it is important to develop various therapeutic techniques that can be used against specific cancers, as unlike for many other diseases there is no miracle treatment that can treat every cancer.

1.1 Photodynamic therapy

While light therapy has been utilised for thousands of years, photodynamic therapy (PDT) is a treatment strategy that relies on 3 main components: light, oxygen and a photosensitiser (PS).[4] A PS is able to absorb light and excite oxygen to generate reactive oxygen species (ROS) such as singlet oxygen ($^1O_2$) which have a high reactivity and can damage cellular components leading to cell death.[5]

In use against tumours, typically a PS is administered to the patient and allowed to localise to the tumour. The tumour is then illuminated with light leading to the generation of ROS and the subsequent destruction of the tumour.[6]

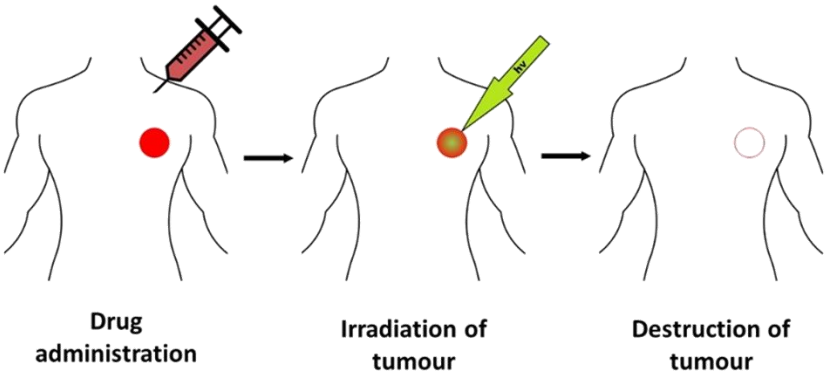

Figure 1.1 – Simplified scheme of the treatment of a tumour using photodynamic therapy. Following drug administration, it is allowed to accumulate in the tumour and is then illuminated. The combination of drug and light leads to the generation of ROS and destroys the tumour.

Cell death during PDT can occur through two major pathways: apoptosis and necrosis. Apoptosis is a programmed route of cell death that occurs following the activation of death receptors or cytochrome C. It takes advantage of pre-programmed cascades which involve the release of "executioner caspases" which lead to DNA and cell fragmentation, this genetic process is highly regulated and is a process that happens during the regular replacement of our cells.[6] Alternatively, necrosis can occur when PDT generates large amounts of ROS and significantly damages the cell. This is a violent and quick form of cell death that can be described as accidental.[7] Apoptosis is the preferred route for therapeutic cell death, since necrosis can lead to inflammation and other side effects.

1.1.1 Advantages of Photodynamic Therapy

PDT offers several advantages over conventional cancer therapies, for example, the treatment can significantly reduce long-term side effects, which can present significant improvements to the patient's quality of life after the tumour has been eliminated. In patients with lip cancer, Foscan mediated PDT treatment resulted in effective elimination of their cancer, with exceptional preservation of function and only very few side effects.[8]

Chemotherapeutic drugs intravenously delivered are unable to distinguish healthy cells other than by their replication speed, leading to extensive side effects including hair loss. In contrast, photosensitisers are not typically toxic in the absence of light,

resulting in PDT offering dual selectivity which enables treatment with minimal damage to healthy tissue. This effect arises as cell death occurs only when light and the PS are combined, either alone presents little toxicity. This allows the area of toxicity to be controlled by both the localisation of the PS and the specific application of light. PDT offers specific advantages over other treatments; it is less invasive than surgery and multiple doses can be used unlike radiotherapy.[8,9]

1.1.2 Generation of Reactive Oxygen Species

Upon illumination of the PS at an appropriate wavelength, it can be electronically excited, generating $^1PS^*$ without changing the spin before undergoing vibrational relaxation leading to a vibrationally equilibrated electronically excited state, figure 1.2. $^1PS^*$ may return to its ground state through internal conversion or fluorescence, however it may also undergo intersystem crossing leading to a triplet state $^3PS^*$ if it is kinetically and thermodynamically favourable. $^3PS^*$ may phosphoresce or release thermal energy to return to the ground state.

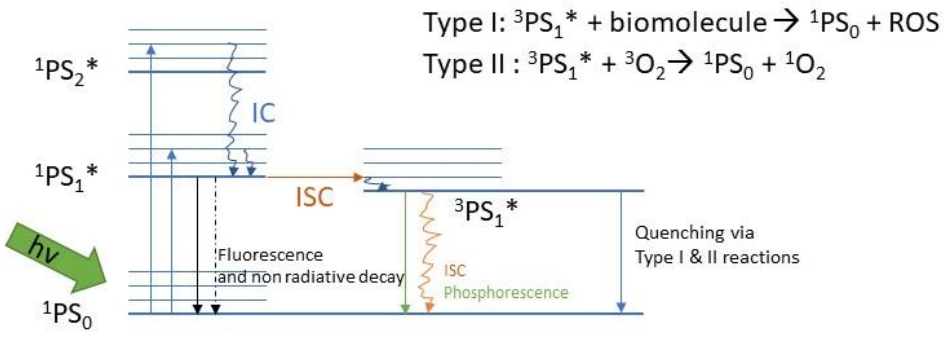

Figure 1.2 – Jablonski diagram of a typical photosensitiser PS. Upon absorption of energy, electrons are promoted to electronically excited states (remaining as singlet states), from here they can undergo internal conversion (IC) to $^1PS_1^*$. From here the PS may return to the ground state via fluorescence or non-radiative decay or may undergo intersystem crossing (ISC) to a triplet state $^3PS_1^*$. From this they may return to the ground state through phosphorescence, ISC or quenching via reaction with biomolecules or $^3O_2$ to generate ROS photodynamically.

However, as the lifetime of $^3PS^*$ typically has a μs lifespan it may be quenched by biomolecules in a type I reaction which can then react with $^3O_2$ to generate ROS such as H_2O_2, $HO^\bullet$ and $O_2^{-\bullet}$. $^3PS^*$ can also react directly with $^3O_2$ via the Dexter mechanism to generate $^1O_2$, a potent ROS which can interact with biological substrates and

induce extensive oxidative damage and subsequently cell death (type II).[5,6,10–12] Both type I and II reactions occur simultaneously, the exact ratio depends on the PS and the abundance of cellular components and $^3O_2$,; however type II is the dominant process for PDT and $^1O_2$ is the most important intermediate.[13]

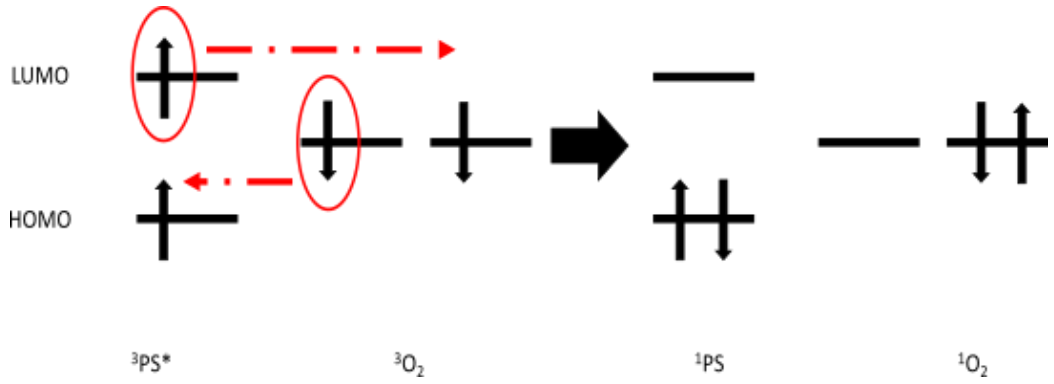

Figure 1.3 – Representative Dexter electron transfer between electronically excited PS (^{3}PS*) and molecular oxygen ($^3O_2$).

The quenching of ^{3}PS* by $^3O_2$ occurs via the Dexter electron exchange mechanism where an excited electron is transferred from a donor (^{3}PS*) to an acceptor ($^3O_2$), figure 1.3. It is a simultaneous transfer of an electron from one 2π* molecular orbital from $^3O_2$ to an unoccupied hole in ^{3}PS* and an electron with opposite spin from the excited energy level of ^{3}PS* to the other 2π* molecular orbital in $^3O_2$ as shown in figure 1.3. This returns the PS to its ground state and generates $^1O_2$ but requires overlap of wavefunctions between the donor and acceptor.[11,12]

1.1.3 Properties of $^1O_2$

The electronic structure of $^3O_2$ can be seen in figure 1.4 A and the structure of $^1O_2$ ($^1\Delta_g$)can be seen in B. While there are two singlet states of oxygen ($^1\Delta_g$ and $^1\Sigma_g^+$) that may be involved here, $^1\Sigma_g^+$ is extremely short lived and relaxes to the lower energy singlet state $^1\Delta_g$ which is commonly known as $^1O_2$.

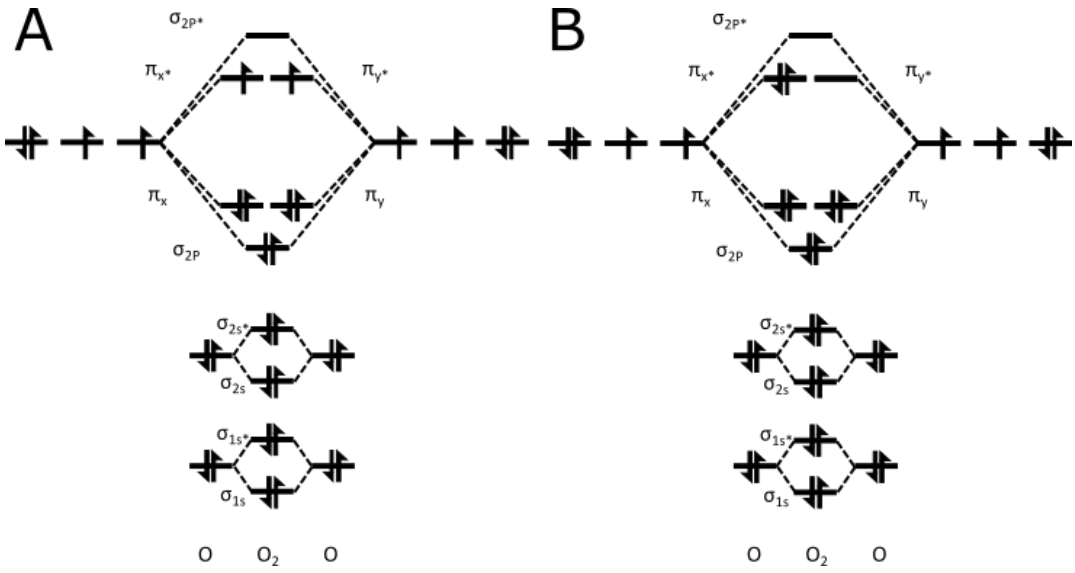

Figure 1.4 – The molecular orbital diagrams of A) Molecular oxygen $^3O_2$ ($^3\Sigma_g^-$) and B) in the singlet state $^1O_2$ ($^1\Delta_g$).

In contrast to $^3O_2$, $^1O_2$ is highly reactive and can react with nucleic acids and proteins in cells to cause cell death.[14] Its lifetime in cells is short due to the presence of biomolecules that it can react with and of H_2O which readily quenches $^1O_2$ via non-radiative electronic-vibration energy transfer due to the high frequency O-H vibrational modes. Monitoring the 1270 nm phosphorescence band presents the most useful and direct technique for determining the lifetime of $^1O_2$ in cells.[15] Studies using this measurement give a lifetime in cells of between 1-3 µs, however the actual value depends on the surrounding cellular environment.[14,16,17] The diffusion distance of $^1O_2$ before quenching in cells is estimated to be 155 nm if the lifetime is 2 µs. This has significant implications for PDT as it means that $^1O_2$ can only affect its immediate cellular surroundings.

1.1.4 Conventional Photosensitisers

The ideal PS should have the following properties: tumour localisation, chemical purity, no dark toxicity, rapid removal from the body, absorb between 630-950 nm (biological window for maximum tissue penetration), desirable subcellular localisation and a high quantum yield for ROS generation.[18,19] These requirements are well defined, however the pharmaceutical sector struggled to meet them, as combining all of these properties in an organic drug leads to significant compromises. The chemical structure of the first PS "photofrin" can be seen in figure 1.5 and was

approved for clinical use in 1999. It is a purified mixture of hematoporphyrin derivatives (HpD) and contains up to 60 porphyrin derivatives, oligomers and polymers, the exact composition is highly batch dependent. It leads to short term skin sensitivity due to poor tumour localisation, has an absorbance at 630 nm which is not ideal for tissue penetration and a low molar extinction coefficient (ε).[20]

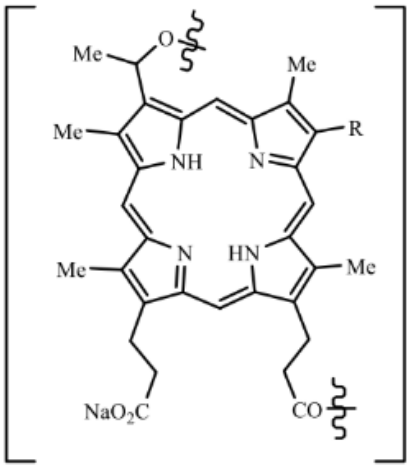

Figure 1.5 – The structure of Photofrin.

Second generation PSs are defined by their goals to reduce skin sensitivity, eliminate the mixutures found in HpDs and tailor the absorption band for better tissue penetration. Typical candidates include porphyrins (Lutex), chlorins (Foscan), pheophorbides and bacteriopheophorbides (Tookad); many of these reached clinical trials or are approved for specific cancers.[21] They have a red-shifted absorption, a larger ε and reduced biological retention times compared to Photofrin. A typical candidate developed is shown in figure 1.6, WST11 (Tookad) which has an absorption peak between 760-780 nm, a higher ε (~10^4 M^{-1} cm^{-1}) and showed quick elimination from mice.[22] Despite these advantages it was not approved for clinical use, with poor selectivity towards tumours which is a typical drawback of second generation PSs.

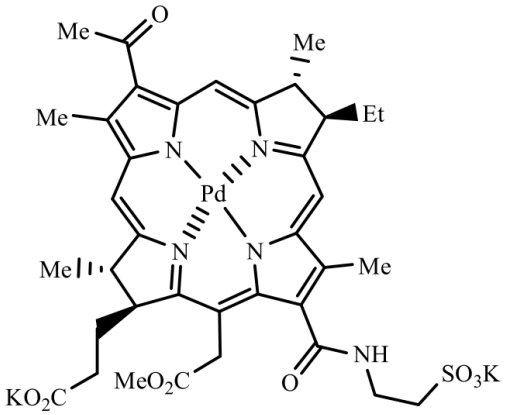

Figure 1.6 – The structure of WST11.

Third generation PSs are yet to reach fruition; however, the main goal of their development is to deliver more selective targeting of tumours to reduce side effects. Typically this involves conjugation to antibodies or encapsulation in carriers than can be delivered to target tissue.[23] Clinically used PSs have failed to take advantage of the dual selectivity due to their poor tumour localisation and suffer from critical issues including poor water-solubility, photobleaching and degradation within tumours.

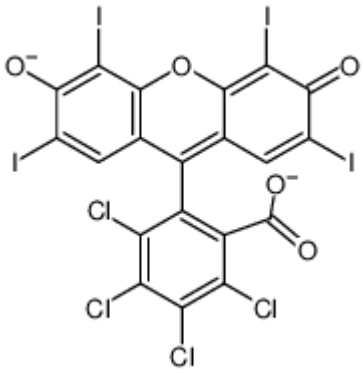

Figure 1.7 – The structure of Rose Bengal (RB).

The combined requirements of a PS preclude the use of many efficient ROS generators, a prime example of this is Rose Bengal (RB), which is used in this project. While having an excellent quantum yield of $^1O_2$ (0.75) and strong absorption between 500-600 nm (ε 80,000 M^{-1} cm^{-1}), its negative charge prevents its effective uptake in cancerous cells and therefore its use as a PS. [24–26] It is a xanthene, its structure can be seen in figure 1.7; as well as $^1O_2$ it also photogenerates superoxide radical ($O_2^{-\bullet}$),

which is another effective ROS, with a quantum yield of 0.2.[27,28] While its absorption is not in the desirable region for maximum tissue penetration, in selected applications, such as tumour bed treatment during surgery, this may be a desirable characteristic as only a thin layer of tumour cells remain above healthy tissue.[29]

1.1.5 Tumorigenesis and its Potential Impact on PDT

While many genetic changes typically occur during tumorigenesis, the loss of the p53 gene is the most common.[30] The loss of this gene means that cells shift to a Warburg metabolism, which can be defined as an increased uptake of glucose by cancerous cells which then undergoes aerobic glycolysis.[31]

There are several proposed reasons for this shift, the first was suggested by Warburg and suggests that inhibited mitochondrial function limits normal energy generation by respiration, however many tumours exhibiting the Warburg metabolism retain a substantial respiration and unaffected mitochondrial production.[32,33] Another proposal is that while aerobic glycolysis is less efficient at producing adenosine 5'-triphosphate (ATP) it is produced at a faster rate. This would give tumour cells a selective advantage when competing for shared and limited resources, and the metabolism provides rapid control of ATP production which would be beneficial for tumours.[3435] The biosynthetic requirements of uncontrolled proliferation provides another explanation: i) increased glucose consumption may be used as a carbon source for proliferation, ii) proliferating cells are in greater need of reducing equivalents and this pathway allows their increased synthesis.[36] The effect of p53 on cell signalling may also explain the shift in glucose metabolism, this includes the generation and modulation of ROS within cells.[31] Whereas normal respiration generates ROS as by-products, glycolysis increases the production of ROS modulators such as nicotinamide adenine dinucleotide phosphate and glycolosis. This can help to regulate and offset the high levels of ROS typically found in cancerous cells.[37]

As well as playing a role in the shift to a Warburg metabolism, p53 is also a part of the mechanism of apoptosis.[38] As the induction of apoptosis is a key target of PDT, the loss of p53 in cancerous cells may reduce the efficacy of this treatment. However, despite the key role it plays in apoptosis there are several p53 independent routes of

apoptosis.[39–41] Indeed, literature reports show that p53-independent apoptosis can be induced when lysosome permeabilization is present. The release of lysosomal cathepsins into the cytosol is believed to play a key role in this.[42] The use of quercitin which targets lysosome permeabilization and releases cathepsins has been shown to trigger p53-independent apoptosis.[43] While these treatments do not utilise ROS or PDT, they target lysosomes which can be a key target of PDT.

The impact of p53 status on the efficacy of PDT was first reported by Fisher in 1997, with photofrin mediated PDT showing significantly more effect in HL60 cells with WT p53 compared to HL60 cells with abrogated p53 function.[44] Further work by this group utilised two colon carcinoma cell lines that were exposed to PDT. LS513 with normal p53 function showed an increased reduction in survival upon treatment with photofrin when compared to LS1034 which has significantly reduced p53 function.[45] Other work has showed a similar effect in HT29 and human fibroblasts.[46,47] These studies used PSs that localised either in the mitochondria or endoplasmic reticulum. The survival of HEK293 treated with PDT (using 1,9-dimethyl methylene blue localised primarily in mitochondria) was reduced when p53 function was reduced, this was ascribed to reduced apoptic activity, however cell death was still observed.[48] A review of the effects of p53 on PDT was published in 2008 by Zawacka-Pankau.[38]

In head and neck cancers, over 80% of HPV negative squamous cell carcinomas of the head and neck were associated with loss of p53 function and it is the most frequent genetic event in this disease.[49] As radiation therapy is typically used to treat these cancers the effect of this mutation was studied on UM-SCC-1 and its isogenic cell lines. [50] The creation of isogenic cell lines involves changing only selected genes which allows the effect of the gene to be studied in essentially identical cell populations. In this case, p53 WT was reintroduced into UM-SCC-1 cells which do not express the p53 protein. UM-SCC-1 cells have no p53 function and show a Warburg metabolism with an increased dependence on glycolysis and reduced respiratory capacity, when p53 WT is introduced (UM-SCC-1 p53 WT) cells show reduced dependence on glycolysis and increased respiration. Radiation treatment is also mediated by ROS and so their findings could have a direct relation to the efficacy of PDT on p53 mutants. Interestingly, no significant difference was observed upon radiation alone between

UM-SCC-1 and UM-SCC-1 p53 WT, in contrast to the reports on the impact of p53 on PDT, though this may arise from the different action of radiation compared to PDT. The results show that when glycolysis is inhibited in cells containing p53 (UM-SCC-1 p53 WT), the effect of radiation does not change. However, when UM-SCC-1 cells were treated with a glycolysis inhibitor the efficacy of radiation increases. This is ascribed to the reduced capacity of cells to tolerate ROS when glycolysis is inhibited.

1.2 Gold Nanoparticles

Gold is one of the most inert chemical materials, it does not burn or oxidise in air even upon heating, and it is impervious to nearly all acids and alkalis except for selenic acid and aqua regia.[51] However, in its colloidal form it presents several desirable properties that may overcome some of the limitations associated with conventional photosensitiser both by acting alone as a PS or providing a scaffold for functionalisation. Controlled synthesis of spherical AuNPs was first reported by Turkevich *et al.* in 1951, which was then improved by Frens *et al.*[52,53]

This synthesis proceeds via the reduction of tetrachloroauric acid ($HAuCL_4$) by trisodium citrate. It allows the synthesis of AuNPs at a range of diameters between 5-120 nm depending on the ratio between $HAuCl_4$ and trisodium citrate and the reaction time. The citrate ions not only reduce the gold, but also provide stability through electrostatic binding on the surface of the AuNP providing a negatively charged layer and preventing aggregation in aqueous solution.

1.2.1 Optical Properties of AuNPs

AuNPs have a strong characteristic absorption of radiation in the visible and near-IR region of the spectrum. This arises due to the interaction of radiation with the electrons of the AuNP which causes collective oscillations of the electron cloud which is resonant with certain frequencies of light which is visually described in figure 1.8. This property is known as localised surface plasmon resonance (LSPR) which can be seen in figure 1.9, and the wavelength of radiation absorbed shifts as the size or shape of the AuNP is changed.[54]

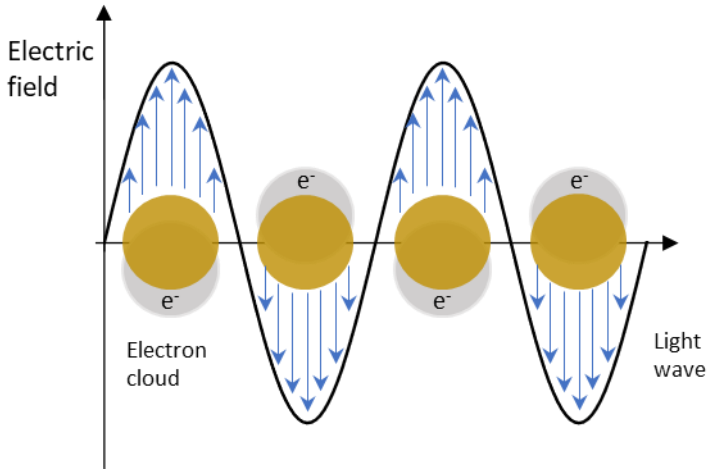

Figure 1.8 – Graphical representation of the LSPR in AuNPs when they interact with light waves.

The effects present in LSPR can be explained by the etymology; a surface plasmon is the collective oscillation of conduction electrons at the surface of metals, and the coherent oscillation is defined as surface plasmon resonance. This is quantitatively described by Mie theory and the spectra of AuNPs can be estimated if the dielectric constants of the particle and the environment are known. When the AuNP is small compared to the resonant wavelength, the external electric field is uniform. However, in larger particles the coherence of the electric field decreases, leading to multipolar plasmon oscillations and the subsequent broadened, red-shifted LSPR absorption peak. [55]

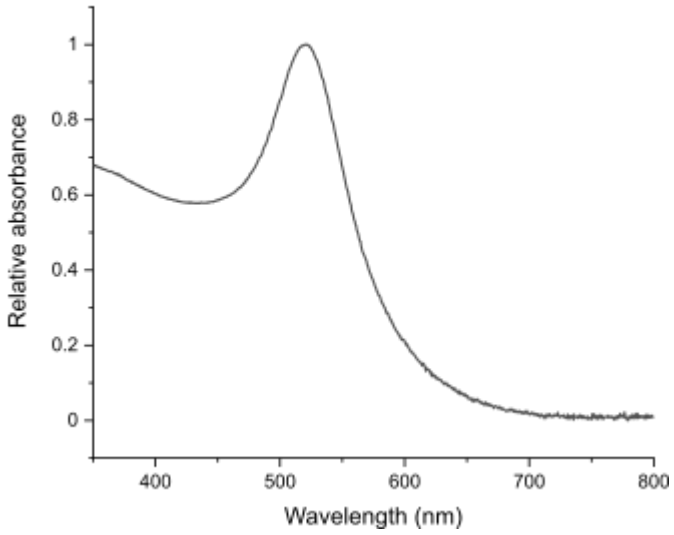

Figure 1.9 – UV-vis spectra of 13 nm AuNP@cit, the absorbance between 450-600 represents the plasmon band. In this case the peak is at 520 nm.

Another factor that can change the properties of the LSPR peak is the immediate surroundings of the nanoparticle, which is known as chemical interface damping. This effect occurs as adsorbates provide new relaxation pathways for the excited electrons, leading to broadening and redshift of the LSPR peak when AuNPs are coated.[55]

1.2.2 Generation of $^1O_2$ by AuNPs

Citrate coated gold nanoparticles (AuNP@cit) have been shown to generate singlet oxygen when illuminated with light overlapping their LSPR band.[56–59] Unlike organic dye molecules, AuNPs do not have discrete energy states rather they have an extending band of states due to the overlap of atomic orbitals of gold atoms constituting the AuNP. It is believed that this takes place through Dexter exchange energy transfer during collisions between $^3O_2$ and AuNPs leading to $^1O_2$.[57,58]

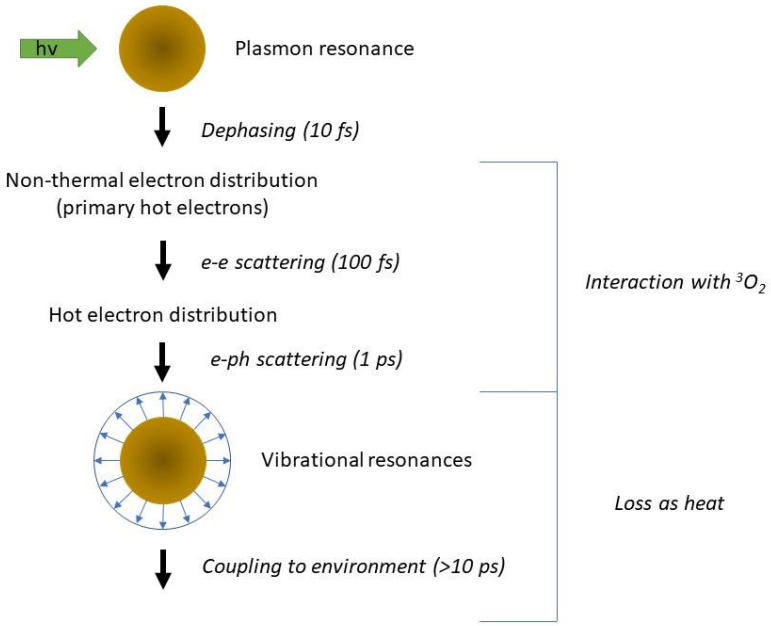

Figure 1.10 – Absorbance of radiation and its dissipation as heat and potential interaction with $^3O_2$ to form $^1O_2$, adapted from Hartland et al. and Chadwick et al.[55,57]

The processes of energy absorption and dissipation from an AuNP are shown in figure 1.10, it has been reported that the generation of $^1O_2$ takes place in either the primary hot electron phase or hot electron phase. The short lifetime (~100 fs and ~1 ps, respectively) of these phases and the short range of the Dexter mechanism leads to the exceptionally small quantum yield of singlet oxygen production (10^{-7}) reported by Entradas and Chadwick.[57,59] Despite this being significantly lower than the quantum yield of conventional PS such as Photofrin (0.89), 13 nm AuNP@cit have an ε of 10^8 M^{-1} cm^{-1} which is significantly higher than that of Photofrin (3 x 10^3 M^{-1} cm^{-1}).[21,60]

1.2.3 Surface Chemistry of AuNPs

AuNPs require stabilisation to overcome Van der Waals forces that attract nanoparticles to each other and cause aggregation. Stabilisation of nanoparticles is provided by application of capping agents to the gold surface which can be divided into three categories; steric, electrostatic and a combination of both steric and electrostatic effects.[61,62] The stabilisation of AuNP@cit is provided by citrate anions on the surface of the AuNP, this provides negative charge which creates a neutral

double layer where cations associate with the negatively charged surface. This type of stabilisation can be characterised through the measurement of the zeta-potential which measures the potential at the slipping plane.[63] Steric stabilisation arises from the association of bulky, non-ionic compounds on the surface of the nanoparticle, preventing the free association of nanoparticles. An example of this is the stabilisation of AuNPs using sulfonated polyethylene glycol (PEG), where a covalent bond is formed between the gold surface and the sulphur and the polymer chain then extrudes away from the gold core providing a dense monolayer.[64] These approaches are combined in electrosteric stabilisation, where a charged polymer known as a polyelectrolyte is added to the nanoparticle. In this case electrostatic repulsion provides long range protection, while when nanoparticles come closer there is a high local concentration of polyelectrolyte which provides steric protection.[65] Polyelectrolytes can be used to coat AuNPs in a layer-by-layer method, where oppositely charged polyelectrolytes are sequentially added to the AuNP allowing the formation of up to 20 layers. Polyallyamine (PAH) and polystyrene sulfonate (PSS) have been used in this context, with transmission electron microscopy (TEM) showing an approximate thickness of 1 nm per layer and UV-vis showing a gradual red-shift of the LSPR band as the capping layer thickness is increased.[66]

As these stabilisation strategies allow the addition of many types of compounds onto the surface of the nanoparticle, they allow the addition of desirable compounds to improve the AuNPs performance in specific applications. These include the addition of glucose and antibodies to improve the selectivity of AuNPs to tumours or the addition of therapeutic drugs or diagnostic markers utilising the AuNP as a delivery system.[67–72]

1.2.4 Uptake of AuNPs by Cells

Unlike dye molecules, AuNPs cannot cross the cell membrane directly. Instead, AuNPs are taken up via endocytosis, remain localised in endosomes and cannot enter the cytosol.[73] Briefly, this process involves the association of AuNPs to the cell membrane, a vesicle forming due to cell membrane bending, scission proteins such as clarithin cutting the membrane and loss of endocytic protein coating to leave a AuNP containing endosome, as shown in figure 1.11. This mechanism is consistent

for all nanoparticles, so other nanoparticle systems can provide useful insight to the uptake of AuNPs by cells.

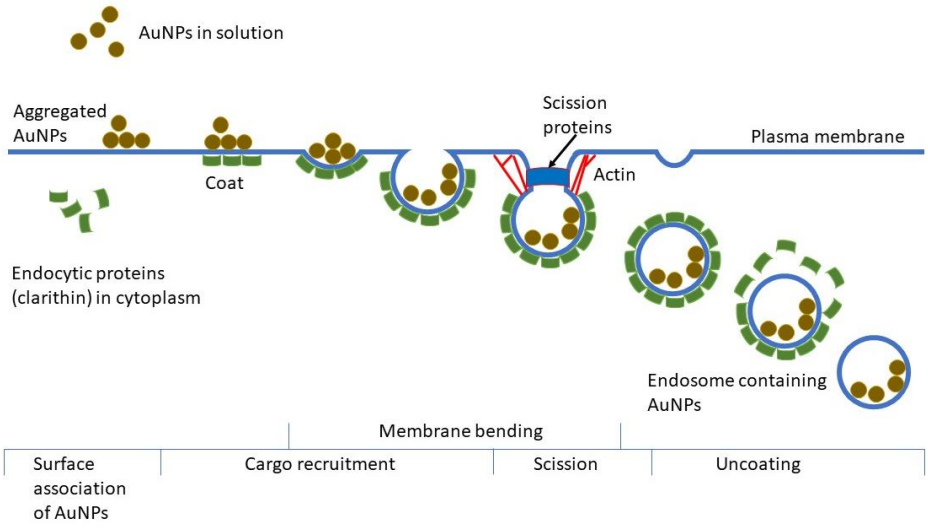

Figure 1.11 – Uptake of AuNPs via clarithin mediated endocytosis.

Upon exposure to cell culture medium (CCM) nanoparticles become coated in a protein corona, with both a "hard" chemisorbed layer and a "soft" physisorbed layer.[74] These proteins can be found in fetal bovine serum (FBS) supplemented CCM and play a key role in the uptake of nanoparticles by cells. However, the exact composition of the coronas formed by FBS remain relatively poorly characterised. Bovine serum albumin forms a chemisorbed corona through sulphur-gold bonds when incubated with AuNPs.[74] Despite it being the most abundant protein in FBS when AuNPs are exposed to CCM supplemented with FBS, it has only a partial interaction with the cell surface.[75] This result suggests that AuNPs act as concentrators of less abundant proteins through competition between high affinity proteins and suggests that the exact composition of the protein corona will change over time. The composition also depends the properties of AuNPs including: charge, hydrophobicity, shape and the presence of ligands.[76]

To study the influence of NP charge on the corona, the surface charge of silica nanoparticles was changed from positive to negative, and these NPs then were exposed to CCM containing FBS. While this changed the composition of the corona, proteins absorbed to the surface in all cases. The uptake characteristics of these nanoparticles changed significantly when non-supplemented CCM was used.

Whereas the uptake of positively charged nanoparticles was reduced by the presence of FBS, the uptake of negatively charged nanoparticles was increased significantly by the presence of FBS.[77] Due to the negative charge of cell membranes, unless a protein corona is present the association and subsequent uptake of negatively charged nanoparticles is unfavoured. For positively charged nanoparticles, the neutral corona now inhibits the association of naked nanoparticles and reduces uptake. For 10 nm AuNP@cit, the presence of the protein corona reduces the uptake compared to AuNP@cit not exposed to FBS.[78] Carnovale *et al.* showed similar results with serum coated AuNP@cit showing a reduced uptake compared to uncoated AuNP@cit in non-supplemented media.[79] Interestingly, when used in serum supplemented media their uptake was further reduced, suggesting that free serum proteins may compete with those on the surface of the AuNP@cit for cellular binding sites. However, for all biological applications CCM containing serum is the best model for cellular interactions, as these serum interactions mimic the interactions that nanoparticles have when used in vivo through their interaction with blood.

The primarily reported method of determining AuNP uptake is using inductively coupled plasma optical emission spectroscopy (ICP-OES). In this technique cells are exposed to AuNPs, washed, counted and then dissolved in aqua regia and the gold concentration is determined using ICP-OES.[73,80] This provides an excellent way of determining the average gold content of cells, however it is limited as it provides an average value and does not determine the sub-cellular localisation of AuNPs. The uptake of AuNP@cit in HeLa cells (human cervical cancer cells) has been shown to be size and shape dependent, with 50 nm AuNPs having the most uptake which then reduces as the size changes around this point. Between 10 nm and 100 nm there is still a substantial uptake of AuNP@cit, with uptake increasing as concentration and time are increased.[80] This paper also showed reduced uptake of gold nanorods (AuNR) as the aspect ratio was increased.

To see uptake mechanisms and sub-cellular localisation electron microscopy can be used. This has shown that AuNPs aggregate on the surface of the cell membrane and are then taken into intracellular vesicles including lysosomes and endosomes.[81] Unless AuNPs are functionalised with specific “cell-penetrating peptides” they are

limited to these intracellular vesicles. 3 nm AuNPs functionalised with the peptide Tat showed nuclear penetration, however as well as the correct functionalisation this delivery requires an appropriately small AuNP so that it can pass through pores in the nucleus.[82] Cell uptake can be eliminated if an appropriate PEG layer is added, such as one bearing alcohol moieties, it is likely that this layer prevents formation of a protein corona and therefore cellular association.[81] The use of the peptide CALNN, which is a good stabiliser of AuNPs, showed similar uptake to AuNP@cit.[81] Alternatively, laser scanning confocal microscopy can be used to determine the localisation of AuNPs, and polyelectrolyte coated AuNPs were shown to be taken up into cells and to remain localised within intracellular vesicles.[83] AuNRs with an exterior shell made of PAH and PSS showed uptake into cells via endocytosis and were localised in intracellular vesicles.[84]

As previously mentioned, when uptake is determined using ICP-OES only the average value of uptake is found. However, recent work using X-ray fluorescence microscopy and radiation treatment suggests that there is a high intercellular variability of gold content.[85] While the previous technique determined intercellular gold content using therapeutic effects, single-cell resolution can now be achieved directly using ICP (SC-ICP), results obtained by this technique suggests that there is a heterogeneity of AuNP uptake by cells in culture.[86–89] Wang *et al.* used a micropatterned growth surface to change the surface area of cells, and showed significantly increased uptake in larger cells, this provides an important consideration for the application of AuNPs as a PS.[89] This increased uptake agrees with work showing that population factors such as cell size impact the rate of endocytosis of viruses and may explain the heterogeneity of AuNP uptake.[90,91]

1.2.5 Biomedical Applications of AuNPs: Toxicity, Localisation, Drug Delivery

For biomedical applications it is important to establish that AuNPs show low toxicity, however current literature is conflicting. There have been reports showing no toxicity in vitro: with cysteine and citrate capped 4 nm AuNPs; glucose capped 12 nm AuNPs; citrate and cetyltrimethylammonium bromide (CTAB) capped 18 nm AuNPs showing no signs of cytotoxicity.[92] 2 nm anionic AuNPs were shown to be non-toxic in Cos-1 cells, however increasing concentrations of these AuNPs or using cationic AuNPs

showed some effect on cell viability.[93] On the other hand, CTAB coated AuNR showed limited toxicity, however it is likely that this arises from free CTAB rather than the AuNR themselves.[79] This paper also reports the toxicity of 20 nm AuNP@cit in PC-3 cells (human prostate cancer cells), interestingly when used in FBS supplemented CCM no toxicity was observed. However, at high concentrations (100 μM gold concentration) in non-supplemented CCM a small cytotoxic effect was observed. This toxicity may arise from the increased AuNP@cit uptake in these conditions. The addition of PAH and PSS coatings on CTAB coated AuNR showed a significant reduction in cytotoxicity.[84] AuNP@cit have been shown to reduce viability in HeLa cells in culture, these results varied time and AuNP concentration and showed increasing an effect as these were increased.[75] Similar results were obtained by Khan *et al.*, however it was observed that there was no increase in stress response pathways within the cells.[94] Wang *et al.* observed no apoptosis in HeLa cells exposed to AuNP@cit, however observed a reduced splitting rate so this may explain the reduced viability previously reported.[95] AuNP toxicity is dependent on the surface properties of the nanoparticles, their size and their shape. These properties also determine cellular uptake, and there is evidence to suggest that observed toxicity can be estimated by AuNP uptake.[95,96]

The toxicity of AuNPs in vivo has received increasing focus in recent years as the applications of AuNPs shifts closer to the clinic. 20 and 50 nm AuNPs were administered to mice and showed no toxicity, however showed an increase in the amount of endocytic vesicles present in endothelial tissue.[97] AuNP@cit showed high toxicity in mice when sized between 8-37 nm, however outside of this size range AuNP@cit showed no toxicity.[98] AuNPs coated in PEG showed no toxicity in mice, with 20 nm AuNP@PEG showing higher tumour uptake and slowest clearance from the body.[99] Polyelectrolyte coated AuNR (outer layer PAH) showed no toxicity in mice and were mostly localised in the liver, spleen and lungs.[84] This localisation is consistent with other AuNPs, typically accumulating in the liver and spleen.[100] For intravenous delivery surface functionalisation plays a key role in toxicity, with PEG AuNPs showing the least interaction, longest blood circulation, and least toxicity; these AuNPs are currently undergoing trials for photothermal therapy.[101]

Targeting of specific receptors that are overexpressed in tumour cell can provide active targeting and preferential uptake in the tumour when AuNPs are injected intravenously. Functionalising AuNPs with antibodies provides a promising route to maximise the benefits of dual selectivity, with several reports showing enhanced tumour uptake in AuNPs bearing overexpressed antibodies.[102–105]

A more direct method of delivery to tumours involves either intratumoral injection or topical application to the surface of the tumour. These strategies result in less exposure of healthy tissues and organs (liver and spleen) compared to intravenous injection and show reduced system toxicity.[104] Intratumoral inject showed a reasonable distribution of AuNPs throughout the tumour after injection and typically AuNPs were retained in the tumour.[106] AuNPs have been applied against canine and feline models as a photothermal agent, the AuNPs were injected intratumorally and showed no long term toxicity after 1 year.[107]

The topical application of AuNPs showed that they could penetrate the epidermis and this may present a minimally invasive delivery method.[108] The size of AuNPs plays a key role in the skin penetration, with smaller AuNPs showing superior penetration.[109] Topically applied 50 nm AuNPs functionalised with polypyrrole and rose Bengal were used topically against plantar warts, this suggests that uptake is achieved and low toxicity was observed.[110] Polyelectrolyte coated AuNPs were found to deliver imatinib mesylate through the skin, which shows that AuNPs are a promising delivery technique for delivery of anticancer agents to melanomas.[111] Fluorouracil-loaded AuNPs in creams and gels showed exceptional drug delivery using a topical application in mice and improved outcomes compared to the application of Fluorouracil alone.[112] While there are varied ways to apply AuNPs to tumours, intratumoral injections and topical application present excellent ways to minimise the toxicity and system-wide side effects of AuNPs in the body. Nevertheless, these must be assessed in more detail for specific AuNPs as their physical properties play a key role in determining toxicity.

1.2.6 AuNPs in Phototherapy

As AuNPs convert the majority of the radiation they absorb into heat, the primary focus for AuNPs in light therapy has been their use as photothermal agents.[68,113,114] These have taken advantage of the localisation of AuNPs discussed above, and the use of AuNPs for photothermal therapy has reached clinical trials.[101] As discussed in section 1.2.2 the generation of $^1O_2$ by AuNPs is relatively well established and AuNPs may function as a PS for PDT. Despite the generation of $^1O_2$ there is considerable confusion on whether cells are killed thermally or via PDT and it is widely assumed without further discussion that photothermal therapy is the main mechanism, even when light absorption is insignificant, or when elevated ROS levels are reported.[115–117]

It was reported by Krpetic *et al.* that subcellular damage to endosomes and cell death occurred following irradiation of HeLa cells containing 34,000 15 nm AuNP@cit per cell. In this experiment, cell killing could not be mediated by thermal routes as the temperature surrounding the AuNP was only raised by a fraction of a degree and the overall temperature of the cells was only raised by a few degrees over room temperature.[118] This heat independent route requires lower AuNP concentrations and/or lower light powers, more importantly, it could potentially act locally against individual cancerous cells, whereas photothermal therapy acts on larger volumes due to the fast diffusion of heat.

AuNPs have been functionalised with PSs over the last 20 years, and many strategies have been used; a review of this work was published by Calavia *et al.*[119] Self-assembled monolayers of mercaptoalkyl-PS were formed on the surface of the nanoparticle via the formation of Au-S bonds. This technique was first used by Russell *et al.* to add a Zn-phthalocyanine to AuNPs, however this AuNP was typically dissolved in ethanol and while it was effective against cells in culture, the requirement of a Cremophor emulsion prevented effective dosage in vivo.[120–122] The use of PEG by this group allowed water solubilisation and longer circulation time in blood. Increased fluorescence was observed when a shorter tether was used and increased generation of $^1O_2$ by the phthalocyanine PS which can be explained by metal-enhanced absorption.[123] This group has also shown that the addition of a EGFR

targeting peptide to these AuNPs shows active targeting of cancer cells that overexpress EGFR.[124] Other strategies involving S-Au bonds include functionalisation of AuNPs with thiolated PEGs which can then be linked to the photosensitiser, for example the attachment of Chlorin e6 to PEG-NH_2 via EDC chemistry.[125] This showed an increased uptake of Chlorin e6 when using AuNPs, and approximately 5800 PS molecules were attached to each AuNP. Interestingly this report combined the use of thermal and PDT based effects.

Polyelectrolyte coated AuNPs have been functionalised with PS, however these have mostly focussed on using electrostatic attraction, this includes the attachment of indocyanine green to 13 nm polyethyleamine coated AuNPs which suggested that 22,300 PS molecules were attached; however, much of the killing was ascribed to a photothermal method.[69] This also includes the use of the negatively charged PS $AlPcS_4$ or mTHPP which has been added to the outer layer of polyelectrolyte coatings or incorporated within the negative layers.[126–129] Rose Bengal has been coated on nanoparticles, however again these were attached electrostatically but showed PDT mediated killing in Cal-27 cells.[25,130]

1.3 Scope of this Work

This thesis covers primarily the application of AuNPs against cancerous cell lines in PDT. AuNP@cit were primarily used initially as a continuation of the work by S. Chadwick on HeLa cells; however, the use of UM-SCC-1 cells, which constitute a more realistic cancer model, required a significant change in experimental procedure and the use of lower irradiation intensities. This meant that the AuNP@cit was no longer suitable for use, so novel AuNP-polyelectrolyte-PS (AuNP@PAH-RB@PSS) were synthesised and characterised before being applied against both HeLa and UM-SCC1 cells.

Chapter 2 describes the synthesis of AuNP@cit and novel polyelectrolyte-Rose Bengal AuNPs (AuNP@PAH-RB@PSS) and their characterisation to allow determination of the loading of Rose Bengal in these AuNPs.

Chapter 3 continues the work performed by S. Chadwick, in which HeLa cells are exposed to AuNP@cit and AuNP@CALNN and subsequently irradiated with 532 cw

laser light. A new method of assessing irradiated cells was developed and the experimental data set was significantly expanded, allowing a more realistic assessment of AuNP mediated PDT and more detailed conclusions. The effect of cell area on the uptake of AuNPs was investigated, which allowed a more detailed interpretation of the experimental results. The different mechanisms of cell death (photothermal and photodynamic) are analysed; and the benefits and limitations of PS-free AuNPs discussed.

Chapter 4 presents the application of AuNP@cit and AuNP@PAH-RB@PSS to HeLa cells, using a more widely used viability assay. Instead of irradiating a small area of a large cell population, the entire population in a much smaller well was irradiated, in preparation for experiments on the much more mobile UM-SCC-1 cancer cells. This required lower intensities of light due to the increased area of irradiation, due to the low $^1O_2$ quantum yield of AuNP@cit, this necessitated the use of AuNP@PAH-RB@PSS. The uptake of AuNP@PAH-RB was determined and their photodynamic efficacy is reported.

Chapter 5 discusses the application of AuNP@cit and AUNP@PAH-RB@PSS against isogenic UM-SCC-1, UM-SCC-1 p53 WT and UM-SCC-1 pBABE cells. UM-SCC-1 is a p53 null cell line with no p53 protein expression, UM-SCC-1 p53 WT is genetically identical to UM-SCC-1 except for the reintroduction of p53 WT and UM-SC-1 pBABE is a vector control cell line. As the p53 gene is the most common mutation in cancer cells its role in determining the outcome of treatments is significant. These cell lines allow the effect of p53 status on on AuNP mediated PDT to be determined.

1.4 References

(1) Ferlay, J.; Colombet, M.; Soerjomataram, I.; Parkin, D. M.; Piñeros, M.; Znaor, A.; Bray, F. Cancer Statistics for the Year 2020: An Overview. *Int. J. Cancer* **2021**, *149* (4), 778–789. https://doi.org/10.1002/ijc.33588.

(2) Jemal, A.; Bray, F.; Ferlay, J. Global Cancer Statistics: 2011. *CA Cancer J Clin* **1999**, *49* (2), 1,33-64. https://doi.org/10.3322/caac.20107.

(3) Broekgaarden, M.; Weijer, R.; van Gulik, T. M.; Hamblin, M. R.; Heger, M. Tumor Cell Survival Pathways Activated by Photodynamic Therapy: A Molecular Basis for Pharmacological Inhibition Strategies. *Cancer Metastasis Rev.* **2015**, *34* (4), 643–690. https://doi.org/10.1007/s10555-015-9588-7.

(4) Niculescu, A. G.; Grumezescu, A. M. Photodynamic Therapy—an up-to-Date Review. *Appl. Sci.* **2021**, *11* (8), 1–18. https://doi.org/10.3390/app11083626.

(5) Correia, J. H.; Rodrigues, J. A.; Pimenta, S.; Dong, T.; Yang, Z. Photodynamic Therapy Review: Principles, Photosensitizers, Applications, and Future Directions. *Pharmaceutics* **2021**, *13* (9), 1–16. https://doi.org/10.3390/pharmaceutics13091332.

(6) Mroz, P.; Yaroslavsky, A.; Kharkwal, G. B.; Hamblin, M. R. Cell Death Pathways in Photodynamic Therapy of Cancer. *Cancers (Basel).* **2011**, *3* (2), 2516–2539. https://doi.org/10.3390/cancers3022516.

(7) Danial, N. N.; Korsmeyer, S. J. Cell Death: Critical Control Points. *Cell* **2004**, *116* (2), 205–219. https://doi.org/10.1016/S0092-8674(04)00046-7.

(8) O'Connor, A. E.; Gallagher, W. M.; Byrne, A. T. Porphyrin and Nonporphyrin Photosensitizers in Oncology: Preclinical and Clinical Advances in Photodynamic Therapy. *Photochem. Photobiol.* **2009**, *85* (5), 1053–1074. https://doi.org/10.1111/j.1751-1097.2009.00585.x.

(9) Calixto, G.; Bernegossi, J.; de Freitas, L.; Fontana, C.; Chorilli, M. Nanotechnology-Based Drug Delivery Systems for Photodynamic Therapy of Cancer: A Review. *Molecules* **2016**, *21* (3), 342. https://doi.org/10.3390/molecules21030342.

(10) Castano, A. P.; Demidova, T. N.; Hamblin, M. R. Mechanisms in Photodynamic Therapy: Part One—Photosensitizers, Photochemistry and Cellular Localization. *Photodiagnosis Photodyn. Ther.* **2004**, *1* (4), 279–293. https://doi.org/10.1016/S1572-1000(05)00007-4.

(11) Murphy, C. B.; Zhang, Y.; Troxler, T.; Ferry, V.; Martin, J. J.; Jones, W. E. Probing Förster and Dexter Energy-Transfer Mechanisms in Fluorescent Conjugated Polymer Chemosensors. *J. Phys. Chem. B* **2004**, *108* (5), 1537–1543. https://doi.org/10.1021/jp0301406.

(12) Skourtis, S. S.; Liu, C.; Antoniou, P.; Virshup, A. M.; Beratan, D. N. Dexter Energy Transfer Pathways. *Proc. Natl. Acad. Sci. U. S. A.* **2016**, *113* (29), 8115–8120. https://doi.org/10.1073/pnas.1517189113.

(13) Ding, H.; Yu, H.; Dong, Y.; Tian, R.; Huang, G.; Boothman, D. A.; Sumer, B. D.; Gao, J. Photoactivation Switch from Type II to Type I Reactions by Electron-Rich Micelles for Improved Photodynamic Therapy of Cancer Cells under Hypoxia. *J. Control. Release* **2011**, *156* (3), 276–280. https://doi.org/10.1016/j.jconrel.2011.08.019.

(14) Ogilby, P. R. Singlet Oxygen: There Is Indeed Something New under the Sun. *Chem. Soc. Rev.* **2010**, *39* (8), 3181. https://doi.org/10.1039/b926014p.

(15) Skovsen, E.; Snyder, J. W.; Lambert, J. D. C.; Ogilby, P. R. Lifetime and Diffusion of Singlet Oxygen in a Cell. *J. Phys. Chem. B* **2005**, *109* (18), 8570–8573. https://doi.org/10.1021/jp051163i.

(16) Jiménez-Banzo, A.; Sagristà, M. L.; Mora, M.; Nonell, S. Kinetics of Singlet Oxygen Photosensitization in Human Skin Fibroblasts. *Free Radic. Biol. Med.* **2008**, *44* (11), 1926–1934. https://doi.org/10.1016/j.freeradbiomed.2008.02.011.

(17) Scholz, M.; Dědic, R.; Hála, J. Microscopic Time-Resolved Imaging of Singlet Oxygen by Delayed Fluorescence in Living Cells. *Photochem. Photobiol. Sci.* **2017**, 1643–1653. https://doi.org/10.1039/C7PP00132K.

(18) Detty, M. R.; Gibson, S. L.; Wagner, S. J. Current Clinical and Preclinical Photosensitizers for Use in Photodynamic Therapy. *J. Med. Chem.* **2004**, *47* (16), 3897–3915. https://doi.org/10.1021/jm040074b.

(19) Mehraban, N.; Freeman, H. S. *Developments in PDT Sensitizers for Increased Selectivity and Singlet Oxygen Production*; 2015; Vol. 8. https://doi.org/10.3390/ma8074421.

(20) Dougherty, T. J.; Gomer, C. J.; Henderson, B. W.; Jori, G.; Kessel, D.; Korbelik, M.; Moan, J.; Peng, Q. Photodynamic Therapy. *JNCI J. Natl. Cancer Inst.* **1998**, *90* (12), 889–905. https://doi.org/10.1093/jnci/90.12.889.

(21) Ormond, A. B.; Freeman, H. S. Dye Sensitizers for Photodynamic Therapy. *Materials (Basel).* **2013**, *6* (3), 817–840. https://doi.org/10.3390/ma6030817.

(22) Mazor, O.; Brandis, A.; Plaks, V.; Neumark, E.; Rosenbach-Belkin, V.; Salomon, Y.; Scherz, A. WST11, A Novel Water-Soluble Bacteriochlorophyll Derivative; Cellular Uptake, Pharmacokinetics, Biodistribution, and Vascular Targeted Photodynamic Activity Against Melanoma Tumors. *Photochem. Photobiol.* **2004**, 342–351. https://doi.org/10.1562/2004-06-14-RA-199.

(23) Baskaran, R.; Lee, J.; Yang, S. G. Clinical Development of Photodynamic Agents and Therapeutic Applications. *Biomater. Res.* **2018**, *22*, 1–8. https://doi.org/10.1186/s40824-018-0140-z.

(24) Entradas, T.; Waldron, S.; Volk, M. The Detection Sensitivity of Commonly Used Singlet Oxygen Probes in Aqueous Environments. *J. Photochem. Photobiol. B Biol.* **2020**, *204* (October 2019), 111787. https://doi.org/10.1016/j.jphotobiol.2020.111787.

(25) Wang, B. et al. Rose-Bengal-Conjugated Gold Nanorods for Invivo

Photodynamic and Photothermal Oral Cancer Therapies. *Biomaterials* **2014**, *35* (6), 1954–1966. https://doi.org/10.1016/j.biomaterials.2013.11.066.

(26) Panzarini, E.; Tenuzzo, B.; Palazzo, F.; Chionna, A.; Dini, L. Apoptosis Induction and Mitochondria Alteration in Human HeLa Tumour Cells by Photoproducts of Rose Bengal Acetate. *J. Photochem. Photobiol. B Biol.* **2006**, *83* (1), 39–47. https://doi.org/10.1016/j.jphotobiol.2005.11.014.

(27) Lee, P. C. C.; Rodgers, M. A. J. LASER FLASH PHOTOKINETIC STUDIES OF ROSE BENGAL SENSITIZED PHOTODYNAMIC INTERACTIONS OF NUCLEOTIDES AND DNA. *Photochem. Photobiol.* **1987**, *45* (1), 79–86. https://doi.org/10.1111/j.1751-1097.1987.tb08407.x.

(28) Srinivasan, V. S.; Podolski, D.; Westrick, N. J.; Neckers, D. C. Photochemical Generation of Superoxide Ion (O2-) by Rose Bengal and Ru(Bpy)32+. *J. Am. Chem. Soc.* **1978**, *100* (20), 6513–6515. https://doi.org/10.1021/ja00488a048.

(29) Ash, C.; Dubec, M.; Donne, K.; Bashford, T. Effect of Wavelength and Beam Width on Penetration in Light-Tissue Interaction Using Computational Methods. *Lasers Med. Sci.* **2017**, *32* (8), 1909–1918. https://doi.org/10.1007/s10103-017-2317-4.

(30) Mantovani, F.; Collavin, L.; Del Sal, G. Mutant P53 as a Guardian of the Cancer Cell. *Cell Death Differ.* **2019**, *26* (2), 199–212. https://doi.org/10.1038/s41418-018-0246-9.

(31) Liberti, M. V; Locasale, J. W. The Warburg Effect: How Does It Benefit Cancer Cells? (Vol 41, Pg 211, 2016). *Trends Biochem. Sci.* **2016**, *41* (3, SI), 287. https://doi.org/10.1016/j.tibs.2016.01.004.

(32) Warburg, O. On the Origin of Cancer Cells. *Science (80-.).* **1956**, *123* (3191), 309–314. https://doi.org/10.1126/science.123.3191.309.

(33) Crabtree, H. G. Observations on the Carbohydrate Metabolism of Tumours. *Biochem. J.* **1929**, *23* (3), 536–545. https://doi.org/10.1042/bj0230536.

(34) Pfeiffer, T.; Schuster, S.; Bonhoeffer, S. Cooperation and Competition in the Evolution of ATP-Producing Pathways. *Science (80-.).* **2001**, *292* (5516), 504–507. https://doi.org/10.1126/science.1058079.

(35) Epstein, T.; Xu, L.; Gillies, R. J.; Gatenby, R. A. Separation of Metabolic Supply and Demand: Aerobic Glycolysis as a Normal Physiological Response to Fluctuating Energetic Demands in the Membrane. *Cancer Metab.* **2014**, *2* (1), 1–9. https://doi.org/10.1186/2049-3002-2-7.

(36) Vander Heiden, M. G.; Cantley, L. C.; Thompson, C. B. Understanding the Warburg Effect: The Metabolic Requirements of Cell Proliferation. *Science (80-.).* **2009**, *324* (5930), 1029–1033. https://doi.org/10.1126/science.1160809.

(37) Liou, G. Y.; Storz, P. *Reactive Oxygen Species in Cancer*; 2010; Vol. 44. https://doi.org/10.3109/10715761003667554.

(38) Zawacka-pankau, J.; Krachulec, J.; Grulkowski, I.; Bielawski, K. P.; Selivanova,

G. The P53-Mediated Cytotoxicity of Photodynamic Therapy of Cancer : Recent Advances. *Toxicol. Appl. Pharmacol.* **2008**, *232*, 487–497. https://doi.org/10.1016/j.taap.2008.07.012.

(39) Roos, W. P.; Kaina, B. DNA Damage-Induced Cell Death by Apoptosis. *Trends Mol. Med.* **2006**, *12* (9), 440–450. https://doi.org/10.1016/j.molmed.2006.07.007.

(40) Seol, D. W. P53-Independent up-Regulation of a TRAIL Receptor DR5 by Proteasome Inhibitors: A Mechanism for Proteasome Inhibitor-Enhanced TRAIL-Induced Apoptosis. *Biochem. Biophys. Res. Commun.* **2011**, *416* (1–2), 222–225. https://doi.org/10.1016/j.bbrc.2011.11.053.

(41) Fricker, M.; Papadia, S.; Hardingham, G. E.; Tolkovsky, A. M. Implication of TAp73 in the P53-Independent Pathway of Puma Induction and Puma-Dependent Apoptosis in Primary Cortical Neurons. *J. Neurochem.* **2010**, *114* (3), 772–783. https://doi.org/10.1111/j.1471-4159.2010.06804.x.

(42) Erdal, H.; Berndtsson, M.; Castro, J.; Brunk, U.; Shoshan, M. C.; Linder, S. Induction of Lysosomal Membrane Permeabilization by Compounds That Activate P53-Independent Apoptosis. *Proc. Natl. Acad. Sci. U. S. A.* **2005**, *102* (1), 192–197. https://doi.org/10.1073/pnas.0408592102.

(43) Wang, Z. X. et al. Quercetin Induces P53-Independent Cancer Cell Death through Lysosome Activation by the Transcription Factor EB and Reactive Oxygen Species-Dependent Ferroptosis. *Br. J. Pharmacol.* **2021**, *178* (5), 1133–1148. https://doi.org/10.1111/bph.15350.

(44) Fisher, A. M. R.; Danenberg, K.; Banerjee, D.; Bertino, J. R.; Danenberg, P.; Gomer, C. J. Increased Photosensitivity in HL60 Cells Expressing Wild-Type P53. *Photochem. Photobiol.* **1997**, *66* (2), 265–270. https://doi.org/10.1111/j.1751-1097.1997.tb08653.x.

(45) Fisher, A. M. R.; Rucker, N.; Wong, S.; Gomer, C. J. Differential Photosensitivity in Wild-Type and Mutant P53 Human Colon Carcinoma Cell Lines. *J. Photochem. Photobiol. B Biol.* **1998**, *42* (2), 104–107. https://doi.org/10.1016/S1011-1344(97)00130-9.

(46) Zhang, W. G.; Li, X. W.; Ma, L. P.; Wang, S. W.; Yang, H. Y.; Zhang, Z. Y. Wild-Type P53 Protein Potentiates Phototoxicity of 2-BA-2-DMHA in HT29 Cells Expressing Endogenous Mutant P53. *Cancer Lett.* **1999**, *138* (1–2), 189–195. https://doi.org/10.1016/S0304-3835(99)00013-0.

(47) Tong, Z.; Singh, G.; Rainbow, A. J. The Role of the P53 Tumor Suppressor in the Response of Human Cells to Photofrin-Mediated Photodynamic Therapy. *Photochem. Photobiol.* **2000**, *71* (2), 201. https://doi.org/10.1562/0031-8655(2000)071<0201:trotpt>2.0.co;2.

(48) Abrantes, A. B. d. P.; Dias, G. C.; Souza-Pinto, N. C.; Baptista, M. S. P53-Dependent and P53-Independent Responses of Cells Challenged by Photosensitization. *Photochem. Photobiol.* **2019**, *95* (1), 355–363. https://doi.org/10.1111/php.13019.

(49) Lawrence, M. S. et al. Comprehensive Genomic Characterization of Head and Neck Squamous Cell Carcinomas. *Nature* **2015**, *517* (7536), 576–582. https://doi.org/10.1038/nature14129.

(50) Wilkie, M. D.; Lau, A. S.; Vlatkovic, N.; Jones, T. M.; Boyd, M. T. Metabolic Signature of Squamous Cell Carcinoma of the Head and Neck : Consequences of TP53 Mutation and Therapeutic Perspectives. *Oral Oncol.* **2018**, *83* (April), 1–10. https://doi.org/10.1016/j.oraloncology.2018.05.018.

(51) Jain, S.; Hirst, D. G.; O'Sullivan, J. M. Gold Nanoparticles as Novel Agents for Cancer Therapy. *Br. J. Radiol.* **2012**, *85* (1010), 101–113. https://doi.org/10.1259/bjr/59448833.

(52) Turkevich, J.; Stevenson, P. C.; Hillier, J. A Study of the Nucleation and Growth Processes in the Synthesis of Colloidal Gold. *Discuss. Faraday Soc.* **1951**, *11* (c), 55–75. https://doi.org/10.1039/DF9511100055.

(53) Frens, G. Controlled Nucleation for the Regulation of the Particle Size in Monodisperse Gold Suspension. *Nat. Phys. Sci.* **1973**, *241*, 20–22. https://doi.org/10.1038/physci241020a0.

(54) Nehl, C. L.; Hafner, J. H. Shape-Dependent Plasmon Resonances of Gold Nanoparticles. *J. Mater. Chem.* **2008**, *18* (21), 2415. https://doi.org/10.1039/b714950f.

(55) Hartland, G. V. Optical Studies of Dynamics in Noble Metal Nanostructures. *Chem. Rev.* **2011**, *111* (6), 3858–3887. https://doi.org/10.1021/cr1002547.

(56) Vankayala, R.; Sagadevan, A.; Vijayaraghavan, P.; Kuo, C. L.; Hwang, K. C. Metal Nanoparticles Sensitize the Formation of Singlet Oxygen. *Angew. Chemie - Int. Ed.* **2011**, *50* (45), 10640–10644. https://doi.org/10.1002/anie.201105236.

(57) Chadwick, S. J.; Salah, D.; Livesey, P. M.; Brust, M.; Volk, M. Singlet Oxygen Generation by Laser Irradiation of Gold Nanoparticles. *J. Phys. Chem. C* **2016**, *120* (19), 10647–10657. https://doi.org/10.1021/acs.jpcc.6b02005.

(58) Pasparakis, G. Light-Induced Generation of Singlet Oxygen by Naked Gold Nanoparticles and Its Implications to Cancer Cell Phototherapy. *Small* **2013**, *9* (24), 4130–4134. https://doi.org/10.1002/smll.201301365.

(59) Entradas, T. Photogeneration of Singlet Oxygen by Gold Nanoparticles, PhD Thesis, University of Liverpool. **2019**.

(60) Haiss, W.; Thanh, N. T. K.; Aveyard, J.; Fernig, D. G. Determination of Size and Concentration of Gold Nanoparticles from UV-Vis Spectra. *Anal. Chem.* **2007**, *79* (11), 4215–4221. https://doi.org/10.1021/ac0702084.

(61) Pugh, R. J.; Matsunaga, T.; Fowkes, F. M. The Dispersibility and Stability of Carbon Black in Media of Low Dielectric Constant. 1. Electrostatic and Steric Contributions to Colloidal Stability. *Colloids and Surfaces* **1983**, *7* (3), 183–207. https://doi.org/10.1016/0166-6622(83)80046-8.

(62) Dumur, F.; Guerlin, A.; Dumas, E.; Bertin, D.; Gigmes, D.; Mayer, C. R.

Controlled Spontaneous Generation of Gold Nanoparticles Assisted by Dual Reducing and Capping Agents. *Gold Bull.* **2011**, *44* (2), 119–137. https://doi.org/10.1007/s13404-011-0018-5.

(63) Bhattacharjee, S. DLS and Zeta Potential - What They Are and What They Are Not? *J. Control. Release* **2016**, *235*, 337–351. https://doi.org/10.1016/j.jconrel.2016.06.017.

(64) Krpetić, Ž.; Davidson, A. M.; Volk, M.; Lévy, R.; Brust, M.; Cooper, D. L. High-Resolution Sizing of Monolayer-Protected Gold Clusters by Differential Centrifugal Sedimentation. *ACS Nano* **2013**, *7* (10), 8881–8890. https://doi.org/10.1021/nn403350v.

(65) Amina, S. J.; Guo, B. A Review on the Synthesis and Functionalization of Gold Nanoparticles as a Drug Delivery Vehicle. *Int. J. Nanomedicine* **2020**, *15*, 9823–9857. https://doi.org/10.2147/IJN.S279094.

(66) Schneider, G.; Decher, G. Functional Core/Shell Nanoparticles via Layer-by-Layer Assembly. Investigation of the Experimental Parameters for Controlling Particle Aggregation and for Enhancing Dispersion Stability. *Langmuir* **2008**, *24* (5), 1778–1789. https://doi.org/10.1021/la7021837.

(67) Motiei, M. et al. Differentiating between Cancer and Inflammation: A Metabolic-Based Method for Functional Computed Tomography Imaging. *ACS Nano* **2016**, *10* (3), 3469–3477. https://doi.org/10.1021/acsnano.5b07576.

(68) El-Sayed, I. H.; Huang, X.; El-Sayed, M. A. Selective Laser Photo-Thermal Therapy of Epithelial Carcinoma Using Anti-EGFR Antibody Conjugated Gold Nanoparticles. *Cancer Lett.* **2006**, *239* (1), 129–135. https://doi.org/10.1016/j.canlet.2005.07.035.

(69) Kuo, W. S.; Chang, Y. T.; Cho, K. C.; Chiu, K. C.; Lien, C. H.; Yeh, C. S.; Chen, S. J. Gold Nanomaterials Conjugated with Indocyanine Green for Dual-Modality Photodynamic and Photothermal Therapy. *Biomaterials* **2012**, *33* (11), 3270–3278. https://doi.org/10.1016/j.biomaterials.2012.01.035.

(70) Rogers, N. J.; Claire, S.; Harris, R. M.; Farabi, S.; Zikeli, G.; Styles, I. B.; Hodges, N. J.; Pikramenou, Z. High Coating of Ru(II) Complexes on Gold Nanoparticles for Single Particle Luminescence Imaging in Cells. *Chem. Commun.* **2014**, *50* (5), 617–619. https://doi.org/10.1039/C3CC47606E.

(71) Rogers, N. J.; Jeffery, H. C.; Claire, S.; Lewis, D. J.; Zikeli, G.; Nikolas, J. Tailoring Iridium Luminescence and Gold Nanoparticle Size for Imaging of Microvascular Blood Flow. **2017**, *12*, 2725–2740.

(72) Chen, Y. H. et al. Methotrexate Conjugated to Gold Nanoparticles Inhibits Tumor Growth in a Syngeneic Lung Tumor Model. *Mol. Pharm.* **2007**, *4* (5), 713–722. https://doi.org/10.1021/mp060132k.

(73) Lévy, R.; Shaheen, U.; Cesbron, Y.; Sée, V. Gold Nanoparticles Delivery in Mammalian Live Cells: A Critical Review. *Nano Rev.* **2010**, *1* (1), 4889. https://doi.org/10.3402/nano.v1i0.4889.

(74) Davidson, A. M.; Brust, M.; Cooper, D. L.; Volk, M. Sensitive Analysis of Protein Adsorption to Colloidal Gold by Differential Centrifugal Sedimentation. *Anal. Chem.* **2017**, *89* (12), 6807–6814. https://doi.org/10.1021/acs.analchem.7b01229.

(75) Maiorano, G.; Sabella, S.; Sorce, B.; Brunetti, V.; Malvindi, M. A.; Cingolani, R.; Pompa, P. P. Effects of Cell Culture Media on the Dynamic Formation of Protein−Nanoparticle Complexes and Influence on the Cellular Response. *ACS Nano* **2010**, *4* (12), 7481–7491. https://doi.org/10.1021/nn101557e.

(76) Tekie, F. S. M.; Hajiramezanali, M.; Geramifar, P.; Raoufi, M.; Dinarvand, R.; Soleimani, M.; Atyabi, F. Controlling Evolution of Protein Corona: A Prosperous Approach to Improve Chitosan-Based Nanoparticle Biodistribution and Half-Life. *Sci. Rep.* **2020**, *10* (1), 9664. https://doi.org/10.1038/s41598-020-66572-y.

(77) Shahabi, S.; Treccani, L.; Dringen, R.; Rezwan, K. Modulation of Silica Nanoparticle Uptake into Human Osteoblast Cells by Variation of the Ratio of Amino and Sulfonate Surface Groups: Effects of Serum. *ACS Appl. Mater. Interfaces* **2015**, *7* (25), 13821–13833. https://doi.org/10.1021/acsami.5b01900.

(78) Kruszewska, J.; Kur, A.; Kulpińska, D.; Grabowska-Jadach, I.; Matczuk, M.; Keppler, B. K.; Timerbaev, A. R.; Jarosz, M. An Improved Protocol for ICP-MS-Based Assessment of the Cellular Uptake of Metal-Based Nanoparticles. *J. Pharm. Biomed. Anal.* **2019**, *174*, 300–304. https://doi.org/10.1016/j.jpba.2019.06.006.

(79) Carnovale, C.; Bryant, G.; Shukla, R.; Bansal, V. Identifying Trends in Gold Nanoparticle Toxicity and Uptake: Size, Shape, Capping Ligand, and Biological Corona. *ACS Omega* **2019**, *4* (1), 242–256. https://doi.org/10.1021/acsomega.8b03227.

(80) Chithrani, B. D.; Ghazani, A. A.; Chan, W. C. W. Determining the Size and Shape Dependence of Gold Nanoparticle Uptake into Mammalian Cells. *Nano Lett.* **2006**, *6* (4), 662–668. https://doi.org/10.1021/nl052396o.

(81) Nativo, P.; Prior, I. a; Brust, M. Uptake and Intracellular Fate of Surface-Modified Gold Nanoparticles. *ACS Nano* **2008**, *2* (8), 1639–1644. https://doi.org/10.1021/nn800330a.

(82) De La Fuente, J. M.; Berry, C. C. Tat Peptide as an Efficient Molecule to Translocate Gold Nanoparticles into the Cell Nucleus. *Bioconjug. Chem.* **2005**, *16* (5), 1176–1180. https://doi.org/10.1021/bc050033+.

(83) Minati, L. et al. Sustained in Vitro Release and Cell Uptake of Doxorubicin Adsorbed onto Gold Nanoparticles and Covered by a Polyelectrolyte Complex Layer. *Int. J. Pharm.* **2012**, *438* (1–2), 45–52. https://doi.org/10.1016/j.ijpharm.2012.08.057.

(84) Wan, J.; Wang, J.-H.; Liu, T.; Xie, Z.; Yu, X.-F.; Li, W. Surface Chemistry but Not Aspect Ratio Mediates the Biological Toxicity of Gold Nanorods in Vitro and in

Vivo. *Sci. Rep.* **2015**, *5* (1), 11398. https://doi.org/10.1038/srep11398.

(85) Turnbull, T.; Douglass, M.; Paterson, D.; Bezak, E.; Thierry, B.; Kempson, I. Relating Intercellular Variability in Nanoparticle Uptake with Biological Consequence: A Quantitative X-Ray Fluorescence Study for Radiosensitization of Cells. *Anal. Chem.* **2015**, *87* (21), 10693–10697. https://doi.org/10.1021/acs.analchem.5b03183.

(86) Khetan, J.; Shahinuzzaman, M.; Barua, S.; Barua, D. Quantitative Analysis of the Correlation between Cell Size and Cellular Uptake of Particles. *Biophys. J.* **2019**, *116* (2), 347–359. https://doi.org/10.1016/j.bpj.2018.11.3134.

(87) Jeynes, J. C. G.; Jeynes, C.; Merchant, M. J.; Kirkby, K. J. Measuring and Modelling Cell-to-Cell Variation in Uptake of Gold Nanoparticles. *Analyst* **2013**, *138* (23), 7070. https://doi.org/10.1039/c3an01406a.

(88) Shahinuzzaman, M.; Barua, D. Dissecting Particle Uptake Heterogeneity in a Cell Population Using Bayesian Analysis. *Biophys. J.* **2020**, *118* (7), 1526–1536. https://doi.org/10.1016/j.bpj.2020.01.043.

(89) Wang, X.; Hu, X.; Li, J.; Russe, A. C. M.; Kawazoe, N.; Yang, Y.; Chen, G. Influence of Cell Size on Cellular Uptake of Gold Nanoparticles. *Biomater. Sci.* **2016**, *4* (6), 970–978. https://doi.org/10.1039/c6bm00171h.

(90) Damm, E.; Liberali, P.; Pelkmans, L.; Snijder, B.; Sacher, R.; Ra, P. Population Context Determines Cell-to-Cell Variability in Endocytosis and Virus Infection. **2009**, *461* (September). https://doi.org/10.1038/nature08282.

(91) Snijder, B.; Pelkmans, L. Origins of Regulated Cell-to-Cell Variability. *Nat. Publ. Gr.* **2011**, *12* (2), 119–125. https://doi.org/10.1038/nrm3044.

(92) Connor, E. E.; Mwamuka, J.; Gole, A.; Murphy, C. J.; Wyatt, M. D. Gold Nanoparticles Are Taken up by Human Cells but Do Not Cause Acute Cytotoxicity. *Small* **2005**, *1* (3), 325–327. https://doi.org/10.1002/smll.200400093.

(93) Goodman, C. M.; McCusker, C. D.; Yilmaz, T.; Rotello, V. M. Toxicity of Gold Nanoparticles Functionalized with Cationic and Anionic Side Chains. *Bioconjug. Chem.* **2004**, *15* (4), 897–900. https://doi.org/10.1021/bc049951i.

(94) Khan, J. A.; Pillai, B.; Das, T. K.; Singh, Y.; Maiti, S. Molecular Effects of Uptake of Gold Nanoparticles in HeLa Cells. *ChemBioChem* **2007**, *8* (11), 1237–1240. https://doi.org/10.1002/cbic.200700165.

(95) Wang, P.; Wang, X.; Wang, L.; Hou, X.; Liu, W.; Chen, C. Interaction of Gold Nanoparticles with Proteins and Cells. *Sci. Technol. Adv. Mater.* **2015**, *16* (3), 34610. https://doi.org/10.1088/1468-6996/16/3/034610.

(96) Wang, L. et al. Selective Targeting of Gold Nanorods at the Mitochondria of Cancer Cells: Implications for Cancer Therapy. *Nano Lett.* **2011**, *11* (2), 772–780. https://doi.org/10.1021/nl103992v.

(97) Rattanapinyopituk, K.; Shimada, A.; Morita, T.; Sakurai, M.; Asano, A.;

Hasegawa, T.; Inoue, K.; Takano, H. Demonstration of the Clathrin- and Caveolin-Mediated Endocytosis at the Maternal-Fetal Barrier in Mouse Placenta after Intravenous Administration of Gold Nanoparticles. *J. Vet. Med. Sci.* **2014**, *76* (3), 377–387. https://doi.org/10.1292/jvms.13-0512.

(98) Chen, Y. S.; Hung, Y. C.; Liau, I.; Huang, G. S. Assessment of the in Vivo Toxicity of Gold Nanoparticles. *Nanoscale Res. Lett.* **2009**, *4* (8), 858–864. https://doi.org/10.1007/s11671-009-9334-6.

(99) Zhang, G. et al. Influence of Anchoring Ligands and Particle Size on the Colloidal Stability and in Vivo Biodistribution of Polyethylene Glycol-Coated Gold Nanoparticles in Tumor-Xenografted Mice. *Biomaterials* **2009**, *30* (10), 1928–1936. https://doi.org/10.1016/j.biomaterials.2008.12.038.

(100) Sani, A.; Cao, C.; Cui, D. Toxicity of Gold Nanoparticles (AuNPs): A Review. *Biochem. Biophys. Reports* **2021**, *26*, 100991. https://doi.org/10.1016/j.bbrep.2021.100991.

(101) Ali, M. R. K.; Wu, Y.; El-Sayed, M. A. Gold-Nanoparticle-Assisted Plasmonic Photothermal Therapy Advances Toward Clinical Application. *J. Phys. Chem. C* **2019**, *123* (25), 15375–15393. https://doi.org/10.1021/acs.jpcc.9b01961.

(102) Marega, R. et al. Antibody-Functionalized Polymer-Coated Gold Nanoparticles Targeting Cancer Cells: An in Vitro and in Vivo Study. *J. Mater. Chem.* **2012**, *22* (39), 21305–21312. https://doi.org/10.1039/c2jm33482h.

(103) Ahmed, M.; Pan, D. W.; Davis, M. E. Lack of in Vivo Antibody Dependent Cellular Cytotoxicity with Antibody Containing Gold Nanoparticles. *Bioconjug. Chem.* **2015**, *26* (5), 812–816. https://doi.org/10.1021/acs.bioconjchem.5b00139.

(104) Chattopadhyay, N.; Fonge, H.; Cai, Z.; Scollard, D.; Lechtman, E.; Done, S. J.; Pignol, J. P.; Reilly, R. M. Role of Antibody-Mediated Tumor Targeting and Route of Administration in Nanoparticle Tumor Accumulation in Vivo. *Mol. Pharm.* **2012**, *9* (8), 2168–2179. https://doi.org/10.1021/mp300016p.

(105) Chen, J. S. et al. Functionalized Nanoparticles with Targeted Antibody to Enhance Imaging of Breast Cancer in Vivo. *J. Nanobiotechnology* **2020**, *18* (1), 1–9. https://doi.org/10.1186/s12951-020-00695-2.

(106) Laprise-Pelletier, M.; Ma, Y.; Lagueux, J.; Côté, M. F.; Beaulieu, L.; Fortin, M. A. Intratumoral Injection of Low-Energy Photon-Emitting Gold Nanoparticles: A Microdosimetric Monte Carlo-Based Model. *ACS Nano* **2018**, *12* (3), 2482–2497. https://doi.org/10.1021/acsnano.7b08242.

(107) Ali, M. R. K.; Ibrahim, I. M.; Ali, H. R.; Selim, S. A.; El-Sayed, M. A. Treatment of Natural Mammary Gland Tumors in Canines and Felines Using Gold Nanorods-Assisted Plasmonic Photothermal Therapy to Induce Tumor Apoptosis. *Int. J. Nanomedicine* **2016**, *11*, 4849–4863. https://doi.org/10.2147/IJN.S109470.

(108) Cui, M.; Wiraja, C.; Chew, S. W. T.; Xu, C. Nanodelivery Systems for Topical Management of Skin Disorders. *Mol. Pharm.* **2021**, *18* (2), 491–505.

https://doi.org/10.1021/acs.molpharmaceut.0c00154.

(109) Fernandes, R.; Smyth, N. R.; Muskens, O. L.; Nitti, S.; Heuer-Jungemann, A.; Ardern-Jones, M. R.; Kanaras, A. G. Interactions of Skin with Gold Nanoparticles of Different Surface Charge, Shape, and Functionality. *Small* **2015**, *11* (6), 713–721. https://doi.org/10.1002/smll.201401913.

(110) Fadel, M.; Fadeel, D. A.; Tawfik, A.; El-Kholy, A. I.; Mosaad, Y. O. Rose Bengal-Gold-Polypyrrole Nanoparticles as a Photothermal/Photodynamic Dual Treatment of Recalcitrant Plantar Warts: Animal and Clinical Study. *J. Drug Deliv. Sci. Technol.* **2022**, *69* (November 2021), 103095. https://doi.org/10.1016/j.jddst.2022.103095.

(111) Labala, S.; Mandapalli, P. K.; Kurumaddali, A.; Venuganti, V. V. K. Layer-by-Layer Polymer Coated Gold Nanoparticles for Topical Delivery of Imatinib Mesylate to Treat Melanoma. *Mol. Pharm.* **2015**, *12* (3), 878–888. https://doi.org/10.1021/mp5007163.

(112) Safwat, M. A.; Soliman, G. M.; Sayed, D.; Attia, M. A. Fluorouracil-Loaded Gold Nanoparticles for the Treatment of Skin Cancer: Development, in Vitro Characterization, and in Vivo Evaluation in a Mouse Skin Cancer Xenograft Model. *Mol. Pharm.* **2018**, *15* (6), 2194–2205. https://doi.org/10.1021/acs.molpharmaceut.8b00047.

(113) Hirsch, L. R. et al. Nanoshell-Mediated near-Infrared Thermal Therapy of Tumors under Magnetic Resonance Guidance. *Proc. Natl. Acad. Sci.* **2003**, *100* (23), 13549–13554. https://doi.org/10.1073/pnas.2232479100.

(114) Huang, X.; Jain, P. K.; El-Sayed, I. H.; El-Sayed, M. A. Determination of the Minimum Temperature Required for Selective Photothermal Destruction of Cancer Cells with the Use of Immunotargeted Gold Nanoparticles. *Photochem. Photobiol.* **2006**, *82* (2), 412. https://doi.org/10.1562/2005-12-14-RA-754.

(115) Guerrero-Florez, V.; Mendez-Sanchez, S. C.; Patrón-Soberano, O. A.; Rodríguez-González, V.; Blach, D.; Fernando Martínez, O. Gold Nanoparticle-Mediated Generation of Reactive Oxygen Species during Plasmonic Photothermal Therapy: A Comparative Study for Different Particle Sizes, Shapes, and Surface Conjugations. *J. Mater. Chem. B* **2020**, *8* (14), 2862–2875. https://doi.org/10.1039/d0tb00240b.

(116) Zhang, Y.; Qian, J.; Wang, D.; Wang, Y.; He, S. Multifunctional Gold Nanorods with Ultrahigh Stability and Tunability for in Vivo Fluorescence Imaging, SERS Detection, and Photodynamic Therapy. *Angew. Chemie - Int. Ed.* **2013**, *52* (4), 1148–1151. https://doi.org/10.1002/anie.201207909.

(117) Yuan, H.; Khoury, C. G.; Wilson, C. M.; Grant, G. A.; Bennett, A. J.; Vo-Dinh, T. In Vivo Particle Tracking and Photothermal Ablation Using Plasmon-Resonant Gold Nanostars. *Nanomedicine Nanotechnology, Biol. Med.* **2012**, *8* (8), 1355–1363. https://doi.org/10.1016/j.nano.2012.02.005.

(118) Krpetić, Ž.; Nativo, P.; Sée, V.; Prior, I. A.; Brust, M.; Volk, M. Inflicting Controlled Nonthermal Damage to Subcellular Structures by Laser-Activated

Gold Nanoparticles. *Nano Lett.* **2010**, *10* (11), 4549–4554. https://doi.org/10.1021/nl103142t.

(119) García Calavia, P.; Bruce, G.; Pérez-García, L.; Russell, D. A. Photosensitiser-Gold Nanoparticle Conjugates for Photodynamic Therapy of Cancer. *Photochem. Photobiol. Sci.* **2018**, *17* (11), 1534–1552. https://doi.org/10.1039/c8pp00271a.

(120) Hone, D. C.; Walker, P. I.; Evans-Gowing, R.; FitzGerald, S.; Beeby, A.; Chambrier, I.; Cook, M. J.; Russell, D. A. Generation of Cytotoxic Singlet Oxygen via Phthalocyaninel-Stabilized Gold Nanoparticles: A Potential Delivery Vehicle for Photodynamic Therapy. *Langmuir* **2002**, *18* (8), 2985–2987. https://doi.org/10.1021/la0256230.

(121) Wieder, M. E.; Hone, D. C.; Cook, M. J.; Handsley, M. M.; Gavrilovic, J.; Russell, D. A. Intracellular Photodynamic Therapy with Photosensitizer-Nanoparticle Conjugates: Cancer Therapy Using a 'Trojan Horse.' *Photochem. Photobiol. Sci.* **2006**, *5* (8), 727–734. https://doi.org/10.1039/b602830f.

(122) Camerin, M.; Magaraggia, M.; Soncin, M.; Jori, G.; Moreno, M.; Chambrier, I.; Cook, M. J.; Russell, D. A. The in Vivo Efficacy of Phthalocyanine-Nanoparticle Conjugates for the Photodynamic Therapy of Amelanotic Melanoma. *Eur. J. Cancer* **2010**, *46* (10), 1910–1918. https://doi.org/10.1016/j.ejca.2010.02.037.

(123) García Calavia, P.; Marín, M. J.; Chambrier, I.; Cook, M. J.; Russell, D. A. Towards Optimisation of Surface Enhanced Photodynamic Therapy of Breast Cancer Cells Using Gold Nanoparticle-Photosensitiser Conjugates. *Photochem. Photobiol. Sci.* **2018**, *17* (3), 281–289. https://doi.org/10.1039/c7pp00225d.

(124) Goddard, Z. R. et al. Peptide Directed Phthalocyanine-Gold Nanoparticles for Selective Photodynamic Therapy of EGFR Overexpressing Cancers. *RSC Med. Chem.* **2021**, *12* (2), 288–292. https://doi.org/10.1039/d0md00284d.

(125) Wang, S. et al. Single Continuous Wave Laser Induced Photodynamic/Plasmonic Photothermal Therapy Using Photosensitizer-Functionalized Gold Nanostars. *Adv. Mater.* **2013**, *25* (22), 3055–3061. https://doi.org/10.1002/adma.201204623.

(126) Reum, N.; Fink-Straube, C.; Klein, T.; Hartmann, R. W.; Lehr, C. M.; Schneider, M. Multilayer Coating of Gold Nanoparticles with Drug-Polymer Coadsorbates. *Langmuir* **2010**, *26* (22), 16901–16908. https://doi.org/10.1021/la103109b.

(127) Shi, Z.; Ren, W.; Gong, A.; Zhao, X.; Zou, Y.; Brown, E. M. B.; Chen, X.; Wu, A. Stability Enhanced Polyelectrolyte-Coated Gold Nanorod-Photosensitizer Complexes for High/Low Power Density Photodynamic Therapy. *Biomaterials* **2014**, *35* (25), 7058–7067. https://doi.org/10.1016/j.biomaterials.2014.04.105.

(128) Jang, B.; Park, J. Y.; Tung, C. H.; Kim, I. H.; Choi, Y. Gold Nanorod-Photosensitizer Complex for near-Infrared Fluorescence Imaging and Photodynamic/Photothermal Therapy in Vivo. *ACS Nano* **2011**, *5* (2), 1086–1094. https://doi.org/10.1021/nn102722z.

(129) Hu, Y.; Yang, Y.; Wang, H.; Du, H. Synergistic Integration of Layer-by-Layer Assembly of Photosensitizer and Gold Nanorings for Enhanced Photodynamic Therapy in the Near Infrared. *ACS Nano* **2015**, *9* (9), 8744–8754. https://doi.org/10.1021/acsnano.5b03063.

(130) Wang, J. H. et al. Bimodal Optical Diagnostics of Oral Cancer Based on Rose Bengal Conjugated Gold Nanorod Platform. *Biomaterials* **2013**, *34* (17), 4274–4283. https://doi.org/10.1016/j.biomaterials.2013.02.012.

2 Synthesis and Characterisation of AuNPs

2.1 Introduction

AuNPs can be characterised using a wide variety of techniques. Differential centrifugal sedimentation (DCS) provides an established method determining the size of the gold core and of any capping layer.[1] The LSPR can be characterised using UV-vis spectroscopy, and the surface charge of AuNPs can be determined using ζ-potential.[2,3]

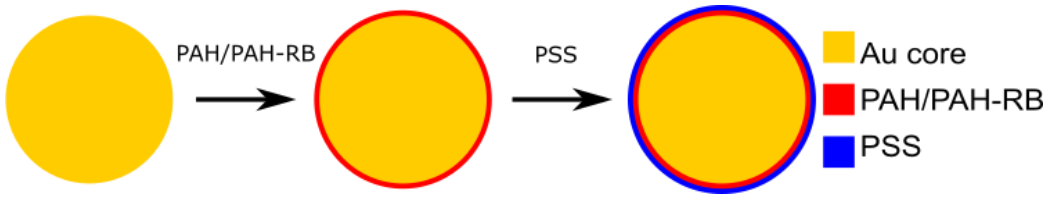

Figure 2.1 – Layer-by-layer coating of AuNP@cit using PAH or PAH/RB to create AuNP@PAH-RB/AuNP@PAH and PSS to create AuNP@PAH-RB@PSS or AuNP@PAH@PSS.

While AuNP@cit can be used as standalone PSs, they have an extremely low quantum yield of $^1O_2$ production. In order to increase the quantum yield, a PS can be attached to the surface of the AuNP. In this chapter, we attach Rose Bengal to poly(allylamine hydrochloride) using EDC chemistry as originally reported by Serrano.[4] While used in hollow microcapsules following a layer by layer synthesis, this loading technique could also be applied to AuNPs as shown in figure 2.1, and we attempt to synthesis novel AuNP@poly(allylamine)-Rose Bengal@poly(styrenesulfonate) (AuNP@PAH-RB@PSS). Layer by layer coatings of AuNPs is widely used to provide electrosteric stabilisation of AuNPs and allows the sequential loading of oppositely charged polymers known as polyelectrolytes.

2.2 Experimental

2.2.1 Materials

Gold (III) chloride trihydrate, trisodium citrate, poly(allylamine hydrochloride) (M_w~15,000), N-(-3-Dimethylaminopropyl)-N'-ethylcarbodiimide hydrochloride (EDC), sucrose, hydrochloric acid (HCl), 2-Morpholinoethanesulfonic acid monohydrate (MES), Rose Bengal (RB) and nitric acid (HNO_3) were purchased from

Sigma-Aldrich (Merck). 10,000 molecular weight cut-off dialysis tubing was purchased from Thermofisher. Poly(sodium-4-styrenesulfonate) (M_w~15,000) was purchased from Kromatek.

2.2.2 Gold Nanoparticle Preparation

Milli-Q water (>18.2 MΩ cm^{-1}) was freshly prepared using a Barnstead Smart2Pure water purification system (Thermofisher).

2.2.2.1 Citrate-coated Gold Nanoparticles (AuNP@cit)

12-15 nm AuNP@cit were synthesised by citrate mediated reduction of $HAuCl_4$ using the Turkevich-Frens method.[5]

150 mL of 0.32 mM $HAuCl_4$ solution was refluxed in a round-bottom flask with vigorous stirring for 5 minutes. 4.5 mL of 39 mM aqueous trisodium citrate was added rapidly. The colour changed from pale yellow to colourless, to deep purple and finally to ruby red. The mixture was refluxed for a further 25 minutes and allowed to cool overnight under stirring. The solution was then filtered through fluted filter paper, stored in a fridge and characterised using UV-Vis spectroscopy and differential centrifugal sedimentation.

2.2.2.2 Poly(allylamine)-coated Gold Nanoparticles (AuNP@PAH)

45.96 mg of poly(allylamine hydrochloride) (mw. 15k) (PAH) was dissolved in 14.967 mL of MQ-H_2O and sonicated for 5 minutes. 20 mL AuNP@cit as prepared in 2.2.2.1 were centrifuged (9000 RCF, 30 minutes, 8 °C), the supernatant was removed, AuNP@cit were resuspended in fresh MQ-H_2O and transferred to a 50 mL round bottom flask. Under stirring the PAH solution was added dropwise to the AuNP@cit solution at room temperature and left for 24 hours. Other incubation conditions were used, including changing the reaction time to 1 and 2 hours, and changing the concentration of PAH used (1 mg mL^{-1}, 2 mg mL^{-1}). The solution was then cleaned using 3 cycles of centrifugation (9000 RCF, 30 minutes, 8 °C) and resuspension and finally resuspended in 20 mL of MQ-H_2O to give poly(allylamine)-coated Gold Nanoparticles (AuNP@PAH)

2.2.2.3 Poly(styrene sulfonate)@poly(allylamine)-coated Gold Nanoparticles (AuNP@PAH@PSS)

45.96 mg of poly(sodium styrene sulfonate) (mw. 15k) (PSS) was dissolved in 14.967 mL of MQ-H_2O and sonicated for 5 minutes. 20 mL of AuNP@PAH as prepared in 2.2.2.2 was transferred to a 50 mL round bottom flask. Under stirring the PSS solution was added dropwise to the AuNP@PAH solution at room temperature and left to stir for 24 hours. The solution was then cleaned using 3 cycles of centrifugation (9000 RCF, 30 minutes, 8 °C), resuspension and finally resuspended in 20mL of MQ-H_2O to give poly(styrene-sulfonate)@poly(allylamine)-coated Gold Nanoparticles (AuNP@PAH@PSS).

2.2.3 Preparation of Rose Bengal Loaded Gold Nanoparticles

Due to the light sensitive nature of Rose Bengal, these experiments were carried out in the dark and any products were protected from light.

2.2.3.1 Poly(allylamine) Loaded with Rose Bengal (PAH-RB)

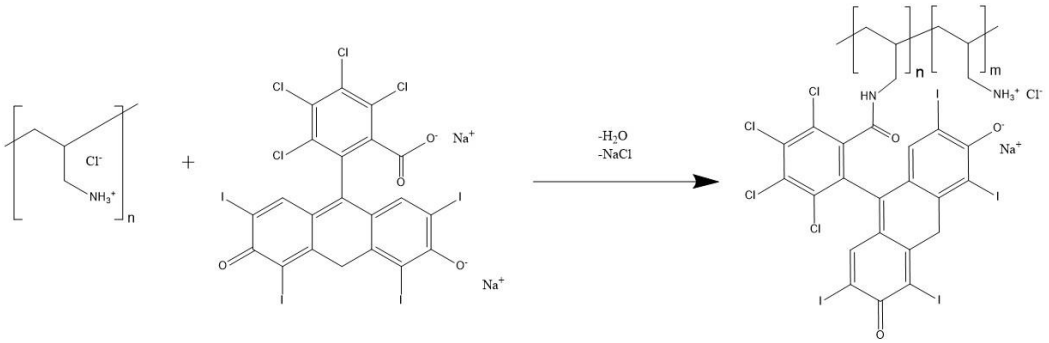

PAH (1) Rose Bengal (2) PAH-RB (3)

Scheme 1 – Reaction scheme for EDC based coupling of PAH (1) and Rose Bengal (3) to form PAH-RB (3).

0.22 g of 2-(4-morpholino)-ethane sulfonic acid monohydrate (MES) was added to 100 mL MQ-H_2O resulting in a MES concentration of 10 mM and adjusted to pH 5.1 using NaOH. A stock solution of Rose Bengal (7.51×10^{-3} M) was prepared as follows; 31 mg of Rose Bengal was dissolved in 10 mL MES (10 mM, pH 5.1) and stored in the dark.

A 10 mL solution of MES buffered Rose Bengal (3 x 10^{-4} M) was added to a 50 mL round-bottom flask. To this 2.97 x 10^{-5} moles of EDC (1 mL, MQ-H_2O) were added and left to stir for 30 minutes. 0.15 g of PAH (mw. 15000) were dissolved in 20 mL of MES (10 mM, pH 5.1), the solution was sonicated for 5 minutes, added to the EDC and RB solution and left for 24 hours. The solution was then transferred to 10,000 mw cut-off dialysis tubing and dialysed against 1 L of MQ-H_2O for 4 days. The water was changed after 2 hours and then every subsequent 24 hours.

2.2.3.2 Poly(allylamine)-Rose Bengal-poly(styrene sulfonate)-coated Gold Nanoparticles (AuNP(@PAH-RB@PSS)n)

20 mL AuNP@cit as prepared in 2.2.2.1 were centrifuged (9000 RCF, 30 minutes), the supernatant removed, resuspended in MQ-H_2O and transferred to a 50 mL round-bottom flask. Under stirring, 15.32 mL PAH-RB solution (PAH: 3 mg mL^{-1} (based on the original weight used in section 2.2.3.1), NaCl: 23 mM) were added dropwise to the AuNP@cit solution at room temperature and left to stir for 24 hours. This mixture was then cleaned using 3 cycles of centrifugation (9000 RCF, 30 minutes, 8 °C) and resuspension and finally resuspended in 0.8 mL of MQ-H_2O to give AuNP@PAH-RB. NaCl free synthesis was also performed, which was identical except for addition of NaCl. Additionally, the PAH-RB conditions were varied.

45.96 g of PSS (mw. 15k) was dissolved in 14.97 mL of MQ-H_2O, 0.353 mL 1 M NaCl and sonicated for 5 minutes. 20 mL of AuNP@PAH-RB were transferred to a 50 mL round bottom flask. Under stirring the PSS solution was added dropwise to the AuNP@PAH solution at room temperature and left to stir for 24 hours. The solution was then cleaned using 3 cycles of centrifugation (9000 RCF, 30 minutes, 8 °C) and resuspension and finally resuspended in 20 mL of MQ-H_2O to give poly(styrene-sulfonate)@poly(allylamine)-coated Gold Nanoparticles (AuNP@PAH-RB@PSS). An NaCl free synthesis was also performed, which was identical except for addition of NaCl. The method described in this section could then be repeated to yield additional layers of PAH-RB@PSS.

2.2.4 Characterisation Methods

2.2.4.1 UV-vis spectroscopy

Spectra were recorded on a spectrophotometer (Thermofisher Scientific Genesys 10S, Agilent Cary 8454) using a quartz cuvette with a path length of 1 cm.

2.2.4.2 Differential centrifugation sedimentation (DCS) – experimental setup

AuNP size distributions were measured by DCS using a DCS disc centrifuge (CPS instruments Inc. DC24000). The rotating disc was loaded with fresh 8 wt. % sucrose in MQ-H_2O, increasing to 24 wt. % over 9 successive additions while spinning at 24,000 rpm. The gradient was then left for at least 1 hour to equilibrate. The machine was calibrated before each measurement with 0.1 mL of 0.226 µm poly(vinyl chloride) particles (Analytik Ltd.), before 0.1 mL of sample was injected into the disc. Each sample was analysed at least three times to verify reproducibility.

2.2.4.3 Differential centrifugation sedimentation (DCS) – analysis of particle size

A nanoparticle that consists of a core of diameter d_{core} with a density of ρ_{core} and a capping layer with thickness s and density ρ_{shell} has a total diameter of $d_{core} + 2s$. The average density of this nanoparticle is shown in equation 2.1.

$$\rho_{effective} = \frac{{d_{core}}^3 \rho_{core} + ((d_{core} + 2s)^3 - {d_{core}}^3)\rho_{shell}}{(d_{core} + 2s)^3}$$

Equation 2.1

The measured sedimentation time of the nanoparticle described in equation 2.1, t, can be calculated from equation 2.2 according to Stokes' law. In this equation, ρ_{fluid} is the average density of the sucrose solution in which the AuNP is sedimented. C is a constant that depends on viscosity, spin speed and cell geometry, however this is determined for each experiment using a calibration with 226 nm PVC nanoparticles.

$$t = \frac{C}{(\rho_{effective} - \rho_{fluid})(d_{core} + 2s)^2}$$

Equation 2.2

However, the DCS instrument reports d_{DCS} which represents the diameter of a nanoparticle with a homogeneous density that sediments and reaches the detector at time t. In this case, it is assumed that the density of this nanoparticle is 19.3 g cm^{-3} (the density of the gold core, ρ_{core}), leading to the simplification of the denominator of equation 2.2 seen in equation 2.3, this leads to equation 2.4.

$$t = \frac{C}{(\rho_{core} - \rho_{fluid})\ {d_{DCS}}^2}$$

Equation 2.3

$$(\rho_{effective} - \rho_{fluid})(d_{core} + 2s)^2 = (\rho_{core} - \rho_{fluid})\ {d_{DCS}}^2$$

Equation 2.4

The position of the maxima in these distributions were averaged, in order to provide an average d_{DCS} calculated by the machine according to equation 2.4 assuming a ρ_{core} density of 19.3 g cm^{-3}. This means that dDCS is actually not the correct diameter of the NP, since it ignores the contributions made by the less dense shell to equation 2.2. A combination of equations 2.1 and 2.4 allows us to relate apparent diameter d_{DCS} to shell thickness (s), core size (d_{core})as shown in equation 2.5.

$$d_{DCS} = (d_{core} + 2s)\sqrt{\frac{(({d_{core}}^3\rho_{core}) + ((d_{core} + 2s)^3 - {d_{core}}^3)\rho_{shell}) \div ((d_{core} + 2s)^3) - \rho_{fluid}}{\rho_{core} - \rho_{fluid}}}$$

Equation 2.5

For a AuNP analysis, it is known from literature that the citrate capping layer has a thickness of 1 nm which allows determination of d_{core}.[1] This then allows the elucidation of capping layer thickness s, when ρ_{shell} is assumed to be 1.4 g cm^{-3}, from equation 2.5. While this is an approximation for a dense organic capping layer, the effect of changing ρ_{shell} between 1.1 g cm^{-3} (porous protein capping layer) and 1.5 g cm^{-3} on determined capping layer thickness is insignificant. The shell thickness obtained for the conditions reported here does not change significantly when varying the density over this range.

2.2.4.4 Zeta-potential

Zeta-potential was measured on a Zetasizer Nano (Malvern Panalytical) using folded capillary zeta cells (DTS1070, Malvern Panalytical). Before sample measurement, the cell was flushed extensively with ethanol and MQ-H_2O (passed through a 0.22 µm filter).

2.3 Characterisation of AuNPs

2.3.1 Characterisation of AuNP@cit

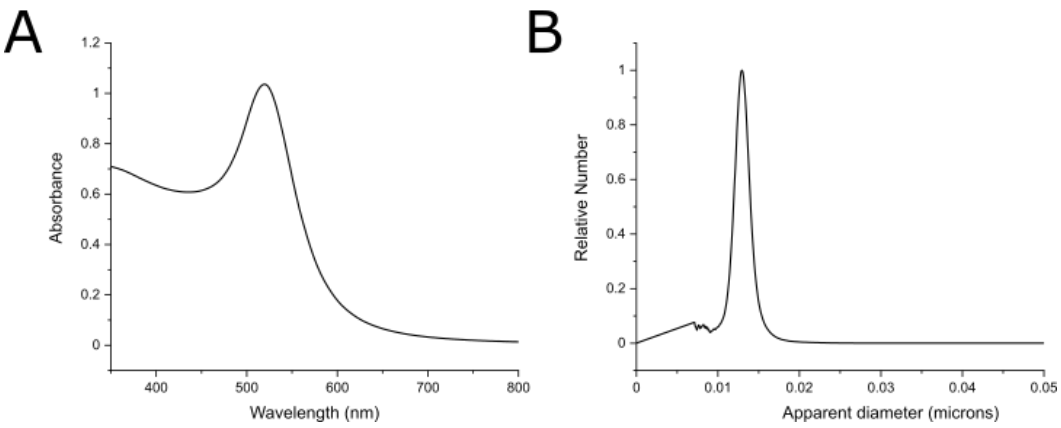

Figure 2.2 – Characterisation of AuNP@cit; A) UV-vis spectrum, B) a size distribution obtained using DCS.In B). These correspond to maxima at; A) 520 nm, B) 12.9 nm.

AuNP@cit were successfully synthesised according to the Turkevic-Frens reaction, a characterisation of AuNP@cit can be seen in figure 2.2. The size of AuNP@cit in figure 1.1. was determined using DCS, via the analysis described in 1.2.4.2 to give Au d_{core} size of 13.8 nm. The UV-vis spectrum is consistent with this sizing with a LSPR peak at 520 nm.[2] Figure 2.2B shows the high monodispersity of AuNPs synthesised using this method. The concentration of AuNPs can be determined using the absorbance at 450 nm and calculated molar extinction coefficients for gold core sizes reported by Haiss.[2] For this batch of AuNP@cit, the concentration of the AuNPs as prepared was determined to be 3.68 nM. While the size of the AuNP@cit used in each cell experiment will be stated, and there is some variation in size between different syntheses of AuNP@cit, typically the d_{core} size falls between 13-14 nm.

2.3.2 AuNP@PAH and AuNP@PAH@PSS

2.3.2.1 Characterisation of AuNP@PAH and AuNP@PAH@PSS

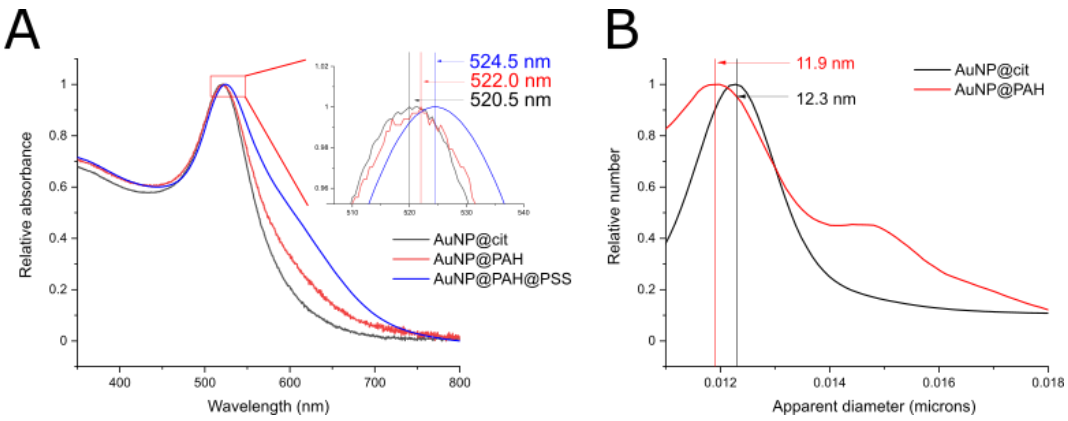

Figure 2.3 – Characterisation of AuNP@cit, AuNP@PAH and AuNP@PAH@PSS. A) Normalised UV-vis spectra, B) size distribution obtained using DCS. These correspond to maxima at; A) 520.5, 522.0 and 524.5 nm; B) 12.3 and 11.9 nm, respectively.

AuNP@PAH and AuNP@PAH@PSS were synthesised as described in section 2.2.2.3 and 2.2.2.4, and characterised using DCS and UV-vis spectroscopy. Characterisation of these AuNPs is shown in figure 2.2, these were synthesised using polyelectrolyte concentrations of 3 mg mL^{-1} and incubation times of 24 hours. The use of PAH and PSS in a layer-by-layer coating regimen for AuNPs is well established, with literature describing ideal coating conditions and characterisation of AuNP(@PAH@PSS)$_n$.[6] The change in the plasmon peak determined by UV-vis is consistent with that described in literature, with a 2 nm shift per layer of polyelectrolyte added. For AuNP@PAH, DCS characterisation showed a shift in the apparent diameter from AuNP@cit (12.3 nm) to AuNP@PAH (11.9 nm). This is indicative of the formation of a thicker shell compared to AuNP@cit. This corresponds to a layer thickness of 1.5 nm (result can be seen in table 2-1), which is similar to the accepted thickness of 1 nm per polyelectrolyte shell, which were reported using incubations with 2.7 mg mL^{-1} of PAH for 18 hours.[7]

The presence of dimers can be confirmed by the size distribution, with the peak at 15 nm corresponding to a AuNP@PAH dimer. This can also be seen in the UV-vis with the broadening of the spectra between 600-800, which increases after the addition of the PSS layer.

2.3.2.2 Effect of Changing Polyelectrolyte Incubation Conditions

The effect of incubation conditions on the polyelectrolyte shell was investigated. Through increasing the initial concentration of PAH from 1 mg mL^{-1} to 3 mg mL^{-1} we can increase the thickness of the polyelectrolyte capping layer from 0.84 to 1.23 nm for a 1 hour incubation. Increasing the incubation time also increases the thickness of the polyelectrolyte capping layer. This increased capping layer also prevents some of the aggregation that can be seen via UV-vis between 600-800 nm. Despite the higher concentration of PAH and longer incubation time, AuNP@PAH (incubation conditions:3 mg mL^{-1}, 24 hours) has a smaller dimer peak in the DCS (15 nm) when compared to AuNP@PAH (incubation conditions: 1 mg mL^{-1}, 1 hour).

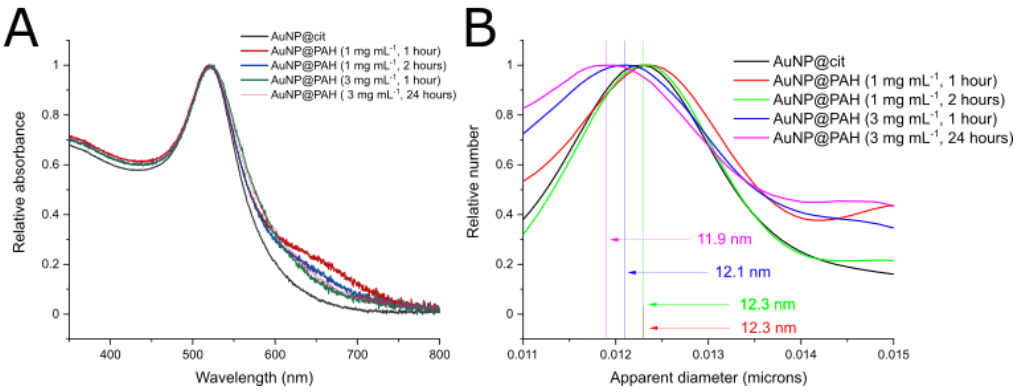

Figure 2.4 – Characterisation of AuNP@PAH where the incubation concentration and time were changed; A) Normalised UV-vis spectra, B) size distribution obtained using DCS.

Concentration (mg mL^{-1})	Time (hours)	d(DCS) (nm)	Shell thickness (nm)
1	1	12.35	0.84
1	2	12.3	0.96
3	1	12.1	1.23
3	24	11.9	1.52

Table 2-1 – Shell thicknesses determined by DCS for different incubation conditions during the synthesis of AuNP@PAH

These AuNPs are stable, and a capping layer is present in all cases, for AuNP@PAH prepared with a PAH concentration of 1 mg mL^{-1}, the apparent diameter reported by

DCS does not significantly shift between AuNP@cit and AuNP@PAH. The presence of a PAH capping layer can be confirmed on these AuNPs as they do not aggregate during the cleaning process. Typically, AuNP@cit will aggregate after several cycles of washing as the citrate is only electrostatically bound to the surface. As such, when the citrate concentration in the solvent is reduced, citrate desorbs from the surface of the AuNP, leading to loss of stability and aggregation. The data presented suggest that the citrate layer is almost entirely replaced by a PAH layer, and when this layer is at its thinnest it provides a similar density and thickness as a AuNP@cit layer.

As the Au surface is positively charged, if bonding was dependent only on electrostatic interactions it would be unlikely that PAH would bind to the Au surface, however due to the excess of amine groups it is likely that these form a covalent bond to the gold surface which overcomes the electrostatic coating to provide a basis for the layer-by-layer coating. The ability of amines to covalently bind to gold nanoparticles is well established, this includes the use of polyethylenimine as a replacement for citrate during the synthesis of AuNPs.[8,9]

There is a characteristic shift in the plasmon band as described in 2.3.2.1, however changing the thickness of the PAH capping layer does not significantly change the position of the plasmon peak.

For all further work we used incubation conditions of 3 mg mL^{-1}, 24 hours as it gave the thickest capping layer.

2.3.3 Characterisation of PAH-RB

The loading of Rose Bengal into PAH was considered successful, as despite extensive dialysis very little free Rose Bengal was lost during the cleaning process. The UV-vis spectra were consistent with literature, with an increase in scattering, increased width of the absorbance band, and increased absorption at 520 nm compared to the main peak at 555 nm.[4] We ascribe this to a different and more inhomogeneous environment inside the polymer than in solution, leading to a different ratio of conformer populations. However, throughout the project it became clear that upon use of PAH-RB in AuNPs a large amount of free Rose Bengal leached out of PAH-RB (see section 2.4.1), this means a large fraction of the Rose Bengal was not covalently

bound using EDC chemistry as desired. Due to the negative charge of Rose Bengal and the positive charge of PAH electrostatic binding is possible. Work in our group by H. McNicholl estimated the efficiency of covalent binding as 40% using UV-vis spectroscopy.[10] The efficacy of the loading will be further discussed in 2.3.5 and 2.4.1.

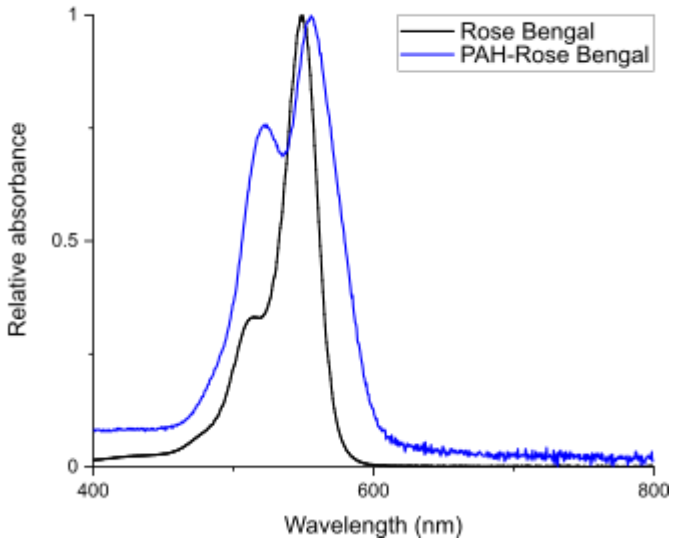

Figure 2.5 – Normalised UV-vis spectra of RB (black) and PAH-RB (blue). The absorbances have been normalised against the absorbance peak in each spectrum. For RB the peaks are at 515 and 548.5 nm, with relative absorbance of 0.33 and 1, respectively. For PAH-RB the peaks are at 522.5 and 555 nm with relative absorbances of 0.75 and 1 respectively.

2.3.4 Characterisation of AuNP@PAH-RB and AuNP@PAH-RB@PSS

2.3.4.1 Characterisation of AuNP@PAH-RB

The characterisation of AuNP@PAH-RB can be seen in figure 2.6 and in table 2-2. The thickness of the shell, when synthesised in the absence of NaCl, is similar to that reported in 2.3.2 for NP@PAH, suggesting that the presence of Rose Bengal does not significantly change the properties of the PAH layer. This is expected, since only a small fraction PAH amine groups are expected to interact with a Rose Bengal, as discussed in section 2.4.1.

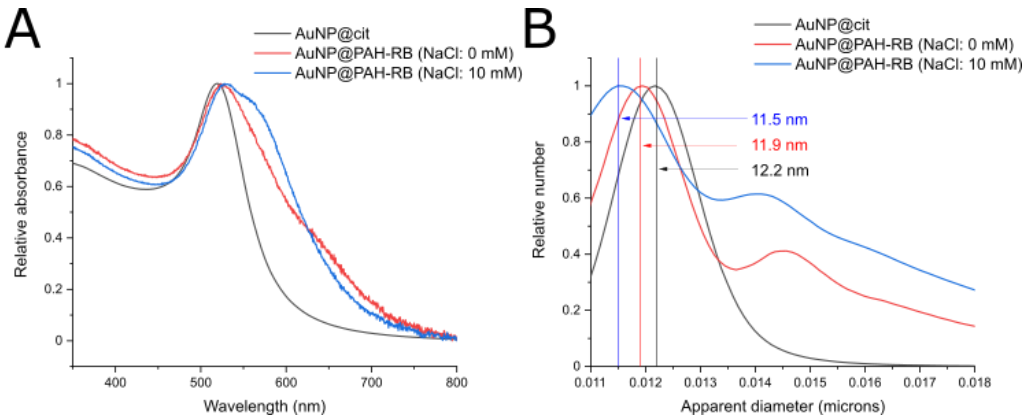

Figure 2.6 Characterisation of AuNP@PAH-RB when different NaCl conditions were used during incubation. A) UV-vis spectra, B) size distribution obtained using DCS.

Concentration (mg mL^{-1})	Time (hours)	NaCl (mM)	d(DCS) (nm)	Shell thickness (nm)
3	24	0	11.93	1.40
3	24	10	11.55	1.84

Table 2-2 – Calculated shell thicknesses calculated from DCS for AuNP@PAH_RB synthesised with or without 10 mM NaCl.

The use of salt to increase the thickness of polyelectrolyte layers is well established.[6] and can be seen in table 2-2 when 10 mM NaCl was used. No similar attempt (synthesis in presence of NaCl) had been made for AuNP@PAH. Upon analysis of the shell thickness, this confirms that the layer thickness reported is 50% thicker than when no salt is present. The spectra seem to show a shift in the position of the LSPR, but it is impossible to directly compare these spectra due to due to the presence of non-NP bound Rose Bengal (~575 nm) which distorts the spectra. The presence of this Rose Bengal is likely due to the self-agglomeration of PAH-RB into large (200 nm) aggregates, which will be discussed further in 2.3.5. For all cell experiments using AuNP@PAH-RB@PSS, the 10 mM NaCl protocol was used due to the slightly thicker PAH-RB layer.

Despite the addition of NaCl to increase the capping layer thickness, AuNP@PAH-RB were unstable, aggregating after around 2 weeks. This may be due to the presence of free Rose Bengal, which due to its negative charge may compromise stabilisation.

2.3.4.2 Characterisation of AuNP@PAH-RB@PSS

When a PSS layer is added to AuNP@PAH-RB, the increase in shell thickness is significantly less pronounced than the initial addition of a PAH-RB layer. The 0.15 nm increase in capping layer thickness is consistent between syntheses with or without NaCl. While literature does report that subsequent layers are not as thick as the initial PAH layer, the addition of a PSS layer assessed using TEM leads to an increase of 0.5 nm to the shell thickness.[7] When a second bilayer was added to form AuNP@PAH-RB@PSS@PAH-RB@PSS, our data supports the reduction in increasing capping layer thickness which only adds 1.5 nm compared to AuNP@PAH-RB@PSS, where the initial bilayer resulted in a shell thickness of 1.97 nm. However, as the literature data was collected using TEM, it is likely that our analysis using DCS provides a more accurate determination of the thickness of the capping layer. It likely that the addition of a PSS layer compresses the PAH-RB layer so the overall added shell thickness is less. Another explanation is that a significant amount of the PSS layer intercalates with the PAH layer, displacing water and chloride ions from the PAH layer.

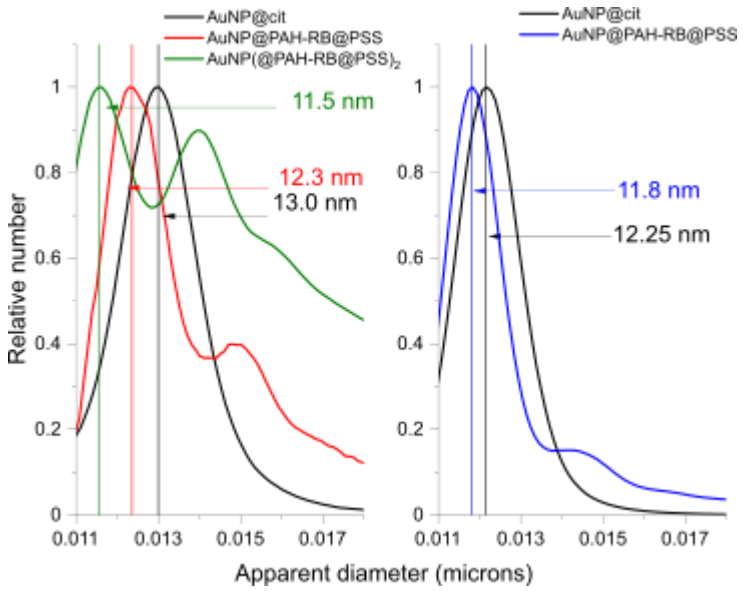

Figure 2.7 – DCS characterisation of; A) AuNP@PAH-RB@PSS and AuNP@PAH-RB@PSS@PAH-RB@PSS when 10 mM NaCl was used, B) AuNP@PAH-RB@PSS when 0 mM NaCl was used.during polymer incubation. Different batches of AuNP@cit were used in A) and B), which can be seen by the variation of the distribution of AuNP@cit.

Number of bilayers	Concentration (mg mL^{-1})	Time (hours)	NaCl (mM)	d(DCS) (nm)	Shell thickness (nm)
1	3	24	0	11.80	1.37
1	3	24	10	12.30	1.97
2	3	24	10	11.50	3.48

Table 2-3 – Shell thicknesses calculated from DCS for AuNP@PAH-RB@PSS synthesised with or without 10 mM NaCl and AuNP@PAH-RB@PSS@PAH-RB@PSS synthesised with 10 mM NaCl.

The addition of PSS, and the subsequent 3 washes, significantly reduces the amount of Rose Bengal distorting the UV-vis spectra discussed in 2.3.4.1, however it is likely that a significant amount of Rose Bengal is still present in the form of PAH-RB@PSS polyelectrolyte complexes, see section 2.3.6. There is a significant widening of the LSPR band visible when NaCl is used, as seen in figure 2.8, suggesting increased aggregation; however, this is unlikely to significantly affect the use of AuNP@PAH-RB@PSS on cells as the AuNPs typically enter cells following aggregation on the cell membrane. There is significantly more Rose Bengal present in AuNP@PAH-RB@PSS@PAH-RB@PSS, as the addition of PAH-RB to AuNP@PAH-RB@PSS takes place when there are still large PAH-RB@PSS aggregates leading to more agglomeration and incorporation of new PAH-RB into these agglomerates.

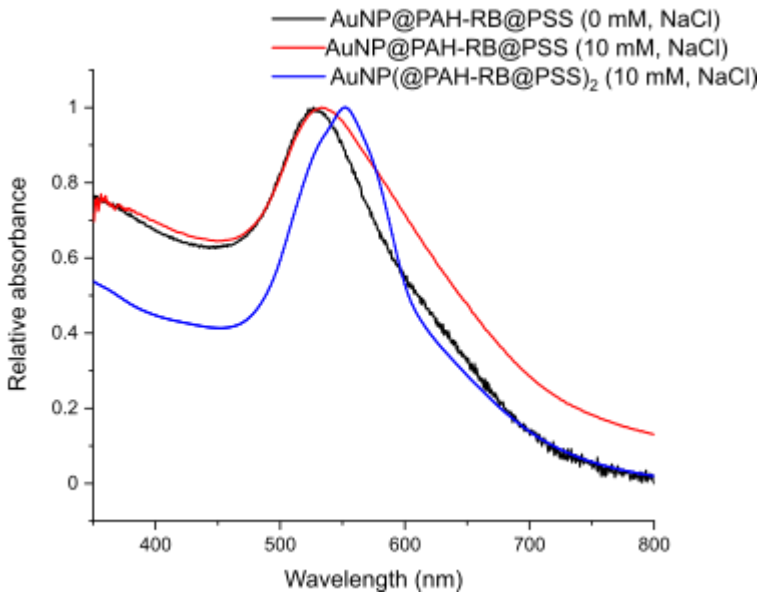

Figure 2.8 – UV-vis spectra of AuNP@PAH-RB@PSS synthesised with 0 mM NaCl (black), 10 mM NaCl (red) and AuNP@PAH-RB@PSS@PAH-RB@PSS with 10 mM salt (blue).

While AuNP@PAH-RB@PSS@PAH-RB@PSS were not used in cell experiments, the addition of further layers of PAH-RB would reduce the need for the thickest PAH-RB shell which would allow the elimination of NaCl in the synthesis. Therefore, if further layer-by-layer coatings were to be used, the elimination of NaCl from the synthesis would be preferential, but for the current work has been used throughout.

2.3.4.3 Change in ζ-potential in sequential synthesis of AuNP@PAH-RB@PSS@PAH-RB@PSS (10 mM NaCl)

ζ-potential was monitored for a synthesis all intermediates during a synthesis of AuNP@PAH-RB@PSS@PAH-RB@PSS, as can be seen in table 2-4, the characteristic switching of the surface charge at each synthesis step can clearly be seen. The values reported are consistent with literature, and the values for AuNP@..@PSS are consistent through the synthesis.[4] However, the lack of stability of AuNPs with a PAH-RB outer layer is evident from the values obtained. This is in line with experimental observations that nanoparticles with PAH-RB outer layers show the lowest stability of all AuNP synthesised.

AuNP	AuNP@cit	AuNP@PAH-RB	AuNP@PAH-RB@PSS	AuNP@PAH-RB@PSS@PAH-RB	AuNP@PAH-RB@PSS@PAH-RB@PSS
ζ-potential / mV	-42.6±0.9	+27.4±1.0	-37.3±1.4	15.6±3.2	-35.6±2.4

Table 2-4 ζ-potential determined at each step in a synthesis of AuNP@PAH-RB@PSS@PAH-RB@PSS

Despite the variation in surface charge for AuNPs with PAH-RB as the outer layer, the overall switching confirms the successful nature of the layer-by-layer synthesis.

2.3.5 Leaching of Rose Bengal

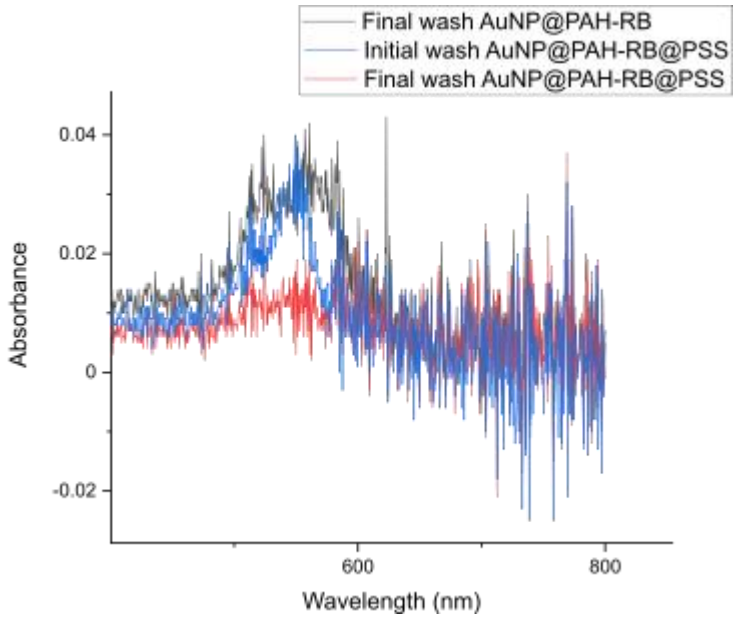

Figure 2.9 – UV-vis spectra of the supernatant from washes of AuNP@PAH-RB and AuNP@PAH-RB@PSS.

During the washing process, the supernatant was monitored using UV-vis spectroscopy to see the amount of PAH-RB remaining in each wash. While after 3 washes, there was very little PAH-RB remaining following the cleaning process associated with the synthesis of AuNP@PAH-RB, following the synthesis of AuNP@PAH-RB@PSS there was a refreshed presence of Rose Bengal in the supernatant, as due to the dilution between the final wash of AuNP@PAH-RB and AuNP@PAH-RB@PSS we would expect significantly less Rose Bengal absorbance. Importantly, this was distinct from PAH-RB spectra and was characteristic of free Rose Bengal rather than PAH-RB. This suggests that upon PSS addition to the

AuNP@PAH-RB solution, electrostatically bound Rose Bengal was displaced from PAH-RB by PSS.

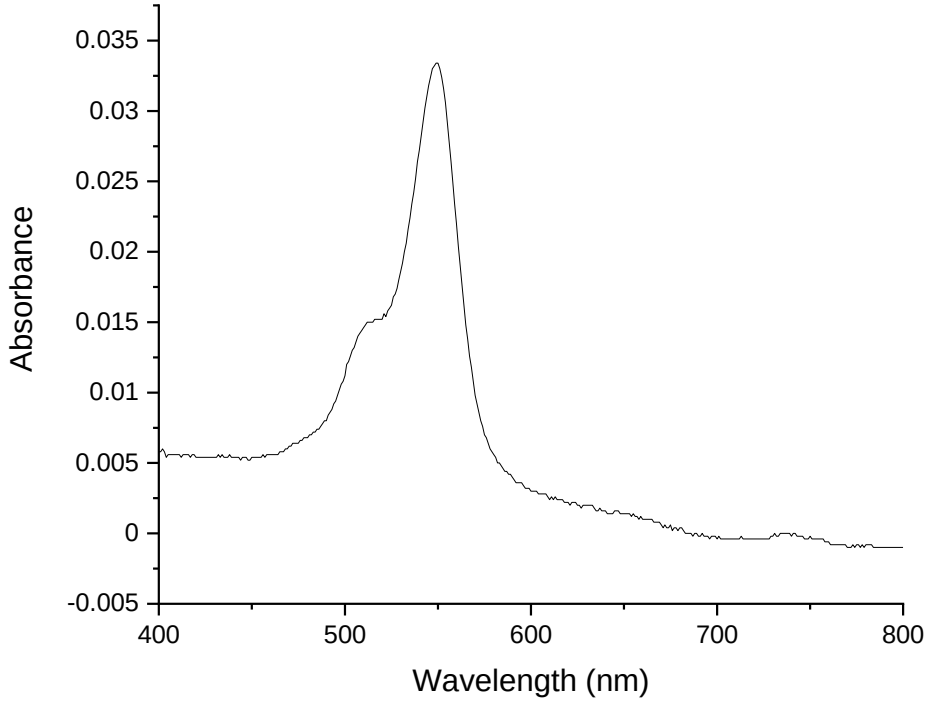

Figure 2.10 – UV-vis spectrum of the supernatant of AuNP@PAH-RB@PSS upon centrifugation 2 months after the synthesis and initial cleaning.

In addition to loss of Rose Bengal during the washing process, a solution of AuNP@PAH-RB@PSS that was used for cell treatments over a 2 month period showed a significant absorbance of Rose Bengal in the supernatant following centrifugation with a magnitude of 0.035 which can be seen in figure 2.10. This spectrum resembles the spectrum of free Rose Bengal, rather than PAH-RB, see figure 2.5. This is over an order of magnitude greater than the absorbance for the amount of Rose Bengal we would expect to be contained in the PAH-RB layer surrounding the AuNP, see section 2.4.2. This suggests that it is coming primarily from the polyelectrolyte complexes in the solution, confirming that a significant amount of Rose Bengal was not covalently bound to the polymer as mentioned in 2.3.3.

2.3.6 Presence of PAH-RB@PSS Aggregates

Recent results obtained in our group show that the addition of 1 M NaCl to PAH-RB leads to aggregation and formation of larger PAH-RB complexes.[10] It is likely that a small amount of these complexes are created during the synthesis of AuNP@PAH-RB described here (NaCl:10 mM); due to their size cleaning via centrifugation also sediments these complexes, preventing their removal. Upon addition of PSS, Rose Bengal is gradually replaced by the polyelectrolyte in these complexes and AuNP@PAH-RB@PSS leading to free Rose Bengal in the solution. The leaching reported in section 2.3.5, is dominated by the leaching from PAH@PSS, however it cannot be ruled out that this also happen for AuNP@PAH-RB@PSS. Negatively charged azo-dyes contained in polyelectrolyte layers showed good stability over the course of several months, suggesting that the strong electrostatic envelopment should be sufficient to contain the Rose Bengal in the bilayer, however this is speculation.[11–13]

The presence of these aggregates prevented quantitative analysis of singlet oxygen generation using molecular probes as the Rose Bengal present in these agglomerates is significantly higher than contained in the PAH-RB layers surrounding the AuNP.

They are unlikely to play a role in cell experiments, as in order for these to be removed by centrifugation at the same rate as the gold nanoparticles which have much higher density, the minimum size of these complexes would be 100 nm. Due to the excess of PSS present it is likely that these polymer complexes are negatively charged, and are at a concentration of less than 8.5×10^{-12} M. While the uptake of polyelectrolyte complexes has been studied in literature, the only uptake studies exist for positively charged complexes exclusively and there is no evidence that negatively charged polyelectrolyte complexes are taken up by cells.[14–16] Negatively charged poly(L-glutatmate-co-N-3-L-glutamylsulfanilic acid)@insulin complexes were found not to interact with epithelial cells even when supplemented with media.[17] In addition to literature suggesting that such complexes are not taken up significantly by cells, our own comparisons between toxicity between AuNP@cit and AuNP@PAH-RB@PSS in HeLa cells suggests that the toxicity occurs at similar levels

of generated singlet oxygen. If these polyelectrolyte complexes had a significant impact, the efficacy of the irradiation would be significantly larger.

While cells have been shown to take up positively charged polyelectrolyte complexes, there is no evidence that negatively charged polyelectrolyte complexes are significantly taken up into cells and therefore these complexes should have no effect on cell experiments. Indeed, despite the leaching of Rose Bengal discussed in section 2.3.5, no decline in photodynamic activity was observed throughout the 2 month period over which AuNP@PAH-RB@PSS were used on cells, suggesting that any leaching from these polyelectrolyte complexes or AuNP@PAH-RB@PSS has no effect upon killing and therefore they are insignificant in any cell killing. This also suggests that the AuNP@PAH-RB@PSS retains electrostatically Rose Bengal, or more likely, loses it during the synthesis due to intercalation of PSS in the PAH-RB layer.

2.4 Determination of Rose Bengal loading in PAH-RB and AuNP@PAH-RB@PSS

2.4.1 Rose Bengal Loading

The loading of Rose Bengal into PAH using EDC chemistry was initially reported by Serrano, though sulfo-NHS was used to increase reaction efficiency.[4] The shift in the Rose Bengal absorbance band, and increased absorption of the shoulder was reported as a sign that the bonding was successful. However, our results show that dialysis does not successfully remove non-covalently bound Rose Bengal from the reaction mixture due to electrostatic retention. Due to this, nearly all of the Rose Bengal was retained in the reaction mixture, as verified by UV-vis spectroscopy on dialysis solvents, and other than through gradual leaching it is impossible to distinguish between covalently and electrostatically bound Rose Bengal. It has been reported that upon mixing a polyelectrolyte and charged dye, large polyelectrolyte-dye nanoparticles can be formed, however it seems that this does not occur in PAH-RB mixtures with salt absent.[18]

However, for future applications of PAH-RB it is important to quantify the amount of Rose Bengal loaded into the polyelectrolyte. Since virtually all Rose Bengal is loaded into PAH, we can calculate the Rose Bengal loading by using the stoichiometric ratio

between PAH and RB in the reaction solution. This results in a ratio of Rose Bengal to amines 1.81:1000 amines. While this number is low, it is important that the modified polyelectrolyte retains its charge for the subsequent layer-by-layer coating of AuNPs.

2.4.2 Rose Bengal Loading in AuNP@PAH-RB@PSS

As we know the thickness of the PAH-RB layer on an AuNP@PAH-RB and we know the ratio of Rose Bengal to PAH monomers, we can calculate the number of Rose Bengal molecules contained in each AuNP. The shell density was assumed to be 1.4 g cm^{-3}, this is expected to be an overestimate, since the PAH monolayer will contain a significant amount of water and counterions which contribute to the shell volume but are ignored in the analysis.

Upon adding PSS, it is likely that a significant fraction of those solvent molecules and counterions are expelled, leading to a collapse of the first layer, this means that it is realistic to assume that it has only half of the thickness of the total layer, which yields a more realistic estimate of the PAH (and hence Rose Bengal) content. The results of this are tabulated in table 2-5, with 2 different shell thicknesses, these correspond to; an equal split of the polyelectrolyte shell between PAH-RB and PSS, and the layer thickness determined in AuNP@PAH-RB

AuNP	Layer thicknesss (nm)	Shell volume (m^3)	Number of Rose Bengal ($AuNP^{-1}$)
AuNP@PAH-RB	1.84	1.262×10^{-24}	33.78
AuNP@PAH-RB@PSS	0.985	6.77×10^{-25}	18.12

Table 2-5 - Shell thickness and amount of Rose Bengal loaded in each AuNP@PAH-RB or AuNP@PAH-RB@PSS.

However, as mentioned in section 2.3.3, the efficiency of covalent binding was determined in the group to be 40%. In light of the leaching observed 2.3.5, we assume that this is displaced by PSS. This leads to a value, obtained of 7.2 Rose Bengal molecules per AuNP@PAH-RB@PSS for the equal split of the polyelectrolyte shell between PAH-RB and PSS. This value will be used for estimates of $^1O_2$ generation in cells reported in chapter 4.

2.5 Conclusion

Polyelectrolyte coated AuNPs (AuNP@PAH, AuNP@PAH-RB, AuNP@PAH@PSS, AuNP@PAH-RB@PSS, AuNP@PAH-RB@PSS@PAH-RB@PSS) and AuNP@cit were successfully synthesised. These were characterised using UV-vis and DCS to provide accurate sizing of both the Au core and the thickness of the polyelectrolyte shell.

Rose Bengal was loaded into PAH to give PAH-RB, however 60% of loading was mediated by electrostatic attraction rather than as a covalent bond. The use of NaCl in the synthesis of AuNP@PAH-RB@PSS also led to PAH-RB@PSS polyelectrolyte complexes that centrifugal cleaning of AuNPs could not remove. However, these are unlikely to play a role in cell experiments.

The use of PAH-RB did not significantly alter the properties required for a successful layer-by-layer coating of AuNPs, and the loading of Rose Bengal in AuNP@PAH-RB@PSS was determined to be 7.2 Rose Bengal molecules per AuNP.

2.6 References

(1) Brust, M.; Cooper, D. L.; Krpeti, L. Z.; Davidson, A. M.; Volk, M.; Kingdom, U.; Science, S.; Square, A.; Biology, C.; Biology, I.; Interactions, B. High-Resolution Sizing of Monolayer- Protected Gold Clusters by Di Ff Erential Centrifugal Sedimentation. *ACS Nano* **2013**, No. 10, 8881–8890.

(2) Haiss, W.; Thanh, N. T. K.; Aveyard, J.; Fernig, D. G. Determination of Size and Concentration of Gold Nanoparticles from UV-Vis Spectra. *Anal. Chem.* **2007**, *79* (11), 4215–4221. https://doi.org/10.1021/ac0702084.

(3) Bhattacharjee, S. DLS and Zeta Potential - What They Are and What They Are Not? *J. Control. Release* **2016**, *235*, 337–351. https://doi.org/10.1016/j.jconrel.2016.06.017.

(4) Serrano, M. P.; Rafti, M.; Thomas, A. H.; Borsarelli, C. D. Photosensitizing Properties of Hollow Microcapsules Built by Multilayer Self-Assembly of Poly(Allylamine Hydrochloride) Modified with Rose Bengal. *RSC Adv.* **2019**, *9* (33), 19226–19235. https://doi.org/10.1039/c9ra03153g.

(5) Frens, G. Controlled Nucleation for the Regulation of the Particle Size in Monodisperse Gold Suspension. *Nat. Phys. Sci.* **1973**, *241*, 20–22. https://doi.org/10.1038/physci241020a0.

(6) Schneider, G.; Decher, G. Functional Core/Shell Nanoparticles via Layer-by-Layer Assembly. Investigation of the Experimental Parameters for Controlling Particle Aggregation and for Enhancing Dispersion Stability. *Langmuir* **2008**, *24* (5), 1778–1789. https://doi.org/10.1021/la7021837.

(7) Schneider, G.; Decher, G. From Functional Core/Shell Nanoparticles Prepared via Layer-by-Layer Deposition to Empty Nanospheres. *Nano Lett.* **2004**, *4* (10), 1833–1839. https://doi.org/10.1021/nl0490826.

(8) Veerakumar, P.; Velayudham, M.; Lu, K. L.; Rajagopal, S. Polyelectrolyte Encapsulated Gold Nanoparticles as Efficient Active Catalyst for Reduction of Nitro Compounds by Kinetic Method. *Appl. Catal. A Gen.* **2012**, *439–440*, 197–205. https://doi.org/10.1016/j.apcata.2012.07.008.

(9) Zakaria, H. M.; Shah, A.; Konieczny, M.; Hoffmann, J. A.; Nijdam, A. J.; Reeves, M. E. Small Molecule- and Amino Acid-Induced Aggregation of Gold Nanoparticles. *Langmuir* **2013**, *29* (25), 7661–7673. https://doi.org/10.1021/la400582v.

(10) Harriet McNicholl. Optimising the Functionalisation Process of Gold Nanoparticles for Photodynamic Cancer Therapy, MChem Dissertation, University of Liverpool, 2022.

(11) Tao, X.; Li, J.; Möhwald, H. Self-Assembly, Optical Behavior, and Permeability of a Novel Capsule Based on an Azo Dye and Polyelectrolytes. *Chem. - A Eur. J.* **2004**, *10* (14), 3397–3403. https://doi.org/10.1002/chem.200400024.

(12) Tao, X.; Li, J.; Hartmann, J.; Möhwald, H. Self-Assembly and Properties of

Phthalocyanine and Polyelectrolytes onto Melamine Resin Particles. *New J. Chem.* **2004**, *28* (12), 1579–1583. https://doi.org/10.1039/b409993a.

(13) Obfs, T.; Dai, B. Z.; Voigt, A.; Leporatti, S.; Donath, E. Layer-by-Layer Self-Assembly of Polyelectrolyte. **2001**, No. 17, 1339–1342.

(14) Palamà, I. E.; Coluccia, A. M. L.; Gigli, G. Uptake of Imatinib-Loaded Polyelectrolyte Complexes by BCR-ABL+ Cells: A Long-Acting Drug-Delivery Strategy for Targeting Oncoprotein Activity. *Nanomedicine* **2014**, *9* (14), 2087–2098. https://doi.org/10.2217/NNM.13.147.

(15) Song, Y.; Zhou, Y.; Chen, L. Wood Cellulose-Based Polyelectrolyte Complex Nanoparticles as Protein Carriers. *J. Mater. Chem.* **2012**, *22* (6), 2512–2519. https://doi.org/10.1039/c1jm13735b.

(16) Palamà, I. E.; Musarò, M.; Coluccia, A. M. L.; D'Amone, S.; Gigli, G. Cell Uptake and Validation of Novel PECs for Biomedical Applications. *J. Drug Deliv.* **2011**, *2011*, 1–7. https://doi.org/10.1155/2011/203676.

(17) Jeong, Y. J.; Lee, D. Y.; Choe, K.; Ahn, H.; Kim, P.; Park, J. H.; Kim, Y. C. Polypeptide-Based Polyelectrolyte Complexes Overcoming the Biological Barriers of Oral Insulin Delivery. *J. Ind. Eng. Chem.* **2017**, *48*, 79–87. https://doi.org/10.1016/j.jiec.2016.12.022.

(18) Chen, J.; Dong, W.; Möhwald, H.; Krastev, R.; June, R. V. Amplified Fluorescence Quenching of Self-Assembled Polyelectrolyte - Dye Nanoparticles in Aqueous Solution Fluorescent Polyelectrolytes (FPs) Are under Considerable Investigation in View of Their Application as Chemical and Biological Sensors as a Resul. **2008**, No. 10, 1664–1666.

3 AuNP@cit and AuNP@CALNN mediated phototherapy in HeLa cells

3.1 Introduction

S. Chadwick initially showed cell killing in HeLa cells upon irradiation following uptake of AuNP@cit and AuNP@CALNN.[1] This chapter covers further experimental work, in particular expanding the experimental conditions, and a more detailed analysis, which was applied to the new data as well as to the existing data obtained by S. Chadwick to elucidate the mechanisms governing the AuNP@cit, light-mediated treatment. In order to discuss the results obtained experimentally, results reported by S. Chadwick will be presented in this section 3.2 and where reanalysis has been performed as part of the current project the results will be included in the results and discussion section. The experimental methods used by S. Chadwick were identical to the methods used in further data gathering, while a description of the transmission electron microscopy (TEM) techniques can be found in the original reporting of these data.[1]

3.2 Previous Results Obtained by S Chadwick

3.2.1 Uptake of AuNP@cit and AuNP@CALNN

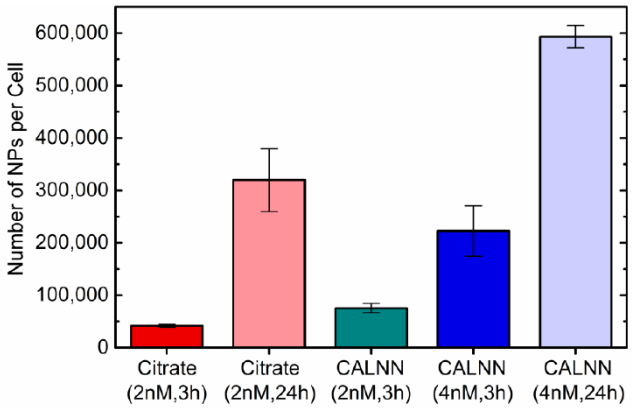

Figure 3.1– Uptake of 13-14 nm AuNPs by HeLa cells with AuNP@cit and AuNP@CALNN at different concentrations and incubation times, the error bars correspond to the standard deviation of individual experiments. Image taken from [1].

Uptake experiments of AuNP@cit and CALNN-stabilised AuNPs (AuNP@CALNN), assessed using ICP-OES, resulted in the values presented in figure 3.1. AuNP@CALNN showed a larger amount of AuNPs associated with the cells, with the number being proportional to AuNP concentration, but saturating in less than a day. The values reported for AuNP@cit are consistent with literature.[2,3]

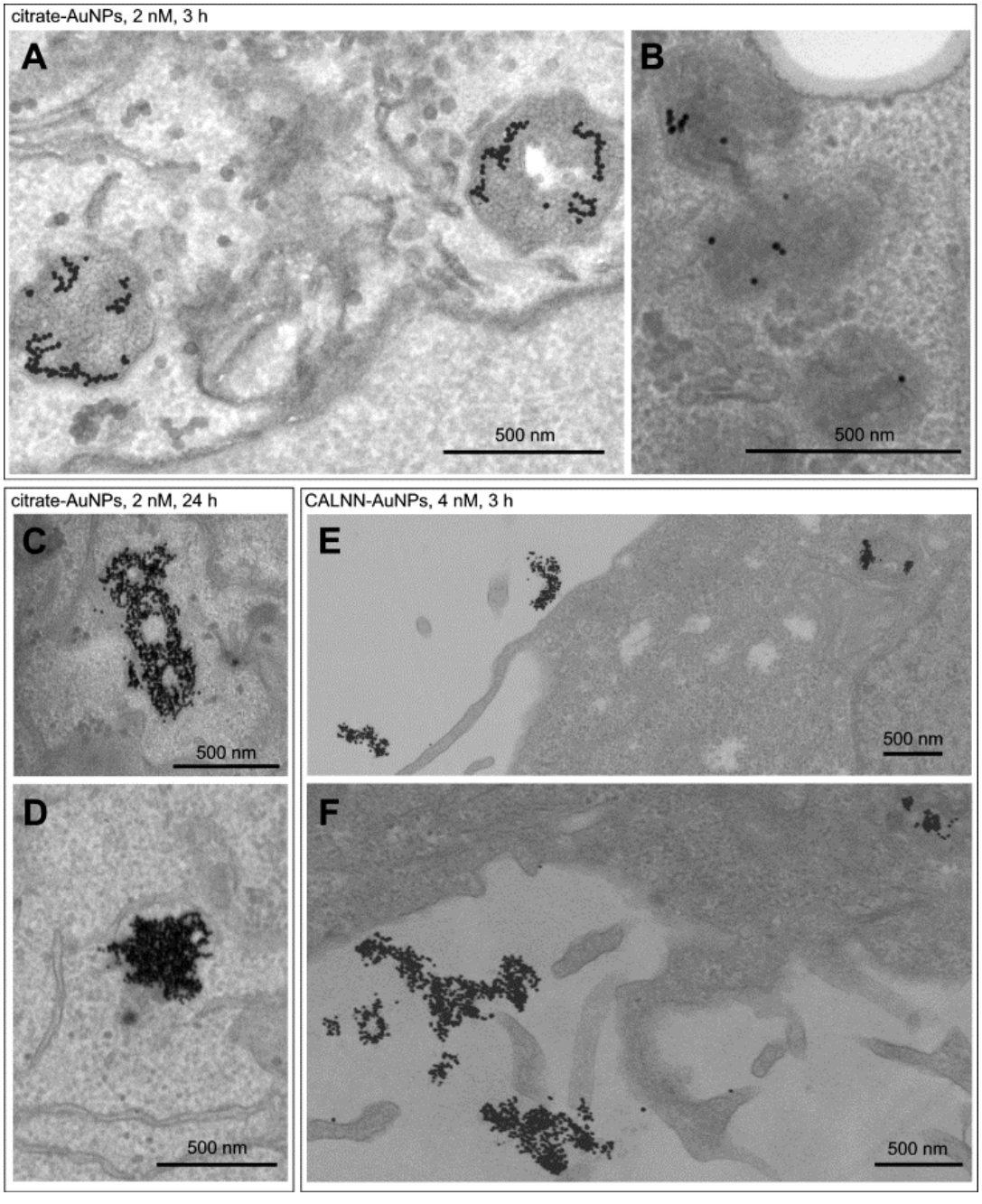

Figure 3.2 - Representative TEM images of HeLa cells after incubation with 2 nM citrate-stabilized 13 nm AuNPs for 3 hours (A, STEM; B, TEM) or 24 hours (C+D, TEM) and with 4 nM CALNN-stabilized 13 nm AuNPs for 3 hours (E+F, STEM). Image taken from [1].

TEM images of HeLa cells following incubation with 13 nm AuNP@cit show AuNPs in intracellular vesicles, including early and late endosomes and lysosomes, figure 3.2, confirming endocytosis as the main mechanism for uptake.[2,4–8] After incubation for 3 hours, both individual and aggregated AuNPs were observed, figures 3.2A and 3.2B, whereas incubation for 24 hours results in extremely dense packing of AuNPs within the vesicles, figure 3.2C and 3.2D. No significant binding of AuNP@cit to the cell surface was observed in these TEM images. In contrast, after incubation with AuNP@CALNN, which leads to a larger number of AuNPs being associated with the cells as detected by ICP-OES, the majority of AuNPs are attached to the outside of the cell membrane rather than in intracellular vesicles, figures 3.2E and 3.2F. This shows that AuNP@CALNN interact with HeLa cells by a different mechanism.

A semi-quantitative analysis of the number of AuNPs in the TEM images provided estimated loadings of between 20,000 and 50,000 AuNPs per cell after incubation with AuNP@cit (2 nM, 3 hours) and approximately 150,000 AuNPs per cell after incubation with AuNP@CALNN (4 nM, 3 hours), which is in good agreement with the ICP-OES results. More importantly, this analysis suggests that only approximately 10% of the AuNP@CALNN which are taken up by cells after repeated washing with PBS are located inside the cells and the majority resides on the cell surface, whereas for citrate-stabilized AuNPs more than 90% of the AuNPs are located inside the cell, in agreement with a previous report for other cell types, which used an analytical method rather than imaging for distinguishing between binding to the cell surface and uptake into the cell.[9] The high AuNP density within the endosomes in cells incubated for 24 hours made it impossible to estimate the AuNP loading from the TEM images.

3.2.2 Determination of Temperature Limit for Thermal Therapy

To determine the required temperature to kill HeLa cells photothermally, dishes were sealed using parafilm and immersed in a water bath.[1]

The effect of elevated temperatures on HeLa cell viability was investigated by immersion of culture dishes in a water bath. Incubation at 40 °C was found to not have any effect on cell viability, whereas keeping the cells at a temperature between

45 and 50 °C for 4 minutes in the absence of AuNPs resulted in a reduction of cell viability to ~0.5 and heating to above 50 °C for 4 minutes reduced viability to 0-0.1, all of which is in good agreement with the effects found for other cell lines.[10–17]

3.2.3 Dynamic Simulations of Temperature Rise in HeLa Cells Containing AuNPs

Dynamic temperature simulations were performed by M. Volk to estimate laser irradiation induced temperature increases for the experiments performed by S. Chadwick and were also applied to results reported in 3.6. The spatio-temporal temperature distribution of the buffer solution above a thin layer of AuNP-loaded cells on a culture dish during irradiation with a laser beam was calculated using finite-element dynamic heat transport simulations based on the Fourier equation, equation 3-1. These were performed using the same method as published.[7]

$$\rho c \frac{\partial T}{\partial t} = \kappa \nabla^2 T + \frac{dq}{dt}$$

Equation 3-1 – Fourier heat equation

In equation 3-1, ρ, c and κ are the density, heat capacity and heat conductivity of the medium, and T is the temperature. dq/dt represents a source term, q is the heat that is released to the medium as a result of the absorbed light energy. The amount of light absorbed is estimated from the absorbance of the sample which can be estimated from the NP per cell, local cell confluency (cell mm^{-1}) and the ε of the AuNPs which is size dependent (for 13 nm AuNPs this is 2.5×10^{-7}).

Figure 3.3 shows a typical example for the increase of temperature upon starting the irradiation, in this case at the maximum intensity available to us, for a cell culture which absorbs 0.3% of the incident light. This absorbance is typical for a HeLa cell culture grown to ~50-80% confluency and incubated with citrate stabilized AuNPs for 3 hours, for which it is in fact impossible to reach temperatures above 37°C, which is the normal incubation temperature for HeLa cells. However, much higher temperatures can indeed be achieved by longer incubation with AuNP@cit or by incubation with AuNP@CALNN (see figure 3.1). Due to the linearity of the Fourier equation, the shape of the spatio-temporal temperature distribution is the same for

all experiments, although the amplitude of the temperature change scales with the amount of heat absorbed, i.e. with the laser intensity applied and the density of AuNPs in the irradiated cell culture area.

It is worth noting that for the laser beam diameter used here most of the temperature increase in the centre of the laser beam is achieved in the initial 30 seconds, followed by a slower phase which is characterized by the heat spreading into the buffer volume, and thus also increasing the area of the cell culture experiencing a significant temperature increase, without a large temperature increase in the centre. This biphasic temperature increase is similar to experimentally observed temperature rises within tumours subjected to AuNP-induced PTT.[10,14,18,19]

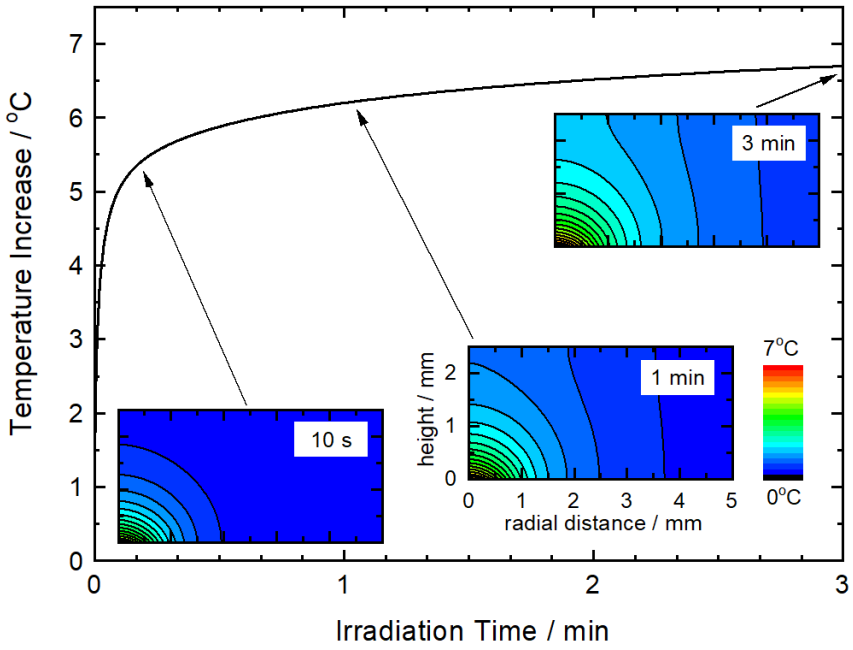

Figure 3.3 - Time-dependent temperature increase of the HeLa cell monolayer at the centre of a laser beam with 210 W/cm^2 intensity and 1.85 mm diameter (1/e^2), for a situation where 0.3% of the incident light is absorbed. (Insets) Contour plots of the spatial temperature distribution in the buffer layer above the HeLa cells after different times of irradiation; horizontal axis: radial distance from the centre of the laser beam; vertical axis: height above the cell layer; for clarity, the horizontal and vertical scales as well as the colour (temperature) scale are shown only for the distribution after 1 min irradiation, the same scales were used for all plots. Image taken from [1].

3.2.4 Light Mediated Cell killing using AuNP@cit and AuNP@CALNN

S. Chadwick investigated the effect of 532 nm, cw laser irradiation (210 W cm-1, 3 minutes) on HeLa cells treated with AuNP@cit (2 nM, 24 hour) and AuNP@CALNN (4 nM, 3 hours). Killing was observed with both AuNPs, where all cells were killed in a large area in the centre of the laser beam, clearly shown by the blue staining in figure 3.4. This result was often found upon irradiation at the highest laser intensity, but only when cells contained large numbers of AuNP@cit (320,000 AuNPs per cell) or AuNP@CALNN (220,000 AuNPs per cell). When the onset of cell death was measured, for these experiments it was typically observed after 1 hour, indicating immediate substantial damage to the cell membrane.

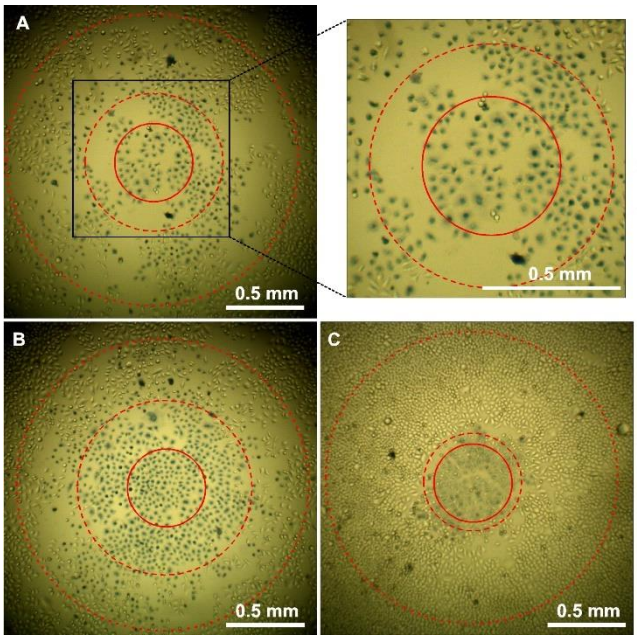

Figure 3.4 - HeLa cells incubated with 13 nm AuNP@cit (2 nM, 24 hours) prior to irradiation at 210 W/cm^2 for 3 min (A, B) or incubated with 13 nm AuNP@CALNN (4 nM, 3 hours) prior to irradiation at 210 W/cm^2 for 1 min (C). All images were taken after trypan blue treatment at 24 hours after irradiation. The red solid circles indicate the centre exposed area with a diameter of 0.5 mm, the dotted circle the 1/e^2 diameter of the laser beam, and the dashed circle indicates the approximate area in which all of the cells are dead. The image to the right of panel (A) is a magnified view of (A), as indicated. Image taken from [1].

In contrast, Figure 3.5 shows experiments where irradiation has resulted in some dead cells whose cell membrane is defective so that they are stained by trypan blue incubation (blue arrows); in addition, some cells have disappeared completely (red arrows), which for HeLa cells normally only happens upon cell death. On the other

hand, interspersed with these cells are cells which have normal morphology and are not stained by trypan blue. Outside of the irradiated area, normal cell splitting was observed. This type of outcome was normally observed after incubation with citrate stabilized AuNPs for 3 hours, irrespective of the irradiation conditions, although cell viability did show a correlation with the irradiation conditions, *vide infra*. However, this outcome was also often found after incubation with CALNN-stabilized AuNPs, particularly when using cell cultures with lower confluency. The onset of death as detected using trypan blue typically took 24 hours, indicating that the membrane wasn't damaged during the irradiation.

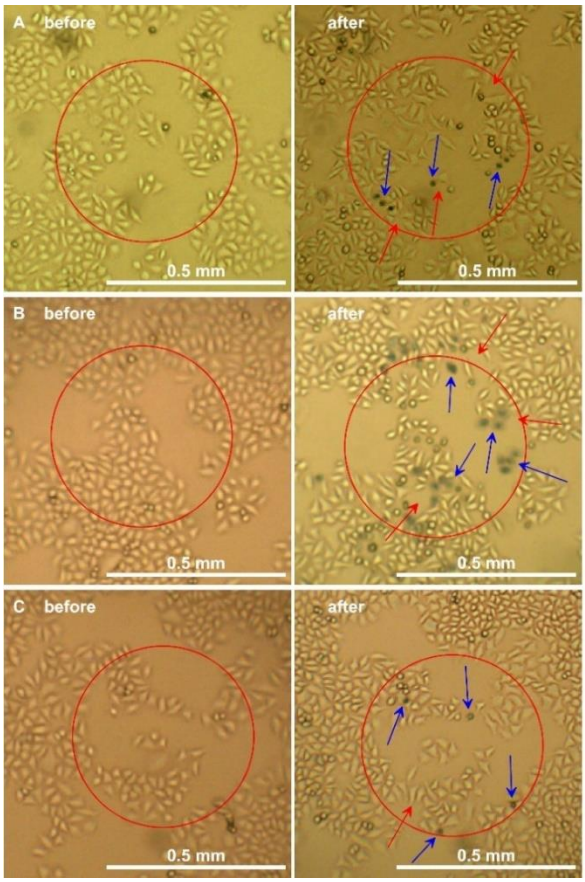

Figure 3.5 - HeLa cells incubated with 13 nm citrate stabilized AuNPs (2 nM, 3 hours) (A) or incubated with 13 nm CALNN-stabilized AuNPs (4 nM, 3 hours) (B, C) prior to irradiation at 140 W/cm^2 for 3 min (A,B) or at 210 W/cm^2 for 1 min (C). For all cases the left image was taken just before irradiation and the right image after trypan blue treatment at 24 hours after irradiation. The red solid circles indicate the centre of the irradiated area with a diameter of 0.5 mm used for cell counting. The blue arrows highlight some of the cells which have been stained by trypan blue, indicating that their cell membrane is compromised, the red arrows show where cells have detached from the dish after irradiation. Image taken from [1].

The different outcomes shown in Figures 3.4 and 3.5 are partly caused by different AuNP loadings and irradiation conditions but cannot be ascribed solely to these factors. In many experiments, different outcomes were found for the same incubation and irradiation conditions, compare Figures 3.4C and 3.5C. In these cases, the only difference between the experiments resulting in complete cell killing and those resulting in a minor reduction of cell viability was the local cell confluency.

The well-defined circular area of complete cell killing which is shown in the examples of Figure 3.4 is reminiscent of results which have been reported previously for AuNP-induced photothermal therapy. [18,20–23] This effect is based on the fact that when AuNPs absorb light, they dissipate virtually all of the absorbed light energy as heat to their surrounding on the picosecond time scale.[24] Given the cell dimensions and the thermal properties of biological material, the released heat then diffuses through the cell on the sub-millisecond time scale, thus rapidly heating the whole volume containing cells and its surrounding; in our case this will mostly heat the buffer which the cells are immersed in, resulting in largely homogeneous heating of buffer and cells in the irradiated area. [7,25,26]

Irradiated cells containing large numbers of AuNPs (figure 3.4) all died and a well-defined area of dead cells is observed. Temperature simulations for these experiments show that cells reach a temperature above 50 °C. This observation is in very good agreement with the results obtained when using a water bath for heating the cell culture dish reported in 3.2.2. However, when cells contained fewer AuNPs (42,000) following an incubation with AuNP@cit (2 nM, 3 hours), this threshold temperature was not reached and viability is reduced with live and dead cells interspersed in only the most intense area of laser irradiation. Due to the short range of singlet oxygen, its cytotoxic effect is limited to the cell it was generated in. This allows live and dead cells to neighbour each other, therefore PDT must be the mechanism for cell killing. Interestingly, for AuNP@CALNN (4 nM, 3 hours) significant killing was only reported when the temperature was above the threshold temperature even though the amount of AuNPs associated with the cells is significantly higher than in AuNP@cit (2 nM, 3 hours).

3.2.5 Summary of Previous Work

Two modalities of cell killing were observed in AuNP@cit and AuNP@CALNN experiments by S. Chadwick. Where cellular AuNP content was high (AuNP@cit: 2 nM, 24 hours) and the temperature reached was above 50 °C, killing was mediated by heating. Where AuNP content was low (AuNP@cit: 2 nM, 3 hours) the temperature reached did not exceed 50 °C and killing was mediated by reactive oxygen generated by AuNPs. For AuNP@CALNN (4 nM, 3 hours) if the irradiation was of sufficient power, the temperature reached was above 50 °C and killing observed was mediated by heating. However, when this temperature was not reached due to lower irradiation conditions or lower cell confluency no killing was observed, despite significantly higher amounts of AuNPs being associated with cells compared to the AuNP@cit (2 nM, 3 hour) experiments. As the majority of AuNP@CALNN are associated with the outside of the cell membrane the reactive oxygen generated is less effective than when it is generated by AuNP@cit.

However, the results presented by S. Chadwick only included a limited analysis of photodynamic killing. This was based on only counting cells that had been stained by trypan blue or detached following irradiation. Also, there was no full comparison of the compensating effects of laser power or irradiation time. As a photodynamic effect is cumulative, lower light doses should still damage cells and lower intensity irradiation over longer time periods should deliver equivalent cytotoxicity to cells while generating lower temperatures within cells.

3.3 Experimental

3.3.1 Materials

Dulbecco's Modified Eagle Medium (DMEM), heat inactivated fetal bovine serum, non-essential amino acids, Penicillin-Streptomycin, trypan blue, and phosphate buffered saline (PBS) (pH 7.4) were purchased from ThermoFisher. Corning cell culture plates and flasks were purchased from Fisher Scientific. AuNP@cit were synthesised and characterised as described in chapter 2.

3.3.2 Cell Culture

HeLa cells were kept in culture in Dulbecco's Modified Eagle Medium (DMEM) supplemented with 10% heat inactivated fetal bovine serum, 1% non-essential amino acids and 1% penicillin-streptomycin in a humidified atmosphere containing 5% CO_2. To maintain consistency passages 4-35 were used for experiments and cells were typically grown to 80% confluency before splitting. During routine cell culture HeLa cells were screened for mycoplasma contamination.

3.3.3 Determination of AuNP Uptake

HeLa cells were seeded in 100 mm cell culture dishes and allowed to attach overnight. Following this, they were incubated with a 1:1 (v/v) mixture of cell culture medium (CCM; Dulbecco Modified Eagle's Medium, DMEM, supplemented with 10% fetal bovine serum, FBS) and AuNP solution, prepared 24 hours before incubation, at different AuNP concentrations and for different times. The cell layer was washed three times with 10 mL of PBS (pH 7.4), detached with 1 mL of trypsin and 9 mL CCM was added. The concentration of cells in the solution was assessed using a haemocytometer, after which the solution was centrifuged at 1000 rcf for 10 minutes. The supernatant was removed and the cell pellet was dissolved in 0.5 mL of freshly prepared aqua regia. After 3 days, this was diluted with 4.5 mL H_2O and the gold content of the sample was determined using ICP-OES and used to calculate the number of AuNPs per cell.

3.3.4 Irradiation of HeLa cells and Determination of Cell Viability

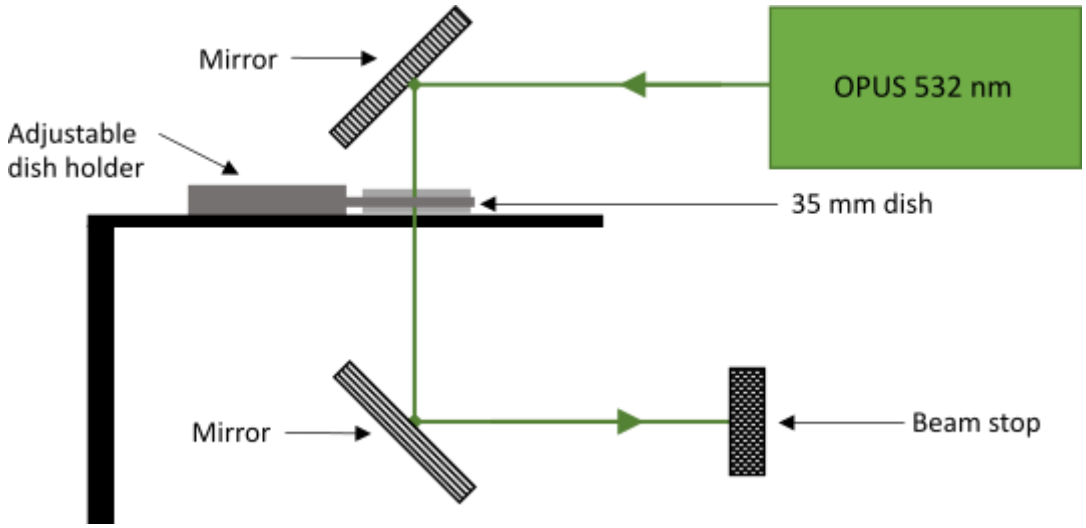

Figure 3.6 – Laser irradiation set up for the irradiation of HeLa cells in 35 mm dishes (side view). The dish was centred using a sticker, and then moved using micrometre screws to irradiate a specific area of the dish. Typically, four areas on each dish were irradiated, except when longer irradiation times were used.

HeLa cells were seeded on a 35 mm cell culture dish and left to attach overnight. They were then incubated with a 1:1 (v/v) mixture of CCM and AuNP@cit at a final AuNP concentration of 2 nM or for control experiments a 1:1 (v/v) mixture of CCM and H_2O, using the same protocol as described above. At the end of the incubation time, cells were imaged using a microscope and washed three times with PBS and then irradiated with cw laser light at 532 nm. In most cases, they were then kept under standard growth conditions under CCM for 24 hours, after which the CCM was replaced with a 1:1 (v/v) mixture of CCM:trypan blue (0.4%) and replaced in the incubator for 5 minutes. The cells were then washed twice with PBS, 1 mL of CCM was added to the dish and the cells were imaged using a microscope. The number of live cells, identified by the absence of staining or significant morphological changes, was counted in a circular area with a diameter of 0.5 mm around the centre of the laser beam, for the images taken prior to and 24 hours after irradiation. These numbers were used to calculate cell viability, by comparing their ratio to the expected growth rate, obtained from a non-irradiated control area on the same dish.

To image and irradiate the correct areas reliably, a micrometre stage was used. A sticker with a hole was placed in the centre of the dish, to which the microscope or

laser were aligned. The area also provided an unirradiated control area. From this alignment, the stage was moved by a precisely controlled movement of the translation stage to image and irradiate cells.

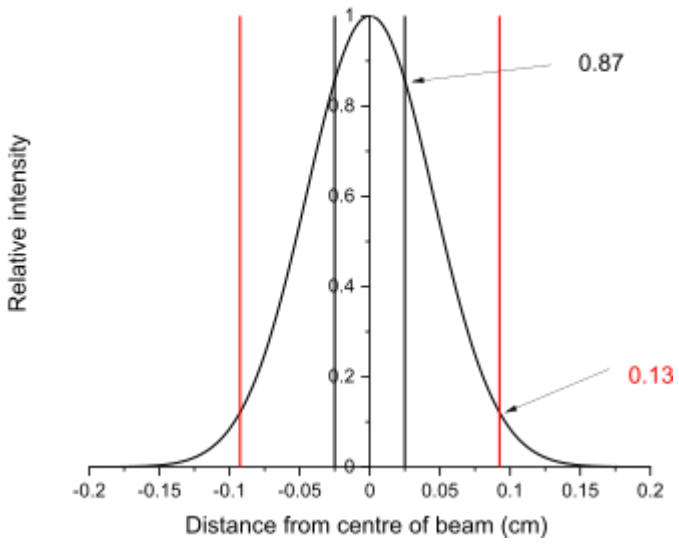

Figure 3.7 – Beam profile of a laser with a $1/e^2$ diameter of 1.85 plotted as relative intensity to the maximum intensity. The black lines indicate the power in the central 0.5 mm and the red line indicates the power at 1.85 mm.

As the Opus 532 nm cw laser used has a $1/e^2$ beam diameter of 1.85, only the central area with diameter 0.5 mm was assessed as the laser intensity at the edge of this area remains 87% of the maximum intensity.

3.3.5 Development of viability assay

The results reported by S Chadwick were reported as cell killing, this is summarised in equation 3-2.[1] The amount of dead and detached cells 24 hours after irradiation were counted and expressed as a percentage of the amount of cells present in an area before irradiation. This can be seen in equation 3-2. These dead cells were assessed using trypan blue, which stains cells with permeabilised membranes blue. This is typically an indicator of necrosis, however in these experiments it also detects cells that show secondary necrosis due to the time delay of 24 hours before assessment. This occurs when cells are killed via pre-programmed routes (apoptosis and autophagy) and have intact membranes but are not removed by the mechanisms that would typically occur in vivo. This results in the loss of cell function gradually

leading to loss of membrane integrity and the ability of trypan blue to stain these cells.

$$Cell\ Death\ Rate\ = \frac{Dead\ Cells\ 24\ Hours\ after\ irradiation}{Live\ Cells\ Before\ Irradiation}$$

Equation 3-2 – Method of reporting cell death rate used by S. Chadwick.

While this is important, more widely used assays such as clonogenic and MTT assays typically measure the growth of cells compared to a control area. This allows the consideration of damaged cells that lose their ability to divide and replicate without undergoing primary or secondary necrosis and hence were not detected in the analysis performed previously. This is a significant effect when we are considering the efficacy of a treatment. As these typically treat the whole of a cell population, they cannot be applied to these experiments as only a small fraction of cells is irradiated. An MTT assay was used in chapters 4 and 5. In order to improve our assessment of cytotoxicty, we developed an assay allows the determination of viability, giving results that are analogous to those widely used assays but is applicable to our conditions. We compared the number of cells in a control area on the same dish before and after irradiation to calculate the growth rate of cells in the absence of irradiation. The cells in the irradiated area were counted before irradiation, and the number of healthy cells were counted after irradiation. The growth rate was applied to cell count in the irradiated area before irradiation and the number of healthy cells following irradiation was compared to this number to display viability. This is summarised in equation 3-3 and 3-4.

$$Viability = \frac{Live\ Cells\ 24\ hours\ after\ irradiation}{Cells\ Live\ Before\ Irradiation\ \times Growth\ Rate}$$

Equation 3-3 – Determination of viability used in the results presented in this chapter.

$$Growth\ Rate = \frac{Live\ Cells\ 24\ Hours\ Later\ (control)}{Live\ Cells\ Before\ Irradiation\ (control)}$$

Equation 3-4 – Determination of growth rate as used in equation 3-3.

3.3.6 Measurement of Average Cell Size in Irradiated Areas

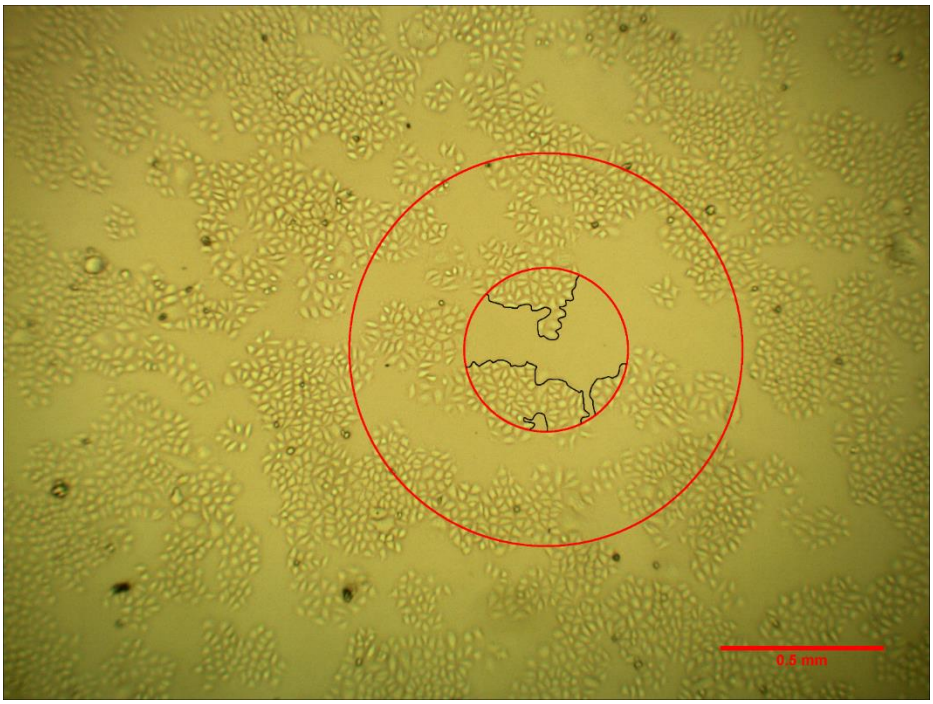

Figure 3.8 – Measurement of area occupied by cells in the central area of a cell irradiation. The red circles indicate diameters of 0.5 mm and 1.2 mm, respectively.

In order to determine the average cell size in an irradiated area, the area was imaged in the CCM:AuNP mixture before irradiation. They were imaged in this mixture rather than PBS as PBS reduced the size of cells. The area occupied by cells was traced, an example of which can be seen in figure 3.8, and the area was analysed in imageJ to give the area occupied by cells. This was then divided by the number of cells in the area to give the average area occupied per cell.

3.4 Uptake of AuNP@cit and its Variability

3.4.1 Uptake of AuNP@cit by HeLa cells

On exposure of AuNP@cit to the CCM, the citrate capping layer is displaced by a corona formed from the FBS proteins, which stabilizes the AuNPs. [3,4,27,28] This corona increases gradually during the 24 hour exposure of AuNPs to CCM prior to their application to cell cultures to yield an overall thickness of ~15 nm.[3,27] However, DCS results obtained in our group show that the "hard" corona, i.e. the tightly bound fraction of this corona which remains in place upon transferring the AuNPs into a

different environment, has a thickness of only 8 nm, is formed within one hour and does not increase significantly by prolonged incubation, in agreement with previous results obtained in almost undiluted CCM.[28,29] This shows that a significant fraction of the protein corona of AuNPs in DMEM/FBS consists of proteins which are only loosely bound ("soft" corona). Moreover, the "hard" serum protein corona is thicker than that formed upon exposure of AuNPs to neat bovine serum albumin (BSA), the most common component of FBS, which confirms that lower abundance proteins are preferentially bound into the corona.[30] It is reasonable to suggest that this corona mimics the protein corona which systemically administered AuNPs would pick up in the blood stream.

The uptake of AuNP@cit in HeLa cells (incubated with 2 nM, 3 hours) determined using ICP-OES to provide a mean uptake of 42,000 per cell. This is in good agreement with values reported in literature for HeLa cells incubated under similar conditions and with the results presented in 3.2.1. While this average value is consistent with those reported in literature, it only provides an average value for the entire cell population. Determination of the uptake of single cells in literature shows significant variation within the cell population, which arises from a variation of the rate of AuNP binding and uptake, e.g. due to variations of the density of endocytotic receptors and the cell size as this dictates the surface area of the cell exposed to the AuNP solution. The size in turn, is influenced by confluency.[31–34]

In order to probe the impact of confluency on AuNP@cit uptake by cells, the total numbers of cells in dishes assessed using ICP-OES was varied between non-confluent and confluent conditions, which provides a simple method of reducing the average cell area exposed to the medium containing AuNP@cit.[35]

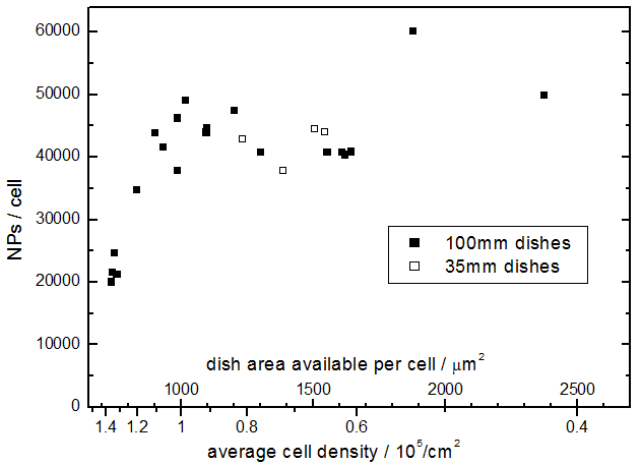

Figure 3.9 – Uptake of 13-14 nm AuNP@cit by HeLa cells after incubation with AuNP@cit (2 nM, 3 hours) on dishes with a wide range of confluencies. The x-axes represent the cell density, which is the amount of cells per area, and the available dish area available per cell, which represents the largest surface area of a cell in these conditions. These were determined from the total cell count obtained during the uptake analysis and the available growth area on a 10 mm cell culture dish.

At low confluency, the area occupied by each cell is expected to decrease only slightly as the number of cells increases, since new cells have enough space to move away from their parent cell.[35] Thus not much change in AuNP uptake is expected; this is in agreement with the results in Figure 3.10, which show only a slight decrease of the number of AuNPs per cell with increasing cell density below 10^5 cells/cm^2. Upon reaching full confluence, above 10^5 cells/cm^2, the average cell size drops rapidly when further increasing cell density, and this is accompanied by a significant decrease of the number of AuNPs per cell; for the highest cell density used here, the number of AuNPs per cell drops to less than half of the value observed for unrestricted cells. As the amount of AuNP@cit contained in the medium is 2×10^{-11} moles and the total amount of AuNP@cit taken up by cells is on the order of 3×10^{-13} moles, this reduction in uptake is unrelated to increased total uptake of AuNP@cit reducing the amount of AuNP@cit available to the cells.

3.4.2 Cell size Analysis

As the AuNP@cit irradiation we describe in this chapter only treats a small section of cells (0.20 mm^2) contained within a larger dish (962 mm^2), the local cell confluency can be significantly different to the overall confluency of a dish. A more detailed

analysis of the cell size used microscopic images, comparing 0.5 mm circular areas of HeLa cells, as can be seen in figure 3.10. In low cell density dish images, cells were found to occupy on average an area of around 1500 μm^2, similar to the cell area reported for other epithelial cell lines.[35] On the other hand, for essentially confluent dishes, the cells occupied on average an area of only 600 μm^2, close to the lowest dish area available per cell in the AuNP incubation samples, Fig. 3.9. In these experiments, cells had been grown at most long enough to reach confluency; significantly lower cell areas can be found upon prolonged cell culture growth, in agreement with literature reports.[35] Thus, the extremes of our cell growth conditions (low cell density to just reaching confluency) lead to a variation of the average area occupied by an individual cell by a factor of 2.5, which is very similar to the accompanying variation of AuNP numbers per cell, suggesting a close-to-linear relationship between the cell surface area and the number of AuNPs that bind to the cell, which is expected since a smaller surface area means that less endocytosis receptors are exposed to the medium containing AuNPs. It should be noted that this relationship only refers to the average AuNP uptake of a cell population of identical size; single cell experiments have shown a significant variability of AuNP binding even for cells of the same size due to other effects, most likely a variability of endocytosis receptor density.[31–33,36] As will be discussed in more detail below, this variability in AuNP binding and uptake presents difficulties in assessing the effectiveness of cytotoxic therapies mediated by AuNPs.

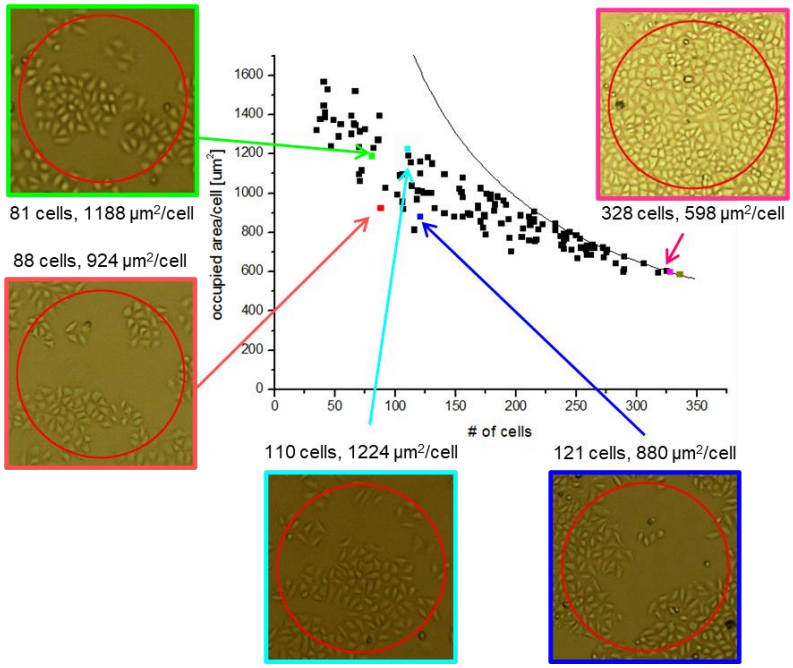

Figure 3.10 - Average occupied area per cell in 0.5 mm areas determined as described in 3.3.6, plotted against the number of cells within the areas. Images of selected areas are shown, with the red circles indicating a diameter of 0.5 mm. The solid line shows the total area available per cell.

3.5 Control experiments

3.5.1 Control irradiations

In the absence of AuNPs, irradiation of HeLa cells with cw laser light at 532 nm at the maximum intensity available (210 W/cm^2) for up to 5 minutes does not significantly affect the cells. 24 hours after irradiation the trypan blue assay does not reveal any dead cells and the cells have normal morphology, see figure 3.11. Moreover, the cells have undergone significant splitting, although a quantitative analysis shows that overall cell viability is reduced to 0.85 $\pm$ 0.08 for 3 min irradiation, compared to cells on the same dish that had not been irradiated, which showed the normal growth rate. Data for other irradiation conditions are shown in Table 3-1, which show that decreasing the laser intensity reduces the effect of irradiation, and that for the same cumulative dose the effect is larger for longer irradiation times at lower dose. This result is in agreement with literature reports that *in vitro* irradiation of various benign and malignant cell types with green or orange cw [37–39] or pulsed light has no or only

minimal effects on their viability, even at intensities comparable to those used here.[37–40]

Intensity (W cm^{-2})	Time (minutes)	Light dose (J cm^{-2})	Viability
210	5	1050	0.74 ± 0.06
210	3	630	0.85 ± 0.08
140	3	420	0.91 ± 0.02
70	3	210	0.90 ± 0.06
210	3	630	0.85 ± 0.08
42	15	630	0.67 ± 0.04
21	30	630	0.55 ± 0.07

Table 3-1 – Viability of HeLa cells 24 hour after irradiation with 532 nm cw laser light in the absence of AuNPs at various intensities and irradiation times.

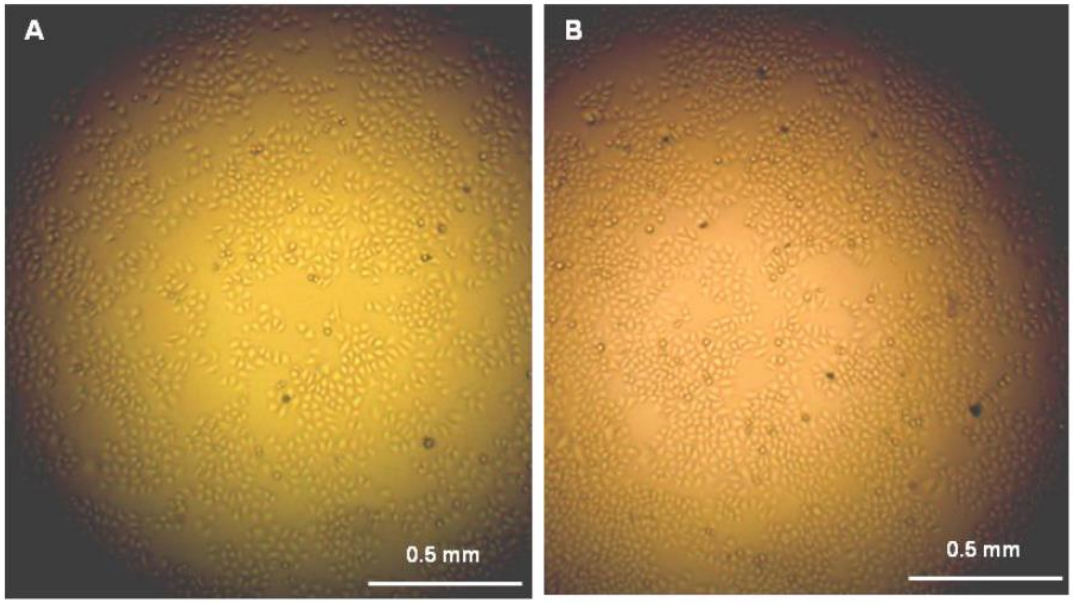

Figure 3.11 HeLa cells in the absence of AuNPs; (A) before and (B) 24 hours after irradiation with 532 nm light at an intensity of 210 W/cm^2 for 5 minutes; trypan blue assay was performed just before taking the image shown in (B).

3.5.2 Effect of AuNP@cit and AuNP@CALNN incubation

HeLa cells incubated with 13-14 nm AuNPs continue to split and proliferate at almost normal rates, and application of trypan blue 24 hours after exposure of the cells to

AuNPs did not result in staining of cells, indicating that all cells had an intact cell membrane at this time.

Quantitative analysis shows that the cell growth rate, i.e. the increase of the number of cells over 24 hours, is slightly reduced after incubation with AuNP@cit for 3 hours, compared to cell dishes which were exposed to a 1:1 (v/v) mixture of CCM and H_2O for the same time, from 2.04 ± 0.08 to 1.68 ± 0.19, which is in agreement with previous reports for the incubation of HeLa cells with AuNP@cit under similar conditions.[3,41] In light of the absence of trypan blue staining, it is tempting to ascribe this effect to a slightly reduced rate of cell splitting with no direct cytotoxicity. However, it is possible that the effect results from a few cells undergoing apoptosis, which are not stained by trypan blue, rather than a reduced rate of cell splitting. This suggestion is based on the observation that the effect of citrate AuNPs on the proliferation of human dermal fibroblasts, which is similar to the one observed here for HeLa cells, is due to cells undergoing apoptosis.[42] The same study also showed that once 13 nm AuNPs are removed from the CCM, non-apoptotic cells rapidly recover even after prolonged exposure to AuNPs . Incubation with AuNP@CALNN, on the other hand, did not lead to any measurable reduction of cell viability, neither did incubation with citrate alone.

3.6 Irradiation of HeLa Cells Containing AuNPs

3.6.1 Summary of Photodynamic and Photothermal Heating Observed in HeLa Cells Using either AuNP@cit or AuNP@CALNN

In order to correlate our results quantitatively with the temperature increase caused by the irradiation and thus confirm the cause of cell death as photothermal heating, we performed numerical simulations. For each individual irradiated area the fraction of incident light which is absorbed by the AuNPs was calculated based on the local density of cells and the number of AuNPs taken up by each cell, figure 3.12. The explicit spatio-temporal temperature distribution in the dish during irradiation was calculated using finite-element dynamic heat transport simulations based on the Fourier equation, as discussed in 3.2.3.[7,25] It is worth noting that for the laser spot

size used here, most of the temperature increase in the centre of the laser beam is achieved in the 30 seconds of irradiation, although the affected area grows with time.

Figure 3.12 correlates the observed viability and the calculated temperature in the maximum of the laser spot at the end of the irradiation for all experiments, which use different types of AuNP coatings, AuNP incubation times and irradiation conditions. From these results, it is obvious that whenever the cells are heated to above 50 °C, they all die, whereas when the maximum temperature is below 45°C cell viability may be reduced, but in most cases we did not observe complete cell killing. In a transition region between these two temperatures, both outcomes were found, although this might be partly due to the uncertainty of our temperature estimates. This observation is in very good agreement with the results obtained when using a water bath for heating the cell culture dish. Therefore, we conclude that under conditions where irradiation results in a temperature above 45-50 °C all cells are killed by the photothermal effect. However, a significant reduction of cell viability, up to almost complete killing, was also found in experiments where our temperature estimates rule out significant heating. This effect must arise from a photochemical effect, and we suggest this to be the photogeneration of singlet oxygen by AuNPs.[43–49]

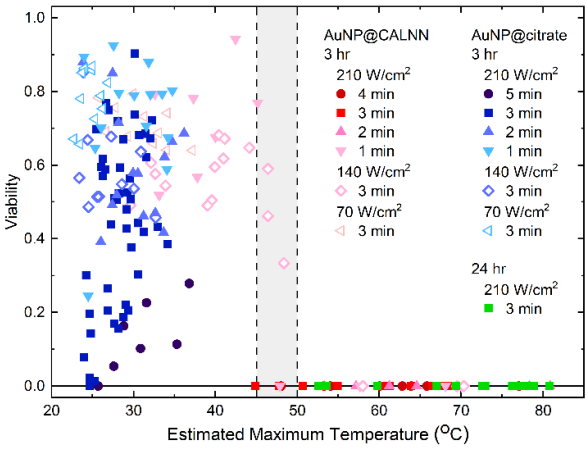

Figure 3.12 - Viability of HeLa cells after incubation with 13 nm citrate or CALNN-stabilized AuNPs and irradiation at different laser intensities for different times. The viability data are plotted against the calculated temperature in the center of the laser spot at the end of the irradiation. The grey area indicates the temperature range below which immersion in a water bath does not affect cell viability, whereas immersion above this range leads to essentially complete killing of cells.

3.6.2 Variation of Cell Killing Caused by Confluency Variation

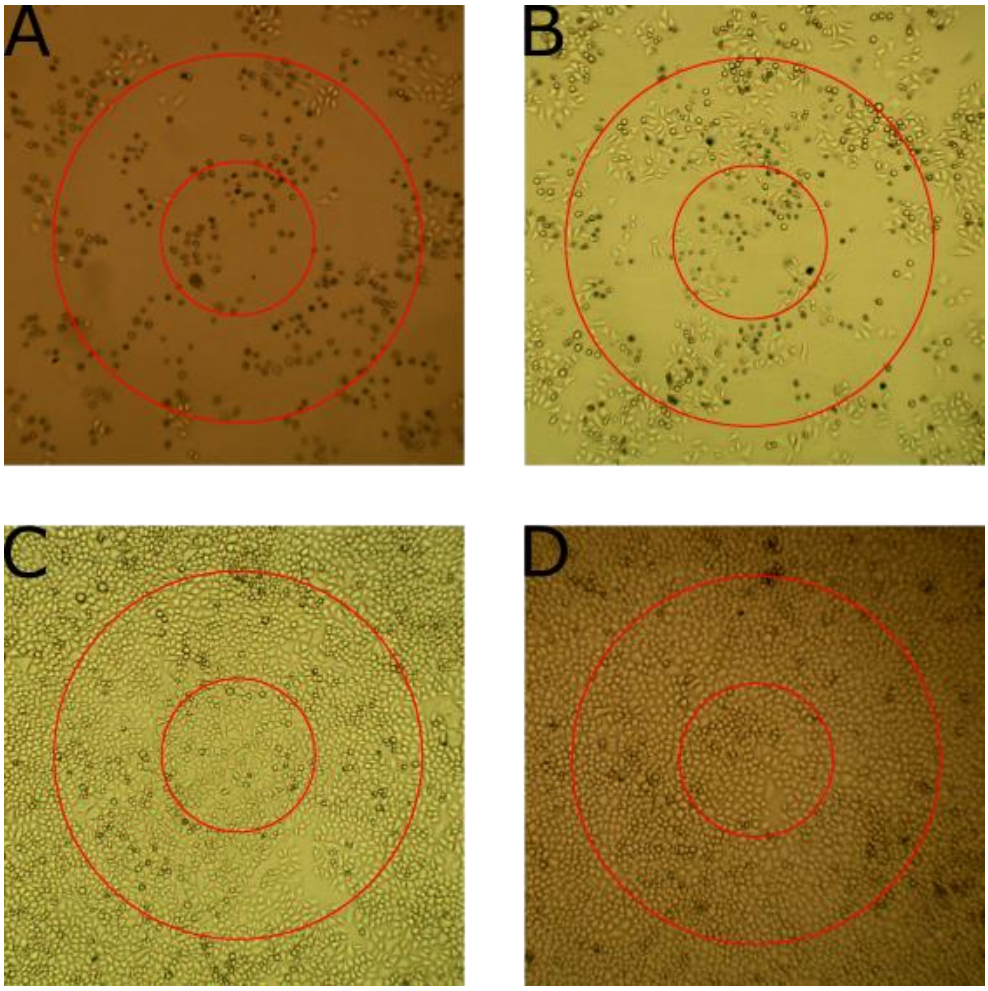

Figure 3.13 – HeLa cells incubated with 13 nm AuNP@cit (2 nM, 3 hours) 24 hours after irradiation with 210 W cm^{-2} for 3 minutes and immediately after treatment with trypan blue. The red solid circles indicate the centre with exposed area with a diameter of 0.5 mm and 1.2 mm. Dead cells can be seen by blue staining and in some cases deformation which typically only occurs in HeLa cells when cells are dead.

Results gathered by S Chadwick within the group showed extensive variation of cell killing. In order to investigate this effect, HeLa cells were treated with AuNP@cit (2 nm, 3 hours) and irradiated with 210 W cm^{-2} for 3 minutes. Cells were replaced in the incubator for 24 hours and assessed using a trypan blue assay, optical microscopy images of irradiated cells can be seen in figure 3.13. Cells are killed throughout the central section, however there are healthy cells alongside dead cells which indicates that reduction in viability is not caused by heating effects. As mentioned in section 3.2.4 if the cytotoxic effect is mediated by heating, it is unlikely that a population of live and dead cells would be distributed together. In addition to this experimental

observation, the simulations also show that heating is insufficient to damage cells containing 42,000 AuNP@cit. The number of cells present before irradiation and the final viabilities for these areas is as follows: A) 67 cells, 0.0, B) 121 cells, 0.24, C) 206 cells, 0.90 and D) 276 cells, 0.56. While significant numbers of dead cells can be seen in A and B, there are very few dead or missing cells in C and D but despite this, there is reduced viability in C and significantly reduced viability in D. This highlights the benefits of reporting viability rather than the amount of dead cells in elucidating the true efficacy of the treatment.

The overall viability of these experiments (51 unique areas) can be seen in figure 3.14A, this value is consistent with the results reported by Chadwick, however significantly more variation in the number of cells in each area is contained in the new data. During analysis it became clear that when irradiated areas had a high confluency, only a few cells were stained by trypan blue. The individual results contained in figure 3.14A are plotted in figure 3.14B against the number of cells within the irradiated area before irradiation; it becomes clear that when low confluency areas are irradiated, the viability is typically reduced significantly as indicated by the lack of data points in the blue area. Conversely, when high confluency areas are irradiated, the effect on viability is reduced, as indicated by the lack of data points in the red area. As reported in section 3.4, increasing the confluency in a 0.5 mm diameter area significantly reduces the cell size, and hence AuNP uptake area of cells. This reduced cell size and AuNP uptake in high confluency areas appears to result in increased viability under otherwise identical irradiation conditions.

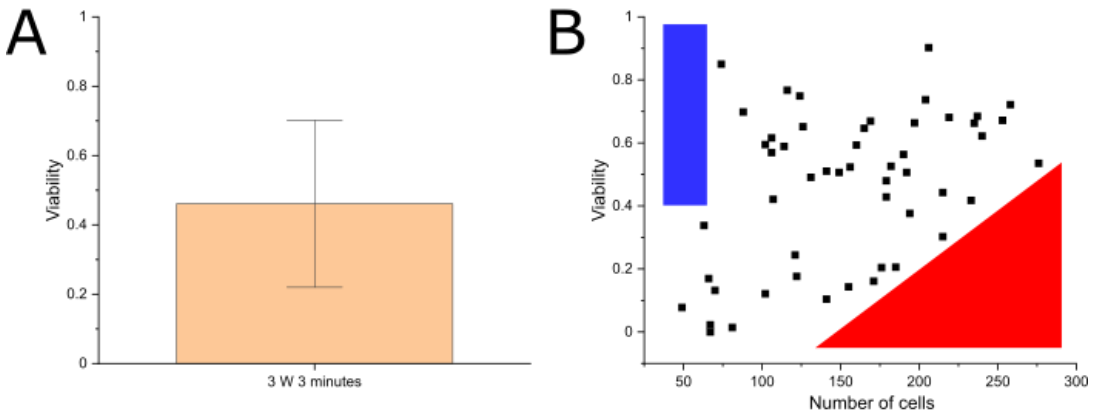

Figure 3.14 – A) The effect of 210 W cm^2, 3 minute irradiation on cells incubated with 13 nm AuNP@cit (2 nM, 3 hours), the error bars correspond to the standard deviation of individual experiments B) The viability of individual areas (contained within A) plotted against the number of cells in the irradiated central section (diameter 0.5 mm)

3.6.3 Effect of Local Confluency Variation upon Cell Viability

The analysis of irradiation conditions presented in 3.6.2 still shows a large range of viabilities when areas contain the same number of cells, figure 3.15B. As an example, individual images of selected experiments can be seen in figure 3.15. The irradiated areas contain similar numbers of cells, however the irradiation of 3.15A reduced the viability significantly more than irradiation of 3.15C. It can be seen that due to local confluency variations area A has significantly larger cells compared to the smaller, more densely packed cells in C. When the average cell area was measured as in section 3.3.6, there is a significant difference between A (1231 µm^2) and C (908 µm^2) and we suggest this explains the difference between the viabilities observed in these areas. A further examination of the individual cells before irradiation indeed shows that the largest cells are likely to die, whereas the smaller cells are more likely to survive.

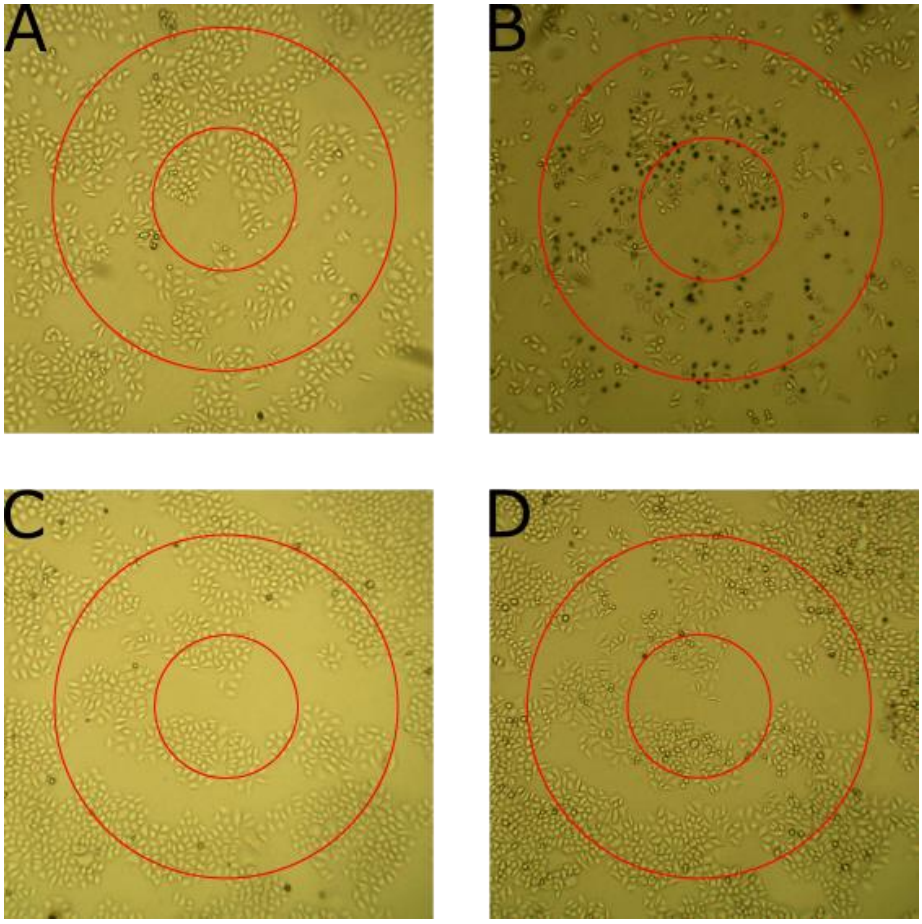

Figure 3.15 – HeLa cells incubated with 13 nm AuNP@cit (2 nM, 3 hours), before irradiation (A, C) and 24 hours after irradiation (B, D). the left image was taken just before irradiation and the right image after trypan blue treatment at 24 hours after irradiation. The viabilities of B, D and the corresponding number of cells before irradiation in A, C were (B,A) 0.18 and 122 cells, (D,C) 0.77 and 116 cells, respectively . The red solid circles indicate the centre exposed area with a diameter of 0.5 mm used for cell counting.

Considering the reduction in AuNP@cit uptake when the available surface area per cell is constrained, each irradiation experiment was assessed to provide an average cell surface area, figure 3.16. This significantly reduces the variation present compared to assessing the experiments using just the number of cells and there is a clear correlation between the average cell surface area in a particular area and the observed viability following irradiation. Areas containing cells with a high local confluency, and hence smaller cell surface area, are significantly less affected than areas containing low local confluency. Literature has shown significant differences in cell biology, including endocytosis, due to the physical properties of cells, and we suggest that the reduced AuNP@cit uptake in constrained cells is responsible for the

reduction in killing.[50] Simply, fewer AuNP@cit associated with a cell results in less light being absorbed, less singlet oxygen generation and consequently a lower likelihood of cell death.

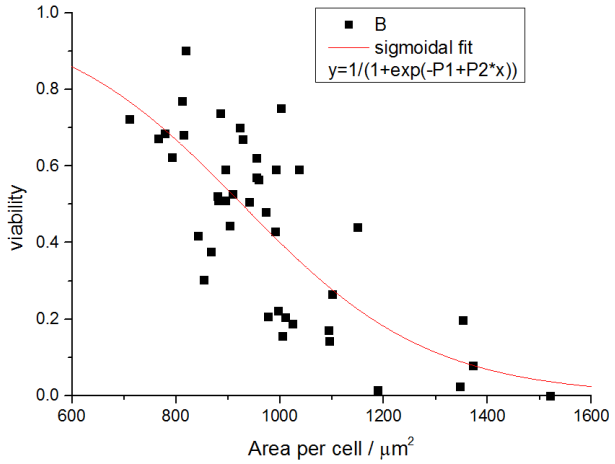

Figure 3.16 - Viability of HeLa cells after incubation with 13 nm citrate stabilized AuNPs for 3 hours and irradiation at 210 W/cm² for 3 min. The viability data are plotted against the average cell area per cell for each individual experiment.

However, the local cell confluency reported above does not precisely determine the viability, and a significant variation of variability is still present, particularly in the transition region around 900-1100 μm², with viabilities varying between 0.17 and 0.75. This can be ascribed to the distribution of cell sizes within similar average cell areas, distribution of AuNPs within endosomes, the distribution of endosomes within cells and inherent variability in cellular processes.

If we consider the whole cell population, each area contains cells of different sizes, figure 3.14. Even if the cellular uptake of AuNP@cit is linearly correlated to the cell area and hence singlet oxygen generated upon irradiation, different cell size distributions with the same average cell size will result in different viability outcomes because of the binary nature of cell death. Our analysis is limited to determining the average cell area, but different size distributions of cells can be present at the same local confluency leading to variation in viability. For example, hypothetical cell areas **A** and **B** shown in table 3-2 both contain 15 cells with an average cell area of 1000 μm². **A** contains a small number of large cells and many small cells and **B** contains cells that are closer to the average size. If cells with a surface area of just over 1000 μm² contain enough AuNPs to kill the cell upon irradiation, whereas cells with a

smaller surface area are not affected, area **A** would have a viability of 80% while area **B** would have a viability of 33%.

Cell area μm^2	900	1000	1100	1400
Area A	12	0	0	3
Area B	5	5	5	0

Table 3-2 – Distribution of individual cell sizes in two hypothetical cell areas containing 15 cells with an average cell area of 1000 μm^2, but a very different distribution, resulting in very different viabilities, see text

Unfortunately, the quality of our captured images prevented a more detailed (single cell) analysis.

On the basis of individual cells, while cell area can provide a reasonable prediction of cell death, there are several factors that influence the efficacy of a photodynamic treatment with AuNP@cit.

i) TEM images of HeLa cells containing 42,000 AuNP@cit show that both aggregated and individual AuNP@cit are found in intracellular vesicles, see figure 3.2. Aggregated AuNP@cit have been shown to be less effective at disrupting these vesicles, possibly due to restricted access of O_2 to the gold surface or the rapid quenching of photoinduced $^1O_2$.[7] The random distribution of individual and aggregated AuNP@cit will increase the variability of the resulting cytotoxic effects.

ii) The spatial distribution of AuNP@cit containing vesicles will vary from cell to cell. Due to the short lifetime of singlet oxygen and its resulting short diffusion distance, this may contribute significantly to the viability variation since the susceptibility of different cell organelles for triggering cell death upon exposure to singlet oxygen varies significantly.

iii) Finally, most cellular processes show significant cell-to-cell variability, which can be partly related to the phenotypic state or population context of individual cells, independent of cell size.[51] In particular, it has been reported that the density of receptors on cell surfaces has significant cell-

to-cell variability, which leads to significant variability of nanoparticle uptake even when corrected for cell size.[31–33,52]

3.6.4 Varying light dose

As $^1O_2$ is generated by AuNP@cit with no photobleaching, the dose received by cells treated with AuNP@cit should be cumulative. As the light dose is changed, the production of $^1O_2$ will change proportionally. In order to prove this, the light dose was varied between 12.6 J cm^{-2} and 63 J cm^{-2}. The results of this can be seen in figure 3.17, with further reduced viabilities at higher doses and higher viabilities at lower doses. Each result is presented as cumulative light energy incident on the cell which is a product of the laser intensity, average cell size and irradiation time.

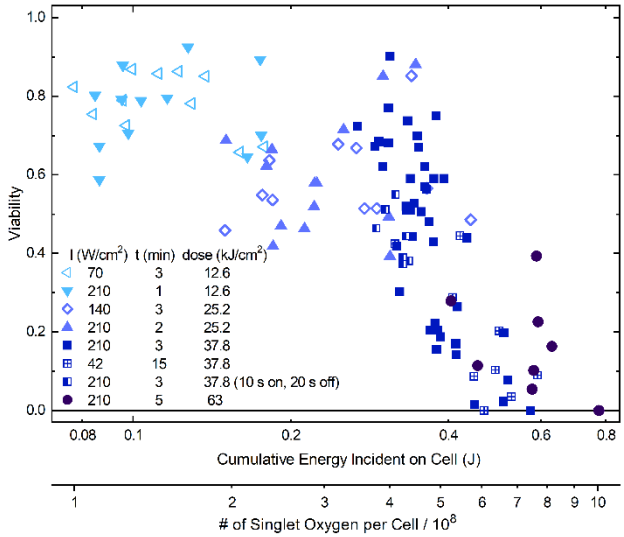

Figure 3.17 - Viability of HeLa cells after incubation with 13 nm citrate stabilized AuNPs for 3 hours and irradiation at different laser intensities and irradiation times, plotted against the cumulative light energy to which the average cell was exposed in the experiment, calculated from the product of average cell area, laser intensity and irradiation time. The second x-axis provides a rough estimate of the number of singlet oxygens produced during irradiation, as described in the text.

This experiment also provides further evidence that the cytotoxic effect proceeds via a photodynamic mechanism rather than a photothermal one. Due rapid heat diffusion, see figure 3.3, most of the heating occurs in the first 30 seconds of irradiation, so that if a cell receives the same light dose delivered over a longer period with a lower intensity the heating of the cells is significantly reduced. The results

presented here show no difference in effectiveness between the same light dose delivered over different timespans.

It appears that exposure of a cell to a cumulative dose of around 0.4 J defines a threshold for these incubation conditions, below which only a small fraction of cells are affected by irradiation, whereas above it a significant fraction is killed, which can reach up to 100% for the larger cells found under low local confluency conditions. We want to stress that this is the dose incident on a cell, not the amount absorbed by it, which is several orders of magnitude lower, depending on its AuNP content. The amount of light absorbed by the AuNPs is not dependent on the size of the cell, as only a small fraction of light passing through the cell is absorbed, so a larger cell with the same AuNP content as a smaller cell will absorb the same amount of light.

3.6.5 Comparison of AuNP@cit to Conventional Photosensitisers

The quantum yield of photogeneration of $^1O_2$ (SOQY) in aqueous solution by citrate AuNPs has been shown by work within our group to be $\phi NP = 1.7 \times 10^{-7}$.[53] A quantitative analysis of our 210 W cm^{-1}, 5 min conditions shows that the AuNPs within each cell (with an absorption cross section of 8.5×10^{-13} cm^2) absorb 6×10^{15} photons over the 5 minute irradiation and generate 1×10^9 $^1O_2$ molecules.

As with any such calculations, this at best can be described as an estimate, not least because the SOQY depends on the concentration of O_2, which may be different in cells compared to air-saturated aqueous solution, for which it was determined.

The threshold for a high rate of killing occurs when 1×10^9 $^1O_2$ molecules are generated within cells, which, taking into consideration the volume of a HeLa cell, yields a cumulative concentration of $^1O_2$ of ~1 mM, which is in good agreement with the cumulative $^1O_2$ concentration required to kill a cancer cell using conventional PSs reported in the literature, as shown in table 3-3. Thus, we can be confident that the mechanism for cell killing is similar to conventional organic photosensitisers.

Cell type	Cumulative $^1O_2$ concentration /mM
MCF7	4.6 [54]
EMT6 spheroids	12.1[55]
MLL	1.3-1.8[56]
AML5	0.2[57]

Table 3-3 – Cumulative $^1O_2$ required to kill various cancerous cell lines when generated by conventional photosensitisers.

It should be noted that cell monolayers have been shown to become hypoxic during and following PDT based treatments, and oxygen depletion is likely to be at its greatest in endosomes that contain densely packed AuNPs.[58] This would lead to lower yields of reactive oxygen species than would be expected in solution based experiments. On the other hand, many conventional PSs target mitochondria or the nucleus of cells, but recent work has reported that PDT against lysosomes is more effective than when targeted at mitochondria.[59] Due to their route of uptake, AuNPs are located exclusively within densely packed intracellular vesicles and have been shown to cause permeabilization and destruction of these vesicles even under non-fatal irradiation.[7] This may amplify the oxidative damage upon irradiation due to accumulation of autophagosomes, autophagic stress and consequently an amplification of the apoptic response.

While the customisation of conventional PSs can allow targeting of specific organelles within the cancerous cell, it must also allow preferential accumulation within the tumour compared to the rest of the body to take advantage of the dual sensitivity that is one of the main advantages of a PDT treatment. However, as the internalisation of AuNPs is limited to endosomes (unless cell penetrating peptides are used), the surface chemistry of the AuNPs can be optimised for active targeting of tumour cells without losing the cytotoxic efficiency that arises from their localisation within the cell.[60] This, combined with the properties of AuNPs such as good photostability, enzymatic stability, customisable surface chemistry and non-toxicity, means that AuNPs can provide significant advantages over conventional PSs.

3.6.6 Reassessment of Use of AuNP@CALNN as Photosensitisers

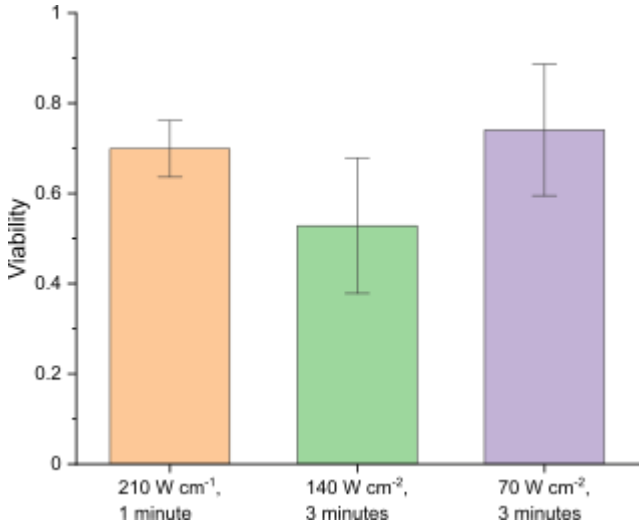

Figure 3.18 – Viabilities of HeLa cells following various irradiations on cells incubated with 14 nm AuNP@CALNN (4 nM, 3 hours), this only includes experiments where the simulated temperature did not reach 50 °C.

As discussed in section 3.2.4, HeLa cells exposed to AuNP@CALNN (4 nM, 3 hours) showed no significant cell killing when exposed to laser irradiation that did not reach the required threshold temperature for photothermal killing. However, upon reassessment of these experiments using the viability method, these experiments showed significantly reduced viability, see figure 3.18 The effects reported here are similar to those reported for AuNP@cit, although these cells contain significantly more AuNP@CALNN (220,000 AuNP@CALNN per cell) than cells incubated with AuNP@cit (42,000 AuNP@cit per cell). However, with most AuNP@CALNN being localised on the exterior of the cell membrane (see figure 3.2), only a small fraction of nanoparticles – 10%, or around 20,000 AuNP@CALNN - are within intracellular vesicles. It should be noted that in addition to the effect from AuNPs within the cell, cell membranes have been targeted for PDT and this has been effective.[61] Thus, significantly more $^1O_2$ is generated in the experiments using AuNP@CALNN, but despite this the efficacy is only slightly higher, this suggests that, as the majority of the AuNPs are bound to the exterior of the cell, the localisation of the AuNP is significant in the cytotoxicity. This provides further proof that $^1O_2$ is responsible due to its short range of activity. In the majority of cases, the viability is never reduced below 0.4, and for those cases where low viability is observed, the temperatures

approach the threshold for photothermal mediated cytotoxicity as seen in figure 3.12.

In experiments where the total light energy used is increased or cells had a high local confluency, the temperature limit is exceeded and cytotoxicity is mediated by heating. This highlights the intrinsic limit of using AuNPs as photodynamic agents, since due to their low quantum yield for SO production nearly all the light energy is converted to heat. If the amount of AuNP@CALNN or the laser irradiation time is increased, the amount of heat generated ensures that any photodynamic effect is overcome by photothermal killing. While the short range of singlet oxygen ensures AuNP localisation is important for photodynamic therapy, heat dissipation means that AuNP localisation is irrelevant for photothermal therapy. This effect limits any application of AuNP@CALNN for photodynamic therapy and is important to consider for other AuNPs.

3.7 Conclusion

AuNPs internalised within HeLa cells can cause cell death upon irradiation with 532 nm light via two pathways. The first is via photothermal heating of the HeLa cells to above 45-50 °C, which can be predicted with temperature simulations and depends only on the total gold content of HeLa cell culture, irrespective of the cellular location. The second alternative route takes place at temperatures below those required for photothermal killing, is localised to individual cells and is dependent on the total dose of light administered and the amount of AuNPs internalised in each individual cell. We suggest that AuNPs generate $^1O_2$ within cells and kill cells via a photodynamic effect. This shows AuNPs are a potential PDT agent, which would provide significant advantages over conventional organic photosensitisers and over the more widely researched application of AuNPs as a PTT agent. In particular, the localised nature of cell killing offers the prospect of selectively killing cancer cells in an environment where both cancerous and non-cancerous cells are present, such as in a tumour bed after surgical removal of a larger tumour, since selective targeting of AuNPs to cancer cells has been shown to be feasible. [60,62]

Additionally, we also present evidence that the variability within this route is due to the variation in AuNP content of individual cells and show that this depends on the cell confluency, leading to more densely packed cells being less affected by the same dose.

3.8 References

(1) Chadwick, S. Photodynamic and Photothermal Human Cancer Cell Killing Using Gold Nanoparticles, PhD Thesis, University of Liverpool, **2015**.

(2) Nativo, P.; Prior, I. a; Brust, M. Uptake and Intracellular Fate of Surface-Modified Gold Nanoparticles. **2008**, *2* (8), 1639–1644. https://doi.org/10.1021/nn800330a.

(3) Maiorano, G. et al. Effects of Cell Culture Media on the Dynamic Formation of Protein−Nanoparticle Complexes and Influence on the Cellular Response. *ACS Nano* **2010**, *4* (12), 7481–7491. https://doi.org/10.1021/nn101557e.

(4) Chithrani, B. D.; Ghazani, A. A.; Chan, W. C. W. Determining the Size and Shape Dependence of Gold Nanoparticle Uptake into Mammalian Cells. *Nano Lett.* **2006**, *6* (4), 662–668. https://doi.org/10.1021/nl052396o.

(5) Behzadi, S. et al. Cellular Uptake of Nanoparticles: Journey inside the Cell. **2017**, *46* (14). https://doi.org/10.1039/c6cs00636a.

(6) Chithrani, B. D.; Chan, W. C. W. Elucidating the Mechanism of Cellular Uptake and Removal of Protein-Coated Gold Nanoparticles of Different Sizes and Shapes. *Nano Lett.* **2007**, *7* (6), 1542–1550. https://doi.org/10.1021/nl070363y.

(7) Krpetić, Ž. et al. Inflicting Controlled Nonthermal Damage to Subcellular Structures by Laser-Activated Gold Nanoparticles. *Nano Lett.* **2010**, *10* (11), 4549–4554. https://doi.org/10.1021/nl103142t.

(8) Hao, X. et al. Caveolae-Mediated Endocytosis of Biocompatible Gold Nanoparticles in Living Hela Cells. *J. Phys. Condens. Matter* **2012**, *24* (16). https://doi.org/10.1088/0953-8984/24/16/164207.

(9) Cho, E. C.; Xie, J.; Wurm, P. A.; Xia, Y. Understanding the Role of Surface Charges in Cellular Adsorption versus Internalization by Selectively Removing Gold Nanoparticles on the Cell Surface with a I 2/KI Etchant. *Nano Lett.* **2009**, *9* (3), 1080–1084. https://doi.org/10.1021/nl803487r.

(10) Li, Z. et al. Small Gold Nanorods Laden Macrophages for Enhanced Tumor Coverage in Photothermal Therapy. *Biomaterials* **2016**, *74*, 144–154. https://doi.org/10.1016/j.biomaterials.2015.09.038.

(11) Jaque, D. et al. Nanoparticles for Photothermal Therapies. *Nanoscale* **2014**, *6* (16), 9494–9530. https://doi.org/10.1039/c4nr00708e.

(12) Liu, Y. et al. A Plasmonic Gold Nanostar Theranostic Probe for in Vivo Tumor Imaging and Photothermal Therapy. *Theranostics* **2015**, *5* (9), 946–960. https://doi.org/10.7150/thno.11974.

(13) MacKey, M. A.; Ali, M. R. K.; Austin, L. A.; Near, R. D.; El-Sayed, M. A. The Most Effective Gold Nanorod Size for Plasmonic Photothermal Therapy: Theory and in Vitro Experiments. *J. Phys. Chem. B* **2014**, *118* (5), 1319–1326.

https://doi.org/10.1021/jp409298f.

(14) Song, J. et al. Ultrasmall Gold Nanorod Vesicles with Enhanced Tumor Accumulation and Fast Excretion from the Body for Cancer Therapy. *Adv. Mater.* **2015**, *27* (33), 4910–4917. https://doi.org/10.1002/adma.201502486.

(15) He, X.; Bhowmick, S.; Bischof, J. C. Thermal Therapy in Urologic Systems: A Comparison of Arrhenius and Thermal Isoeffective Dose Models in Predicting Hyperthermic Injury. *J. Biomech. Eng.* **2009**, *131* (7), 1–12. https://doi.org/10.1115/1.3128671.

(16) Huang, P. et al. Biodegradable Gold Nanovesicles with an Ultrastrong Plasmonic Coupling Effect for Photoacoustic Imaging and Photothermal Therapy. *Angew. Chemie Int. Ed.* **2013**, *52* (52), 13958–13964. https://doi.org/10.1002/anie.201308986.

(17) Yang, W. L. et al. Heat Shock Protein 70 Is Induced in Mouse Human Colon Tumor Xenografts after Sublethal Radiofrequency Ablation. *Ann. Surg. Oncol.* **2004**, *11* (4), 399–406. https://doi.org/10.1245/ASO.2004.08.013.

(18) Hirsch, L. R. et al. Nanoshell-Mediated near-Infrared Thermal Therapy of Tumors under Magnetic Resonance Guidance. *Proc. Natl. Acad. Sci.* **2003**, *100* (23), 13549–13554. https://doi.org/10.1073/pnas.2232479100.

(19) Dickerson, E. B. et al. Gold Nanorod Assisted Near-Infrared Plasmonic Photothermal Therapy (PPTT) of Squamous Cell Carcinoma in Mice. *Cancer Lett.* **2008**, *269* (1), 57–66. https://doi.org/10.1016/j.canlet.2008.04.026.

(20) Loo, C.; Lowery, A.; Halas, N.; West, J.; Drezek, R. Immunotargeted Nanoshells for Integrated Cancer Imaging and Therapy. *Nano Lett.* **2005**, *5* (4), 709–711. https://doi.org/10.1021/nl050127s.

(21) Chen, J. et al. Immuno Gold Nanocages with Tailored Optical Properties for Targeted Photothermal Destruction of Cancer Cells. *Nano Lett.* **2007**, *7* (5), 1318–1322. https://doi.org/10.1021/nl070345g.

(22) Gobin, A. M. et al. Near-Infrared Resonant Nanoshells for Combined Optical Imaging and Photothermal Cancer Therapy. *Nano Lett.* **2007**, *7* (7), 1929–1934. https://doi.org/10.1021/nl070610y.

(23) Pelaz, B. et al. Tailoring the Synthesis and Heating Ability of Gold Nanoprisms for Bioapplications. *Langmuir* **2012**, *28* (24), 8965–8970. https://doi.org/10.1021/la204712u.

(24) Hu, M.; Hartland, G. V. Heat Dissipation for Au Particles in Aqueous Solution: Relaxation Time versus Size. *J. Phys. Chem. B* **2002**, *106* (28), 7029–7033. https://doi.org/10.1021/jp020581CCC:22.00.

(25) Keblinski, P.; Cahill, D. G.; Bodapati, A.; Sullivan, C. R.; Taton, T. A. Limits of Localized Heating by Electromagnetically Excited Nanoparticles. *J. Appl. Phys.* **2006**, *100* (5). https://doi.org/10.1063/1.2335783.

(26) Richardson, H. H.; Carlson, M. T.; Tandler, P. J.; Hernandez, P.; Govorov, A. O.

Experimental and Theoretical Studies of Light-to-Heat Conversion and Collective Heating Effects in Metal Nanoparticle Solutions. *Nano Lett.* **2009**, *9* (3), 1139–1146. https://doi.org/10.1021/nl8036905.

(27) Casals, E.; Pfaller, T.; Duschl, A.; Oostingh, G. J.; Puntes, V. Time Evolution of the Nanoparticle Protein Corona. *ACS Nano* **2010**, *4* (7), 3623–3632. https://doi.org/10.1021/nn901372t.

(28) Piella, J.; Bastús, N. G.; Puntes, V. Size-Dependent Protein-Nanoparticle Interactions in Citrate-Stabilized Gold Nanoparticles: The Emergence of the Protein Corona. *Bioconjug. Chem.* **2017**, *28* (1), 88–97. https://doi.org/10.1021/acs.bioconjchem.6b00575.

(29) Deeley, N. The Protein Corona on Gold Nanoparticles and Its Consequences for Photodynamic Cancer Therapy, MChem Dissertation, University of Liverpool, **2019**.

(30) Davidson, A. M.; Brust, M.; Cooper, D. L.; Volk, M. Sensitive Analysis of Protein Adsorption to Colloidal Gold by Differential Centrifugal Sedimentation. *Anal. Chem.* **2017**, *89* (12), 6807–6814. https://doi.org/10.1021/acs.analchem.7b01229.

(31) Khetan, J.; Shahinuzzaman, M.; Barua, S.; Barua, D. Quantitative Analysis of the Correlation between Cell Size and Cellular Uptake of Particles. *Biophys. J.* **2019**, *116* (2), 347–359. https://doi.org/10.1016/j.bpj.2018.11.3134.

(32) Shahinuzzaman, M.; Barua, D. Dissecting Particle Uptake Heterogeneity in a Cell Population Using Bayesian Analysis. *Biophys. J.* **2020**, *118* (7), 1526–1536. https://doi.org/10.1016/j.bpj.2020.01.043.

(33) Jeynes, J. C. G.; Jeynes, C.; Merchant, M. J.; Kirkby, K. J. Measuring and Modelling Cell-to-Cell Variation in Uptake of Gold Nanoparticles. *Analyst* **2013**, *138* (23), 7070. https://doi.org/10.1039/c3an01406a.

(34) Wang, X. et al. Influence of Cell Size on Cellular Uptake of Gold Nanoparticles. *Biomater. Sci.* **2016**, *4* (6), 970–978. https://doi.org/10.1039/c6bm00171h.

(35) Puliafito, A. et al. Collective and Single Cell Behavior in Epithelial Contact Inhibition. *Proc. Natl. Acad. Sci. U. S. A.* **2012**, *109* (3), 739–744. https://doi.org/10.1073/pnas.1007809109.

(36) Wang, X. et al. Influence of Cell Size on Cellular Uptake of Gold Nanoparticles. *Biomater. Sci.* **2016**, *4* (6), 970–978. https://doi.org/10.1039/c6bm00171h.

(37) Huang, X.; Jain, P. K.; El-Sayed, I. H.; El-Sayed, M. A. Determination of the Minimum Temperature Required for Selective Photothermal Destruction of Cancer Cells with the Use of Immunotargeted Gold Nanoparticles. *Photochem. Photobiol.* **2006**, *82* (2), 412. https://doi.org/10.1562/2005-12-14-RA-754.

(38) AL-Jawad, S. M. H.; Taha, A. A.; Al-Halbosiy, M. M. F.; AL-Barram, L. F. A. Synthesis and Characterization of Small-Sized Gold Nanoparticles Coated by Bovine Serum Albumin (BSA) for Cancer Photothermal Therapy. *Photodiagnosis Photodyn. Ther.* **2018**, *21* (December 2017), 201–210.

https://doi.org/10.1016/j.pdpdt.2017.12.004.

(39) Guerrero-Florez, V. et al. Gold Nanoparticle-Mediated Generation of Reactive Oxygen Species during Plasmonic Photothermal Therapy: A Comparative Study for Different Particle Sizes, Shapes, and Surface Conjugations. *J. Mater. Chem. B* **2020**, *8* (14), 2862–2875. https://doi.org/10.1039/d0tb00240b.

(40) Li, J. L. et al. In Vitro Cancer Cell Imaging and Therapy Using Transferrin-Conjugated Gold Nanoparticles. *Cancer Lett.* **2009**, *274* (2), 319–326. https://doi.org/10.1016/j.canlet.2008.09.024.

(41) Khan, J. A.; Pillai, B.; Das, T. K.; Singh, Y.; Maiti, S. Molecular Effects of Uptake of Gold Nanoparticles in HeLa Cells. *ChemBioChem* **2007**, *8* (11), 1237–1240. https://doi.org/10.1002/cbic.200700165.

(42) Mironava, T.; Hadjiargyrou, M.; Simon, M.; Jurukovski, V.; Rafailovich, M. H. Gold Nanoparticles Cellular Toxicity and Recovery: Effect of Size, Concentration and Exposure Time. *Nanotoxicology* **2010**, *4* (1), 120–137. https://doi.org/10.3109/17435390903471463.

(43) Vankayala, R.; Sagadevan, A.; Vijayaraghavan, P.; Kuo, C. L.; Hwang, K. C. Metal Nanoparticles Sensitize the Formation of Singlet Oxygen. *Angew. Chemie - Int. Ed.* **2011**, *50* (45), 10640–10644. https://doi.org/10.1002/anie.201105236.

(44) Jiang, C. et al. Two-Photon Induced Photoluminescence and Singlet Oxygen Generation from Aggregated Gold Nanoparticles. *ACS Appl. Mater. Interfaces* **2013**, *5* (11), 4972–4977. https://doi.org/10.1021/am4007403.

(45) Zhang, Y.; Qian, J.; Wang, D.; Wang, Y.; He, S. Multifunctional Gold Nanorods with Ultrahigh Stability and Tunability for in Vivo Fluorescence Imaging, SERS Detection, and Photodynamic Therapy. *Angew. Chemie - Int. Ed.* **2013**, *52* (4), 1148–1151. https://doi.org/10.1002/anie.201207909.

(46) Chadwick, S. J.; Salah, D.; Livesey, P. M.; Brust, M.; Volk, M. Singlet Oxygen Generation by Laser Irradiation of Gold Nanoparticles. *J. Phys. Chem. C* **2016**, *120* (19), 10647–10657. https://doi.org/10.1021/acs.jpcc.6b02005.

(47) Lv, J.; Zhang, X.; Li, N.; Wang, B.; He, S. Absorption-Dependent Generation of Singlet Oxygen from Gold Bipyramids Excited under Low Power Density. *RSC Adv.* **2015**, *5* (100), 81897–81904. https://doi.org/10.1039/c5ra15362j.

(48) Zhao, T. et al. Gold Nanorods as Dual Photo-Sensitizing and Imaging Agents for Two-Photon Photodynamic Therapy. *Nanoscale* **2012**, *4* (24), 7712–7719. https://doi.org/10.1039/c2nr32196c.

(49) Gao, L. et al. Plasmon-Mediated Generation of Reactive Oxygen Species from near-Infrared Light Excited Gold Nanocages for Photodynamic Therapy in Vitro. *ACS Nano* **2014**, *8* (7), 7260–7271. https://doi.org/10.1021/nn502325j.

(50) Snijder, B.; Pelkmans, L. Origins of Regulated Cell-to-Cell Variability. *Nat. Publ. Gr.* **2011**, *12* (2), 119–125. https://doi.org/10.1038/nrm3044.

(51) Damm, E. et al. Population Context Determines Cell-to-Cell Variability in

Endocytosis and Virus Infection. **2009**, *461* (September). https://doi.org/10.1038/nature08282.

(52) Imoukhuede, P. I.; Popel, A. S. Quantification and Cell-to-Cell Variation of Vascular Endothelial Growth Factor Receptors. *Exp. Cell Res.* **2011**, *317* (7), 955–965. https://doi.org/10.1016/j.yexcr.2010.12.014.

(53) Entradas, T. Photogeneration of Singlet Oxygen by Gold Nanoparticles, PhD Thesis, University of Liverpool. **2019**.

(54) Anquez, F.; El Yazidi Belkoura, I.; Suret, P.; Randoux, S.; Courtade, E. Cell Death Induced by Direct Laser Activation of Singlet Oxygen at 1270 Nm. *Laser Phys.* **2013**, *23* (2). https://doi.org/10.1088/1054-660X/23/2/025601.

(55) Georgakoudi, I.; Nichols, M. G.; Foster, T. H. The Mechanism of Photofrin Photobleaching and Its Consequences for Photodynamic Dosimetry. *Photochem. Photobiol.* **1997**, *65* (1), 135–144.

(56) Dysart, J. S.; Singh, G.; Patterson, M. S. Calculation of Singlet Oxygen Dose from Photosensitizer Fluorescence and Photobleaching during MTHPC Photodynamic Therapy of MLL Cells. *Photochem. Photobiol.* **2005**, *81* (1), 196–205. https://doi.org/10.1562/2004-07-23-RA-244.

(57) Niedre, M. J.; Secord, A. J.; Patterson, M. S.; Wilson, B. C. In Vitro Tests of the Validity of Singlet Oxygen Luminescence Measurements as a Dose Metric in Photodynamic Therapy In Vitro Tests of the Validity of Singlet Oxygen Luminescence Measurements as a Dose Metric in Photodynamic Therapy. **2003**, 7986–7994.

(58) Weston, M. A.; Patterson, M. S. Measurement of Intracellular Oxygen Concentration During Photodynamic Therapy in Vitro. **2014**, 878–888. https://doi.org/10.1111/php.12256.

(59) Kessel, D.; Reiners, J. J. Promotion of Proapoptotic Signals by Lysosomal Photodamage. *Photochem. Photobiol.* **2015**, *91* (4), 931–936. https://doi.org/10.1111/php.12456.

(60) Lévy, R.; Shaheen, U.; Cesbron, Y.; Sée, V. Gold Nanoparticles Delivery in Mammalian Live Cells: A Critical Review. *Nano Rev.* **2010**, *1* (1), 4889. https://doi.org/10.3402/nano.v1i0.4889.

(61) Buytaert, E.; Dewaele, M.; Agostinis, P. Molecular Effectors of Multiple Cell Death Pathways Initiated by Photodynamic Therapy. *Biochim. Biophys. Acta - Rev. Cancer* **2007**, *1776* (1), 86–107. https://doi.org/10.1016/j.bbcan.2007.07.001.

(62) Chen, J. S. et al. Functionalized Nanoparticles with Targeted Antibody to Enhance Imaging of Breast Cancer in Vivo. *J. Nanobiotechnology* **2020**, *18* (1), 1–9. https://doi.org/10.1186/s12951-020-00695-2.

4 Use of AuNP@cit and AuNP@PAH-RB@PSS as Photosensitisers in HeLa Cells Assessed Using MTT Asssay

4.1 Introduction

While the trypan blue assay used in the previous chapter provides a good measure of treatment efficacy, it is extremely time consuming due to the amount of analysis required and it is not widely used in literature. An MTT assay is a widely used, colorimetric assay that assesses metabolic activity as NADPH-dependent oxidoreductase enzymes reduce 3-(4,5-dimethylthiazol-2-yl)-2,5-diphenyltetrazolium bromide (MTT) to formazin.

In addition to ease of use, a change in protocol was required as initial experiments using trypan blue assays on UM-SCC-1 cells showed that their high motility and growth rate compared to HeLa cells prevented analysis. Typically, the irradiation site became overgrown and previous patterns in the cell distribution could not be located to accurately line up images taken before and after irradiation. This showed that the more mobile UM-SCC-1 cells were moving around in the 24 hours required between irradiation and analysis. To overcome this 6 mm wells were used to grow cells and the entirety of the growth area was irradiated. However, this required expansion of the laser beam and hence lower irradiation intensities were necessitated. This protocol is described in this chapter, including testing on HeLa cells with AuNP@cit for comparison to previous results.

Additionally, for the first time AuNP@PAH-RB@PSS were used against cells and its efficacy is compared against AuNP@cit.

4.2 Experimental

4.2.1 Materials and Equipment

Dulbecco's Modified Eagle Medium (DMEM), heat inactivated fetal bovine serum, non-essential amino acids, Penicillin-Streptomycin, MTT (3-(4,5-Dimethylthiazol-2-yl)-2,5-Diphenyltetrazolium Bromide), DMSO and Dulbecco's phosphate buffered saline (Mg^{2+}, Ca^{2+}, glucose, pyruvate) (DPBS) (pH 7.4) were purchased from

ThermoFisher. Corning cell culture plates and flasks were purchased from Fisher Scientific.

MTT assays were performed on a Molecular Devices F3 Filtermax plate reader.

4.2.2 Irradiation Setup

Four wells were seeded with 4000 or 8000 HeLa cells for 4 or 3 day experiments, respectively, in 96-well plates (well diameter of 6 mm) in 100 µL DMEM (in all cases supplemented with 10 % fetal bovine serum (FBS), 1 % penicillin-streptomycin (P/S) and 1 % non-essential amino acids (NEAA)) and left overnight in an incubator (5% CO_2). AuNPs were mixed with DMEM (1:1, DMEM:AuNP/MQ-H_2O) and the DMEM in the wells was replaced in all wells with the AuNP mixture or DMEM and left for either 3 or 24 hours (incubation time, final AuNP concentration and AuNP type will be stated for each experiment). Following the incubation, cells were washed three times with 100 µL DPBS (Mg^{2+}, Ca^{2+}, glucose, pyruvate) and then the wells were filled with 300 µL DPBS. One of the four wells was irradiated with a cw 532 nm laser with a $1/e^2$ beam width of 1.9 mm which had been expanded using a -100 mm lens to a beam diameter of 6 mm, which passed through a 6 mm aperture directly below the well at different powers. In order to prevent scattered light affecting the control wells, they were covered during irradiation. A diagram of the laser set up can be seen in figure 4.1. Following irradiation, the DPBS was replaced with 100 µL DMEM and the well plate was placed back in the incubator for 20 hours.

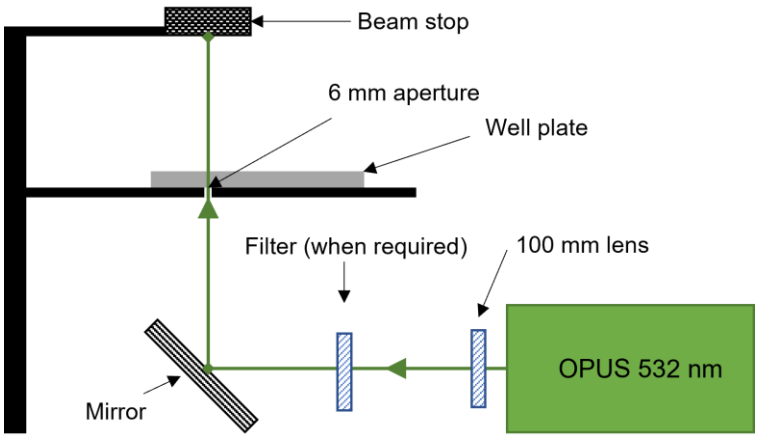

Figure 4.1 – Laser set up for the irradiation of well plates (side view).

In selected experiments the temperature of the DPBS in the irradiated well was measured using a thermocouple immediately after irradiation.

4.2.3 Incubation of Cells with no Irradiation

12 wells were seeded with 4000 (24 hour incubations) or 8000 (3 hour incubations) HeLa cells in a 96 well plate in 100 µL DMEM and left overnight in an incubator. AuNP solutions prepared as above were then added to 6 wells and 1:1 DMEM:MQ-H_2O was added to 6 wells. Following incubation with AuNPs or 1:1 MQ-H_2O, the cells were washed as above with DPBS, 100 µL DMEM was added and placed in the incubator for a further 20 hours.

4.2.4 Determining Viability

The DMEM was replaced with 100 µL MTT solution (10% 5 mg/mL MTT, 90% DMEM), and after 4 hours the MTT solution was removed and 100 µL of dimethyl sulfoxide (DMSO) was added. This was left for 20 minutes to solubilise in the incubator before the absorbance was assessed at 595 nm and 620 nm for each well using a plate reader. Following the standard protocol for the MTT assay, the viability was calculated by dividing the absorbance difference (595-620) of the irradiated wells by the absorbance difference of the control wells, which can be seen in equation 4-1.

$$Viability = \frac{Absorbance\ of\ irradiated\ cell_{595\ nm} - Absorbance\ of\ irradiated\ cell_{620\ nm}}{Average\ (Absorbance\ of\ control\ cell_{595\ nm} - Absorbance\ of\ control\ cell_{620\ nm})}$$

Equation 4-1 – Determination of viability of irradiated cell using MTT assay

4.2.5 Determining Cellular Uptake of AuNP@PAH-RB@PSS

HeLa cells were seeded in 100 mm diameter dishes and left overnight to attach to the surface of the dish. Subsequently, the media was replaced with 10 mL of 1:1 media to AuNP solution at a final AuNP concentration of 0.586 nM, 0.293 nM and 0.147 nM, respectively. After 3 hours, the solution was removed and the cells were washed 3 times with fresh DPBS. The cells were then detached using 1 mL trypsin and resuspended in 9 mL media. At this stage, 0.024 mL was removed and used for cell counting in a hemacytometer. After counting, the cell suspension was centrifuged (1000 RCF, 10 minutes) and the supernatant was removed. 0.5 mL aqua

regia was added to the pellet and left for 3 days. 4.5 mL MQ-H_2O was added to the solution and the concentration of gold was then determined using ICP-OES.

4.2.6 Effect of Beam Inhomogeneity

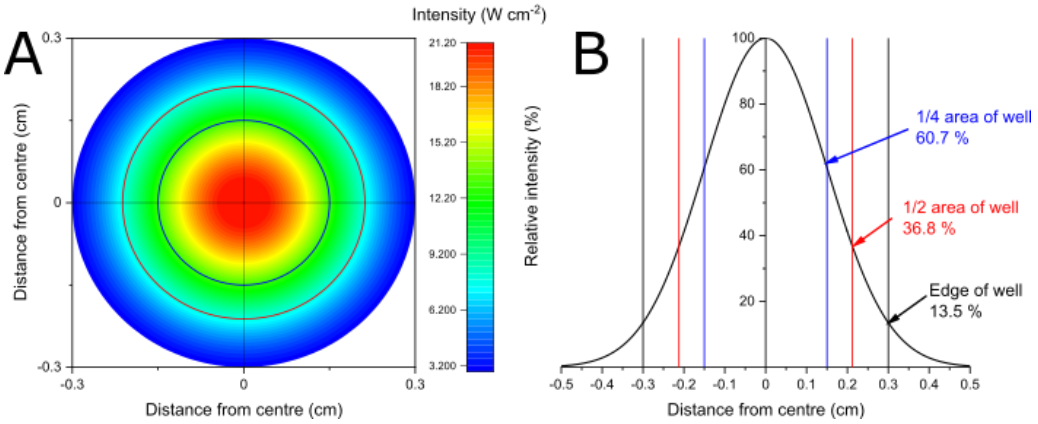

Figure 4.2 – The intensity profile of the laser beam used in well irradiations. A) The intensity profile of a 3 W irradiation. The area of the plot represents the size of a well, with the red line representing half of the area of the well and the blue line representing a quarter. B) The relative intensity of the beam compared to the intensity of the beam in the centre of irradiation.

In these experiments, the laser beam was expanded from a diameter of 1.9 mm to 6 mm in order to cover the entirety of the irradiated well with light. In the previous dish experiments only the inner 0.5 mm was considered, as this is where the light intensity only varies by 12%, however the variation of light intensity in the 6 mm well is almost 90%. This can be seen in figure 4.2 which shows the beam profile which is assumed to be Gaussian. Assuming that cells are evenly distributed throughout the well, ¼ of the cells will experience 61-100% of the maximum intensity and ¼ will experience 37-61% of the intensity in the centre of the well, the remaining ½ of cells will receive less than 37% of the maximum intensity.

This means that the inhomogeneity of the beam will play a significant effect upon the killing observed, as unlike in chapter 3, where cells that receive less than 87% of the maximum intensity are discounted, the MTT assay considers the whole population. It is therefore important to consider what fraction of cells can be affected by irradiation, this can be calculated in equation 4-2.

$$Fraction\ of\ cells\ affected = \frac{d^2}{2w^2} ln\left(\frac{I_o}{T}\right)$$

Equation 4-2 Fraction of well area where intensity exceeds threshold intensity T when maximum intensity is I_0

In equation 4-2; d, w, I_o, T are the $1/e^2$ beam diameter, well diameter, laser intensity at the centre of the beam and the threshold intensity for killing, respectively. The threshold intensity for killing corresponds to the intensity of light where the intensity is still sufficient to kill an (average) cell. This now ignores the cell size effects which have been discussed in chapter 3.

4.3 Uptake of AuNPs@PAH-RB@PSS by HeLa cells

HeLa cells exposed to 13.8 nm core size AuNP@PAH-RB@PSS, as reported in 1.3.4, for 3 hours at a concentration; 0.586 nM, 0.293 nM and 0.147 nM and analysed using ICP-OES resulted in a mean AuNP uptake of; 5200±200, 3300±500 and 1700±300 AuNPs per cell, respectively.

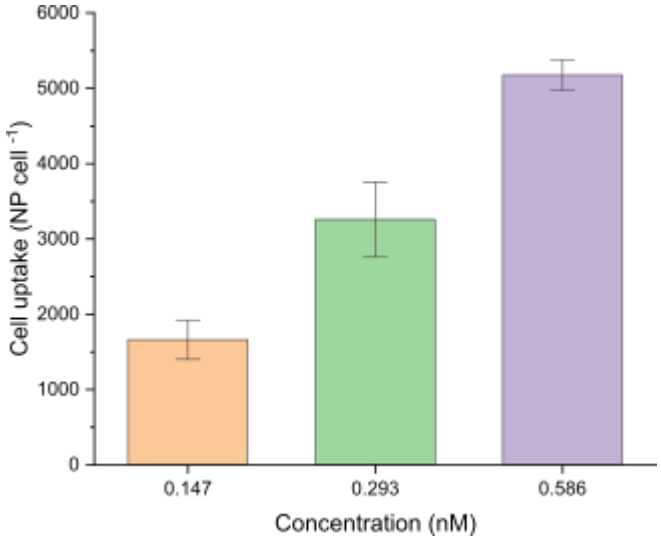

Figure 4.3 – Cellular uptake of AuNP@PAH-RB@PSS by HeLa cells after 3 hour incubation with AuNP@PAH-RB@PSS at concentration; 0.147 (orange), 0.293 (green) and 0.586 nM (purple). The bars represent the mean of several experiments and the error bars represent the standard deviation.

The uptake of AuNP@PAH-RB@PSS increases as the incubation concentration is increased from 0.147 nM to 0.586 nM, this is consistent with literature across a range of AuNP concentrations.[1,2] However, when concentration is scaled for, the uptake of AuNP@PAH-RB@PSS is less than that reported for AuNP@cit in 3.2.1. The difference

in surface chemistry of the two AuNPs may provide an explanation as uptake of NPs depends heavily on the surface chemistry of the AuNP.[3] AuNP@cit interacts strongly with serum proteins which include proteins such as BSA that can displace citrate to form sulphur-gold bonds.[4] For AuNP@PAH-RB@PSS due to the double capping layer from polyelectrolytes it is unlikely that this direct gold-protein interaction is possible. The PSS layer will interact with different serum proteins, resulting in a changed protein corona and consequently interact with the cell membrane in a different way.

Polyelectrolyte encapsulated NPs have been shown to be taken into cells through endocytosis resulting in internalisation within endosomes and lysosomes.[5–7] While there are no reports about the internalisation of AuNPs with an outer coating of PSS, it is likely that they are internalised within endosomes in a similar way to AuNP@cit, which will allow a direct comparison between the efficacy of AuNP@PAH-RB@PSS and AuNP@cit.

4.4 Control Experiments

4.4.1 Effect of Incubation of HeLa cells with AuNPs

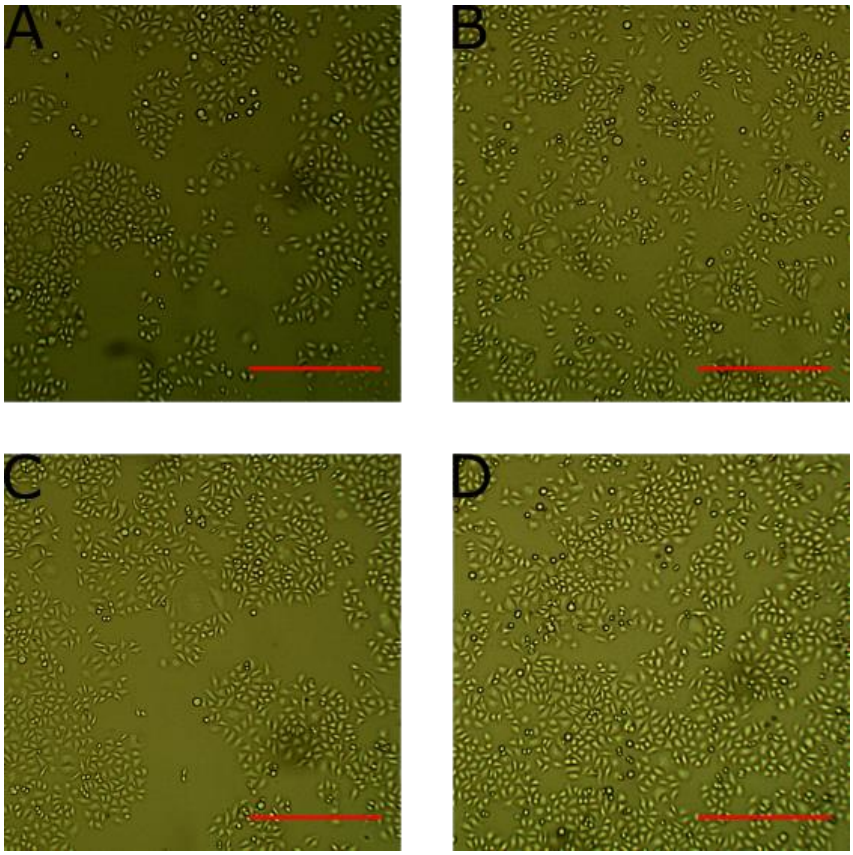

Figure 4.4 – HeLa cells 24 hours after incubation with; A) AuNP@cit (2 nM , 3 hours), B) AuNP@PAH-RB@PSS (0.586 nM, 3 hours), C) AuNP@PAH-RB@PSS (0.293 nM, 3 hours), D) AuNP@PAH-RB@PSS (0.147 nM, 3 hours). Scale bar in all images represents 0.5 mm.

The viability of HeLa cells containing 42,000 13.8 nm AuNP@cit (incubation at 2 nM, 3 hours) and 320,000 AuNP@cit (2 nM, 24 hours) was assessed with MTT and found to be 0.66±0.10 and 0.57±0.08, respectively. This is similar to the reduction in growth rate from 2.04 ± 0.08 to 1.68 ± 0.19 obtained using the trypan blue assay for AuNP@cit (incubated with 2 nM, 3 hours). HeLa cells incubated with AuNP@PAH-RB@PSS containing 5200 (incubated with 0.587 nM, 3 hours), 3300 (incubated with 0.293 nM, 3 hours) and 1700 (incubated with 0.147 nM, 3 hours) were found to have a viability of 0.87±0.13, 0.83±0.28, 0.80±0.28, respectively. When viability was assessed immediately after incubation (incubated with 0.293 nM, 3 hours), viability was found to be 0.96±0.20. In images of representative wells, some deformed cells can be seen in figure 4.4 for AuNP@cit (2 nM, 3 hours), few deformed cells can be seen in incubations with AuNP@PAH-RB@PSS.

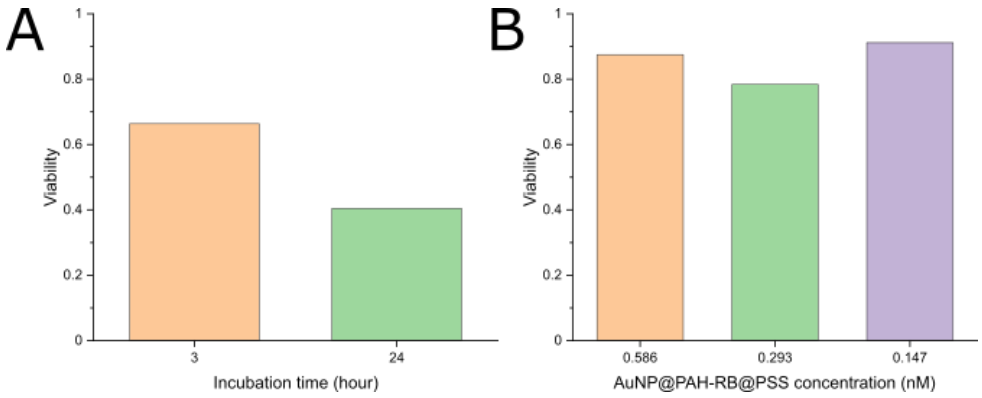

Figure 4.5 – Viability of HeLa cells 24 hours after incubation with; A) 2 nM AuNP@cit, B) AuNP@PAH-RB@PSS 3 hours.

Due to the lower concentration of AuNP@PAH-RB@PSS required for irradiation based cell killing, the toxicity of AuNP@PAH-RB@PSS in the absence of light irradiation is significantly lower than that of AuNP@cit, figure 4.5. The effect on viability is less than that reported for the standard 2 nm, 3 hour AuNP@cit required for cell killing in the dish experiments in chapter 3, and significantly less than the effect by 2 nm, 24 hour AuNP@cit needed to observe cell killing in well experiments. This reduction is expected as literature shows that AuNP toxicity is directly related to

the amount of AuNPs in the cell.[8] It has previously been reported that HeLa cells incubated with 0.24 nM PSS coated gold nanorods for 6 hours resulted in AuNP content per cell of ~2000, with a viability captured immediately after incubation of 95%.[9] Considering that AuNRs are typically taken up less by cells, these results are in good accordance with the results reported here, HeLa cells treated with 0.293 nM AuNP@PAH-RB@PSS for 3 hours resulting in 3300 AuNPs per cell and a viability measured immediately after incubation of 96%. Human neuroblastoma cells (SH-SY5y) treated with 0.2 nM, 18 nm AuNP@cit, AuNP@cit@PAA and AuNP@..@PAH for 24 hours and analysed using a formazin based assay all showed showed viabilities of 95%, while AuNP@CTAB showed a viability of 25%, which shows that the influence of surface coating may play a role in toxicity.[10] The toxicity of AuNPs is related to AuNP uptake, which itself relies upon incubation time, concentration, cell type and surface chemistry of the nanoparticle, which makes directly comparing our results to others difficult.[11,12] Despite this, the viability results reported here are not in disagreement with literature and AuNP@PAH-RB@PSS results in significantly less reduction in cell viability when compared to AuNP@cit.

4.4.2 Irradiation of HeLa cells Containing no AuNPs

The effect of irradiation on HeLa cell viability in wells was determined by exposing cells to irradiation powers and times of 3 W, 12 minutes; 3 W, 6 minutes; 2 W, 6 minutes and 1 W, 6 minutes, resulting in viabilities of 0.58±0.08, 0.99±0.18, 0.96±0.09 and 1.09±0.12, respectively. For irradiation times under 6 minutes no reduction in viability was observed; however, for 3 W, 12 minute irradiations, there was a significant effect upon viability. This is confirmed by optical microscopy shown in figure 4.6B, there is a significant amount of deformed cells throughout the well indicating widespread cell death upon irradiation at 3 W for 12 minutes. While there are some deformed cells in 3 W 6 minute irradiations (figure 4.6A), the level of this is consistent with cells exposed to no irradiation (figure 4.6C). This suggests that the mechanical forces of washing must be considered, as cells that weren't washed didn't show any cell deformation. Due to these visual observations, both treated and untreated cells were always subjected to the same washing procedures.

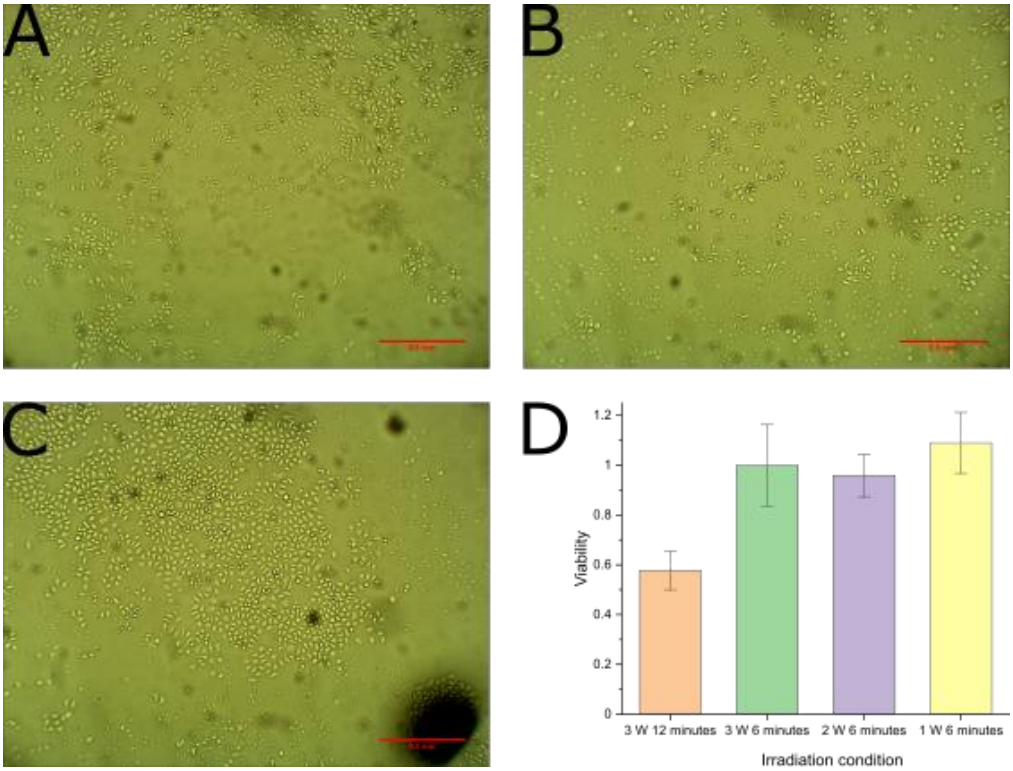

Figure 4.6 - HeLa cells 24 hours after washing and irradiation with; A) 3 W 6 minutes, B) 3 W 12 minutes C) no irradiation. Scale bar in all images represents 0.5 mm. D) Viability of cells irradiated with various conditions, determined using MTT. The bars represent the mean of several repeats and the error bars show the standard deviation.

4.5Irradiation of HeLa cells Containing AuNP@cit

4.5.1 Cell Killing Using AuNP@cit

HeLa cells containing 42,000 (incubation at 2 nM, 3 hours) and 320,000 (2 nM, 3 hours) AuNP@cit were irradiated with 3 W light for 6 minutes. No killing effect was observed for cells containing 42,000 AuNPs as cells had a viability of 1.06±0.06; however, cells containing 320,000 AuNP@Cit resulted in a reduced viability of 0.75±0.07. Longer irradiation times were not tried due to the effect on viability observed with no AuNPs present.

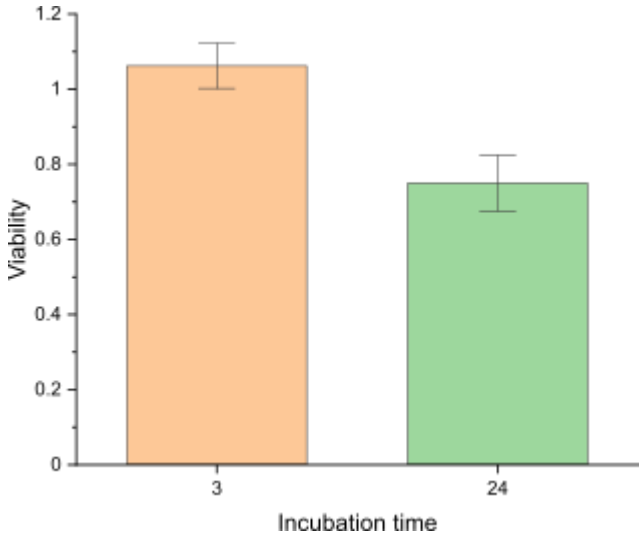

Figure 4.7 – Effect of 3 W irradiation for 6 minutes on HeLa cells following incubation with 2 nM AuNP@cit for 3 (orange) or 24 (green) hours. The bars represent the mean of several experiments and the error bars represent the standard deviation.

4.5.2 Temperature increase in HeLa cells containing AuNP@cit

Due to the differences in the amount of solvent present in a well (300 µL) versus the amount present in the dish experiments discussed in chapter 3 (2000 µL), it is important to rule out photothermal effects from these new well experiments as the solvent has less ability to dissipate the heat away from the irradiated section of cells In order to investigate the potential heating in the well experiments, dynamic simulations to estimate the laser induced temperature rise were performed by M. Volk, using the same method described in section 3.2.3.

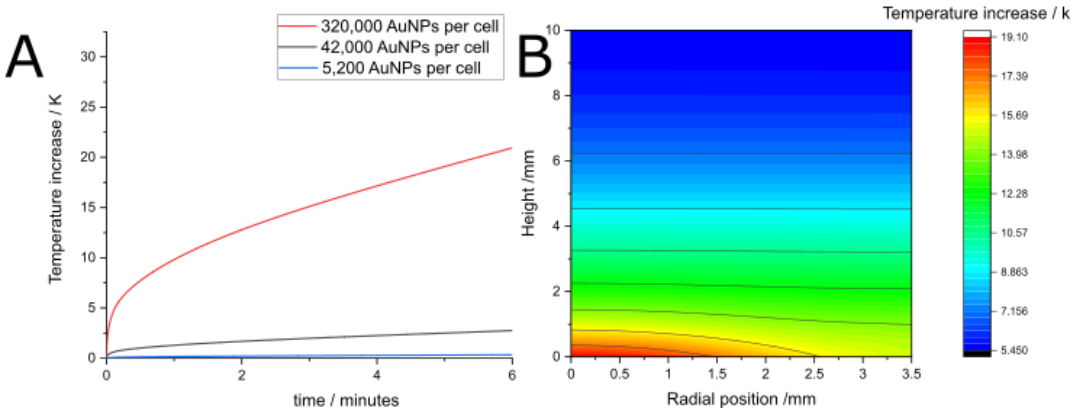

Figure 4.8 – A) Maximum temperature rise after irradiation of HeLa cells containing 320,000 (red), 42,000 (grey) and 5,200 (blue) AuNPs per cell with 3 W for 6 minutes. B) Spatial temperature rise in the buffer layer above background temperature in HeLa cells containing 320,000 AuNPs after irradiation with 3 W for 6 minutes. The colour scale give the temperature increase above the background temperature.

The simulations show an increase of only ~2.5 degrees in the solvent immediately above the cells when cells contain 42,000 AuNP@cit (incubated with 2 nM, 3 hours) and are irradiated at 3 W for 6 minutes, figure 4.8A. However, there is significantly more heating in cells containing 320,000 AuNP@cit (incubated with 2 nM, 24 hours), with an increase over room temperature of ~20 °C; this would lead to a temperature of 39 °C, figure 5.8B, which is still acceptable for good viability.

Temperature increases measured using thermocouples with the highest number of AuNP@cit per cell (320,000) indicate that in a 3 W, 6 minute irradiation the temperature measured in the solvent surrounding the cells was only 25.5 °C, this agrees with the simulations above as this temperature increase was measured in the middle of the well, figure 4.8B. While this suggests that the temperature has not increased to the threshold of 45 °C, the exact temperature in the cell layer may have increased further so heat based killing cannot be explicitly ruled out.

4.5.3 PDT Effect Using AuNP@cit

As discussed in chapter 3, the generation of singlet oxygen by AuNP@cit is proportional to the total light dose and therefore so is any cytotoxic effect shown by the AuNP@cit upon irradiation. As the intensity of light at the maximum laser output of 3 W has dropped to 21.2 W cm^{-2} from 210 W cm^{-2} due to the expansion of the

beam from 1.9 mm to 6 mm, each cell sees a much lower dose of light in the well experiments compared to the dish experiments of chapter 3. When HeLa cells containing 42,000 AuNP@cit were previously irradiated with the small laser beam at 3 W for 3 minutes (Average intensity in the central area: 210 W cm^{-2}), significant cell killing was observed. However, when HeLa cells containing the same number of AuNP@cit were irradiated with the larger laser beam at 3 W for 6 minutes no killing was observed with an MTT assay.

As the total light dose per cell in the centre of the beam has dropped by approximately 90% by expanding the beam, the total singlet oxygen dose received by the cell becomes insufficient to damage the cells even for an irradiation time of 6 minutes. This is in agreement with the results reported in chapter 3, since the light dose in the beam centre for 3W, 6 min of the larger beam corresponds to 0.6 W for 3 minutes with the 1.9 mm beam. Even at a higher dose of 1 W for 3 min (or 3 W for 1 min), no significant reduction of viability (compared to irradiation in the absence of NPs) was observed, see figure 3.17. As the toxicity of longer light doses in cultured cells even in the absence of AuNPs becomes significant in irradiations above 6 minutes (section 4.4.2), there is no further way to increase the cytotoxic dose of singlet oxygen while using the expanded beam.

A potential photodynamic effect was observed in HeLa cells containing 320,000 AuNP@cit after irradiation with 3 W 6 minutes (maximum intensity: 21.2 W cm^{-2}); here, the increased number of AuNPs per cell offsets the light intensity induced reduction in singlet oxygen generation per AuNP. As discussed in section 4.2.6, the beam inhomogeneity means that not all the well sees a sufficient light intensity to damage the cells and the effect of the beam profile is a necessary consideration in these experiments, unlike in chapter 3 where only the beam centre was considered. The observed viability of 0.75, yields a threshold of ~13 W cm^{-2} for cells containing 320,000 AuNP@cit, from equation 4-2, which assumes that killing occurs when I>T. This is a simplified analysis which ignores the distribution of cell uptake discussed in chapter 3, but can be regarded as an estimate of the average threshold.

As the amount of $^1O_2$ produced by AuNP@cit is proportional to the amount of light absorbed, the increased AuNP@cit content per cell means that more light is

absorbed per cell. Using the threshold intensity obtained above (13 W cm^{-2}) and the number of AuNP@cit per cell the amount of light absorbed per cell is equivalent to a 2.8 W, 3 minute irradiation of HeLa cells containing 42,000 AuNP@cit with the 1.9 mm diameter beam. Indeed, a wide range of viabilities was observed, figure 3.14, which suggests that this treatment is at the threshold of cell killing. The role of heating in these well experiments cannot be ruled out, as temperature simulations for these conditions suggest that the maximum temperature reached is approaching the threshold region. However, the results presented here are consistent with the data presented in chapter 3 which suggests that despite the increase in heating the reduction in viability is mediated by $^1O_2$.

As the viability of cells incubated with AuNP@cit (2 nm, 24 hours, no irradiation) is already significantly reduced to 0.57±0.08, it would be unfeasible to increase the AuNP@cit incubation time as the reduced viability would begin to offset any extra light induced killing, and heating would increase, thus the photothermal mechanism would dominate. Furthermore, increasing the incubation time may not significantly increase the AuNP content per cell, as literature suggests that AuNP uptake reaches a steady state as endocytosis and exocytosis reach equilibrium and would start to see large variations between freshly divided and undivided cells.[1,13,14] The same is true of increasing AuNP@cit concentration over a 24 hour time frame as it was found that higher concentrations of AuNP@cit aggregated on exposure to media and cells.

The failure to observe significant killing at low light intensities will present significant obstacles for the use of AuNP@cit, as higher intensity laser light will damage both healthy and cancerous cells due to thermal heating even with no AuNPs present. At tolerable intensities of light, PDT mediated by AuNP@cit suffers from an intrinsic issue in that the majority of light absorbed is converted to heat and due to the extremely low quantum yield of AuNP@cit a significant amount of light energy is needed to be absorbed to generate a toxic dose of singlet oxygen.

4.5.4 Modelling of Cell Killing Using AuNP@cit

As discussed in chapter 3, the uptake of AuNPs by cells is heterogeneous, partly due to the distribution of surface area. While it is not possible to assess the surface area

of cells when using the MTT protocol in wells, it is possible to model uptake heterogeneity and beam inhomogeneity in parallel. This was done in Mathcad (full details can be found in appendix 1), and various parameters can be changed to estimate the viability in a well. The calculation requires the molar extinction coefficient of the AuNP@cit (2.5 x 10^8 M^{-1} cm^{-1}), the $^1O_2$ quantum yield (1.7 x 10^{-7}), the mean uptake of AuNP@cit (320,000), the width of the (log-normal) distribution of AuNP uptake (0.72 – taken from literature)[15], irradiation conditions (3 W, 6 minutes), diameter of the well (6 mm), $1/e^2$ diameter of the laser (6 mm).To achieve a viability of 0.75 (experimental value 0.75±0.07), the required $^1O_2$ dose per cell needs to be ~5 x 10^8 $^1O_2$ molecules, which is only slightly lower than that reported in chapter 3. It should be noted this is an estimate, and the constants are estimates due to the unknown behaviour of quantum yield and absorbance in aggregated AuNP@cit. The more refined modelling also supports the fact that results obtained in chapter 3 and here are in good agreement.

4.6 Irradiation of Cells Containing AuNP@PAH-RB@PSS

4.6.1 Temperature increase in HeLa cells containing AuNP@PAH-RB@PSS

The temperature reached immediately after a 3 W, 6 minute irradiation, measured using a thermocouple, using the highest number of AuNP@PAH-RB@PSS (5200 AuNP $cell^{-1}$), 23.4 °C, which is consistent with the simulations shown in figure 4.8A. This indicates that the heat generated by the AuNPs is not sufficient to damage the cells – as discussed in chapter 3, the temperature required to kill cells is 45 °C. This temperature measured is approximately the same as the ambient temperature of the air, so any heating effect can be discounted. As essentially all the absorption at 532 nm of a AuNP@PAH-RB@PSS is provided by the LSPR band of the AuNP, another piece of evidence that heating is not responsible for any killing observed here is that HeLa cells containing 42,000 AuNP@cit per cell showed no killing effect with a laser irradiation of 3 W for 6 minutes. As each AuNP@cit would absorb the same amount of light as an AuNP@PAH-RB@PSS and there are 42,000 AuNP@cit vs 5200 AuNP@PAH-RB@PSS, the total amount of heat generated by cellular AuNP@PAH-RB@PSS will be much smaller.

Temperature rises were only measured for the highest powers and nanoparticle concentrations used as heat generated is proportional to the number of nanoparticles and the laser power, lower doses will therefore have much smaller amounts of heat, so heating can be discounted.

4.6.2 Cell Killing Using AuNP@PAH-RB@PSS (0.293 nM, 3 hours), 3 W irradiation for 6 minutes

HeLa cells containing 3300 AuNP@PAH-RB@PSS (incubation at 0.293 nM, 3 hours) per cell were irradiated with 3 W for 6 minutes resulting in a viability of 0.54±0.14 when assessed 20 hours after irradiation. This extensive reduction in viability is confirmed by optical microscopy, an example of which can be seen in figure 4.9. There are large amounts of deformed cells dispersed throughout the well, whereas unirradiated wells show few damaged cells.

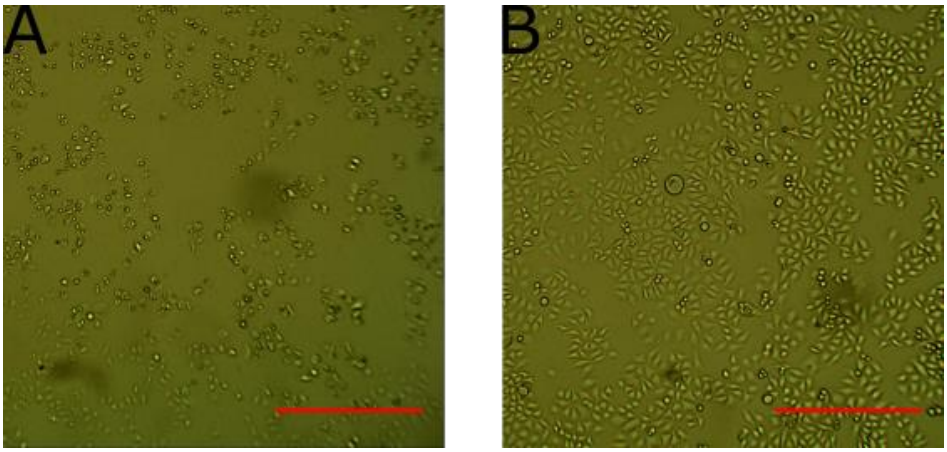

Figure 4.9 –Sections of wells containing HeLa cells 24 hours after incubation with 0.293 nM AuNP@PAH-RB@PSS for 3 hours. A) irradiated for 6 minutes with 3 W B) no irradiation. Scale bar in all images represents 0.5 mm.

4.6.3 Varying Light Dose and the Effect of Rose Bengal Bleaching

HeLa cells containing 3300 AuNP@PAH-RB@PSS (incubation at 0.293 nM, 3 hours) per cell were irradiated for 6 minutes with 2 W, 1 W, 500 mW and 50 mW, which resulted in viabilities of 0.53±0.14, 0.64±0.17, 0.71±0.20 and 0.87±0.05, respectively. Images of typical cell cultures after 50 mW irradiation are shown in figure 4.10 which clearly show distorted and normal cell morphologies interspersed throughout the

well, this can be compared to cell cultures after 3 W irradiation in figure 4.9 where there are more distorted morphologies.

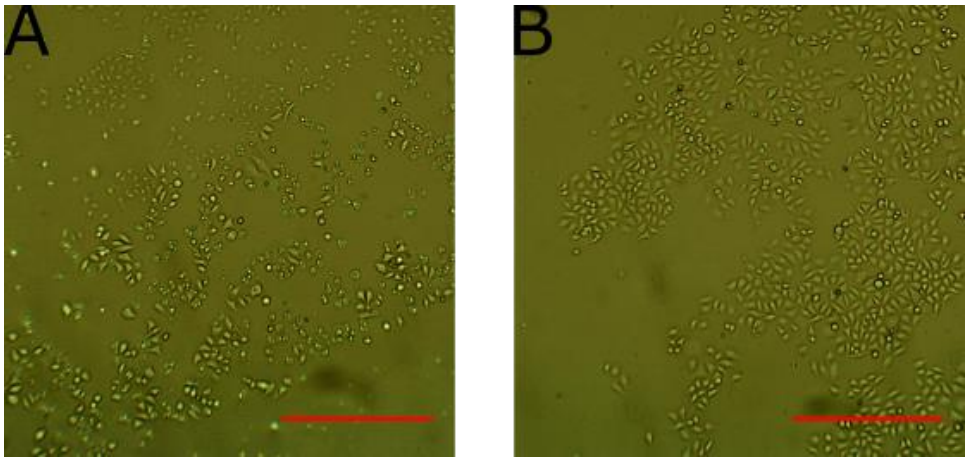

Figure 4.10 – Sections of wells containing HeLa cells 24 hours after incubation with 0.293 nM AuNP@PAH-RB@PSS for 3 hours. A) irradiated for 6 minutes with 50 mW B) no irradiation. Scale bar in all images represents 0.5 mm.

In contrast to the effect on HeLa cells of AuNP@cit, where killing is proportional to the amount of light absorbed by the AuNP, AuNP@PAH-RB@PSS shows a distinctive saturation of killing. For HeLa cells containing 3300 AuNPs on average, there is no significant difference between 6 minute irradiations at 3, 2, 1 and 0.5 W. However, when a much lower power of 50 mW is used, there is still a small effect upon viability, although the intensity of light was reduced by a factor of 60, these results can be seen in figure 4.11.

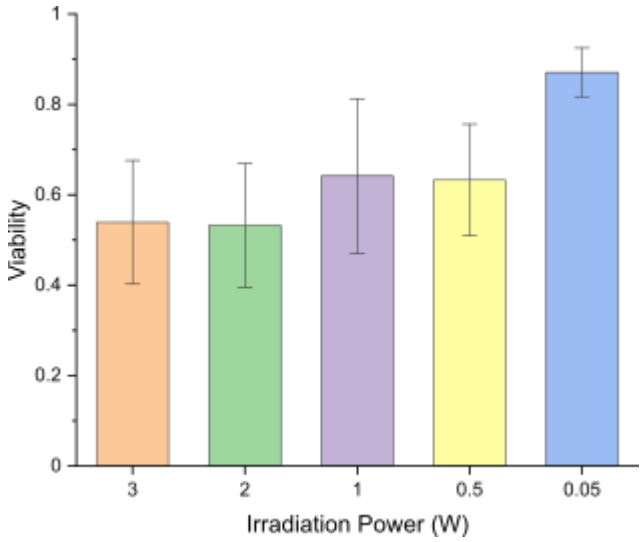

Figure 4.11 – Effect of 6 minute irradiation on HeLa cells incubated with 0.287 nM AuNP@PAH-RB@PSS for 3 hours. Irradiation power; 3 (orange), 2 (green), 1 (purple), 0.5 (yellow) and 0.05 W (blue). The bars represent the mean of several experiments and the error bars represent the standard deviation.

Clearly, the cell killing effect is not directly proportional to the amount of light incident on the well in experiments using AuNP@PAH-RB@PSS, as we would expect there to be no effect in 50 mW irradiations compared to 3 W irradiations as 60 times less singlet oxygen would be produced. However, in contrast to AuNP@cit the generation of singlet oxygen is mediated by Rose Bengal which as an organic dye can photobleach unlike the gold core which is photostable. We can assume that the amount of $^1O_2$ generated per AuNP@PAH-RB@PSS must saturate at higher powers as the Rose Bengal photobleaches. In a 3 W 6 minute experiment each Rose Bengal would absorb 1.8×10^6 photons which is more than enough absorption cycles for the molecule to bleach and hence stop generating singlet oxygen. Even when reducing power, most Rose Bengal molecules still bleach before the end of the irradiation, albeit at a later point. Thus, the amount of $^1O_2$ generated is only determined by the number of absorption cycles before the photobleach, hence generating the same killing effect. Only below a certain power level (for the conditions used here somewhere below 500 mW) will bleaching become less prominent, and many RB remain active until the end of irradiation, so that the amount of $^1O_2$ generated now depends on power, hence the reduced killing at 50mW. For AuNP@PAH-RB@PSS there is a maximum amount of singlet oxygen that can be generated at high powers before all the Rose Bengal is bleached.

While the amount of $^1O_2$ that can be generated per AuNP@PAH-RB@PSS is constant, the amount generated within each cell is not, due to the heterogeneity of AuNP uptake by cells. As the viability saturates to 0.55 for these incubation conditions (3 hr, 0.293 nM), we can assume that the killing effect becomes limited by the amount of AuNP@PAH-RB@PSS that each cell contains. In these conditions, this would correspond to only 45% of the cells containing enough AuNPs per cell to generate the required cytotoxic dose of singlet oxygen before complete bleaching of all Rose Bengal molecules. Even with this correction, the values obtained using equation 4-1 are inconsistent with the results obtained experimentally due to the saturation of $^1O_2$ production by AuNP@PAH-RB@PSS, this means that in these conditions cell death is primarily limited by AuNP@PAH-RB@PSS uptake rather than the light dose.

4.6.4 Varying AuNP@PAH-RB@PSS Concentration

HeLa cells containing 5200 AuNP@PAH-RB@PSS (incubation at 0.586 nM, 3 hours) per cell were irradiated for 6 minutes with 1 W, 0.25 W and 0.05 W, which resulted in viabilities of 0.09±0.01, 0.11±0.06 and 0.35±0.09, respectively. A further increase in power was not used as the absorbances recorded by the plate reader were at the background threshold, indicating that no cells were left alive. A representative section of a well irradiated with 50 mW for 6 minutes can be seen in figure 4.12A, with nearly all cells visible showing distorted morphologies.

HeLa cells containing 1700 AuNP@PAH-RB@PSS (incubation at 0.147 nM, 3 hours) per cell were irradiated for 6 minutes with 3 W, 2 W, 1 W, 0.5 W and 0.05 W resulted in viabilities of 0.98±0.15, 0.99±0.17, 1.04±0.25, 1.18±0.14 and 1.08±0.14, respectively. Lower powers were not assessed as there was no killing at higher powers. A representative section of a well irradiated with 50 mW for 6 minutes can be seen in figure 4.12B with nearly all cells showing normal morphologies.

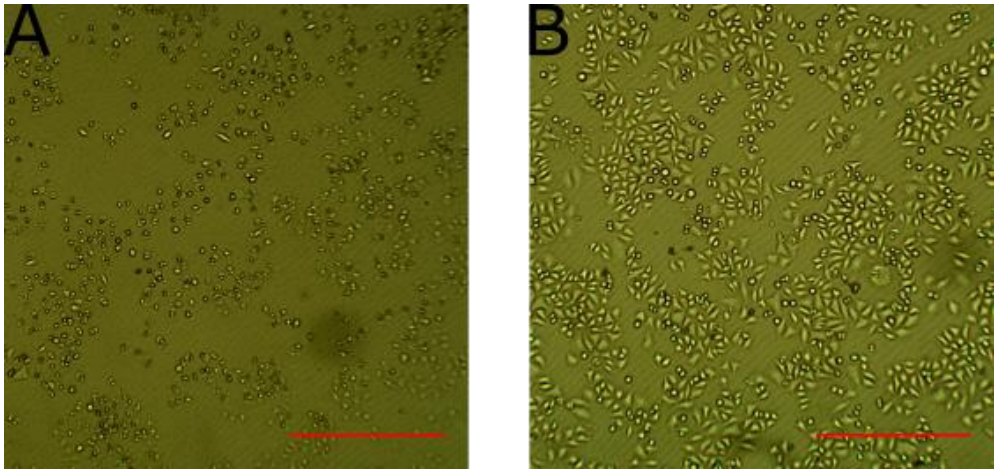

Figure 4.12 – Sections of wells containing HeLa cells 24 hours after irradiation with 50 mW for 6 minutes following a 3 hour incubation with AuNP@PAH-RB@PSS; A) 0.586 nM, B) 0.147 nM. Scale bar in all images represents 0.5 mm.

Increasing the number of AuNPs per cell to 5200 results in a significantly larger effect upon viability compared to cells containing 3300 AuNPs per cell, see figure 4.13. As discussed earlier, the maximum amount of singlet oxygen generated in these cells is limited by how many AuNPs the cell contains. At lower concentrations the bleaching of Rose Bengal that takes place at higher powers limits cell killing, however for cells containing more AuNPs the limit of $^1O_2$ production is beyond the killing threshold. This can be seen in experiments with HeLa cells containing 5200 AuNP@PAH-RB@PSS where the killing is saturated at 90% for powers as low as 250 mW, rather than at 45% for powers of 3000 mW in experiments using HeLa cells containing 3300 AuNP@PAH-RB@PSS.

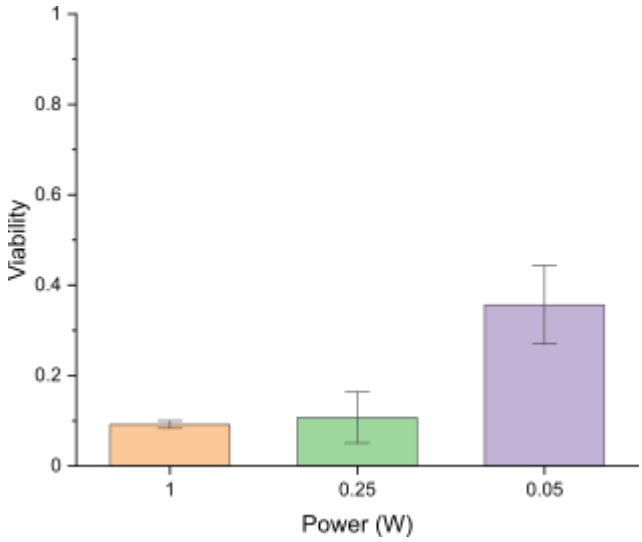

Figure 4.13 - Effect of 6 minute irradiation on HeLa cells incubated with 0.586 nM AuNP@PAH-RB@PSS for 3 hours. Irradiation power; 1 (orange), 0.25 (green) and 0.05 W (purple). The bars represent the mean of several experiments and the error bars represent the standard deviation.

When the amount of AuNP@PAH-RB@PSS in HeLa cells is reduced further to 1700, no significant killing is observed at any power, see figure 4.14, which shows that the limiting factor for cell killing is indeed the number of AuNPs contained by cells. This is significantly different to the effect of AuNP@cit, where the photodynamic effect is mediated simply by the product of total light dose and the number of AuNPs present.

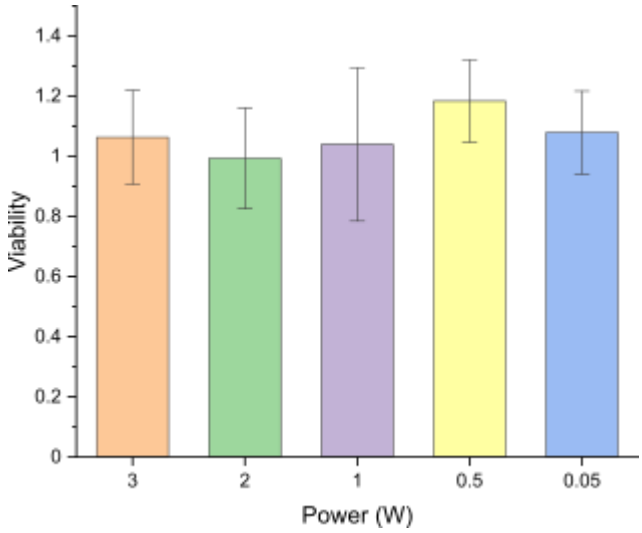

Figure 4.14– Effect of 6 minute irradiation on HeLa cells incubated with 0.147 nM AuNP@PAH-RB@PSS for 3 hours. Irradiation power; 3 (orange), 2 (green), 1 (purple), 0.5 (yellow) and 0.05 W (blue). The bars represent the mean of several experiments and the error bars represent the standard deviation.

4.6.5 Impact of Cell Heterogeneity

As discussed in chapter 3, the uptake of AuNPs by cells is heterogenous in nature. This has been reported to follow a log-normal distribution in literature where uptake of AuNPs has been assessed using single cell ICP-MS.[15] While we are dealing with substantially more cells in the well experiments described here than in the dish experiments in chapter 3 and therefore cell area does not need to be considered in order to explain individual killing results due to averaging over a much larger number of cells, the number of AuNPs contained in each cell will play a significant role in whether a cell is affected by the irradiation or not. In order to work out the threshold dose of AuNPs required for a cell to die, the AuNP content distribution of a population of cells was simulated based on distributions reported in literature with a log value variance of 0.7 and average log values of 0.753.[15] This distribution was then scaled for the mean AuNP content determined by ICP-OES for each incubation condition of 5200 and 3300, respectively, which resulted in distributions that can be seen in figure 4.15.

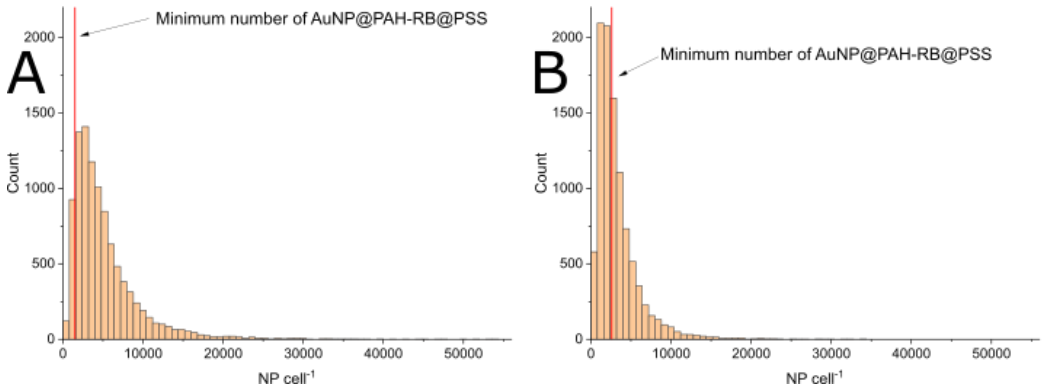

Figure 4.15 – Distributions and required number of nanoparticles per cell for a 1 W irradiation for 6 minutes. A) 0.586 nM, 3 hour incubation, B) 0.293 nM, 3 hour incubation. As the viability saturates at 0.1 and 0.54 at these conditions, the red line indicates the AuNP content corresponding to this efficacy.

The distribution allows determination of the required number of AuNP@PAH-RB@PSS required to kill a cell. The viability provides the fraction of cells affected by irradiation and as such this fraction can be applied to the modelled AuNP uptake distribution to find the minimum number of AuNPs required to kill a cell. However, this can only provide an accurate number when beam inhomogeneity does not affect

the results of irradiation. This is the case when all the Rose Bengal is bleached and killing reaches a plateau.

As such we have to primarily consider results where the killing plateau has been reached – for cells containing 3300 AuNP@PAH-RB@PSS, this occurs above 0.5 W, and the viability obtained for cells irradiated with 3 W for 6 minutes is ~0.54. This corresponds to a minimum AuNP content per cell of 2600, where 46% of cells contain more AuNPs and are therefore assumed to die. We can calculate the minimum AuNP content for killing at conditions of 1 W for cells containing 5,200 AuNP@PAH-RB@PSS per cell, where killing is saturated. The observed viability of 0.1 results in a required AuNP per cell of 1500. These results suggest that cells exposed to higher concentrations of AuNP@PAH-RB@PSS require fewer AuNP@PAH-RB@PSS for cells to die than in cells exposed to lower concentrations. This will be further discussed in 4.6.6.

4.6.6 Modelling of Cell Killing with AuNP@PAH-RB@PSS

Unlike AuNP@cit, NP@RB generate the $^1O_2$ primarily by excitation of Rose Bengal, which means that several additional variables must be taken into account: number of Rose Bengal per AuNP, estimated to be 7.2 in chapter 2, ε_{max} (35,000 M^{-1} cm^{-1}). Another key parameter is the maximum excitations of Rose Bengal, as this directly influences the amount of $^1O_2$ generated by AuNP@PAH-RB@PSS. The other variables are known; AuNP@PAH-RB@PSS per cell (3,300 determined from ICP-OES in 4.3), AuNP distribution w (0.72– taken from literature[15]), irradiation conditions, diameter of the well (6 mm), $1/e^2$ diameter of the laser (6 mm).

This leaves two variables unaccounted for; required dose of $^1O_2$ and the maximum excitations, which have been varied to get a good fit of all experimental results, which can be seen in table 4-1. In order to satisfactorily model the experimental data obtained for cells containing 3,300 AuNP@PAH-RB@PSS, the maximum excitations of Rose Bengal and the required $^1O_2$ dose were determined to be 35,000 and 5.5 x 10^8, respectively. The required $^1O_2$ dose is similar to that determined for AuNP@cit in section 4.5.4 and the maximum excitations of Rose Bengal is the correct order of magnitude, as experiments in our group on PAH-RB have shown. However, attempts

to use the same parameters for cells containing 5,200 AuNP@PAH-RB@PSS did not allow accurate modelling of the experimentally determined viability. As the maximum excitations of Rose Bengal is expected to be the same, the result can only be modelled if the required dose of $^1O_2$ is reduced. Using the same parameters obtained for cells containing 3,300 AuNP@PAH-RB for cells containing 1,700 AuNP@PAH-RB@PSS predicted a small reduction in viability, however no reduction was observed experimentally, to obtain the experimental result the required $^1O_2$ dose would have to be increased, however this was not attempted.

Irradiation power (W)	AuNP@PAH-RB@PSS (cell^{-1})	Maximum excitations of Rose Bengal	Required $^1O_2$ to kill cell (x 10^8)	Modelled viability	Experimental viability
3	3,300	63,000	5.5	0.26	0.55
0.05	3,300	63,000	5.5	0.82	0.87
3	3,300	63,000	7	0.38	0.55
0.05	3,300	63,000	7	0.88	0.87
3	**3,300**	**35,000**	**5.5**	**0.56**	**0.55**
0.05	**3,300**	**35,000**	**5.5**	**0.83**	**0.87**
0.05	5,200	35,000	5.5	0.67	0.35
0.05	5,200	60,000	5.5	0.66	0.35
0.05	**5,200**	**35,000**	**2.75**	**0.38**	**0.35**
3	1,700	35,000	5.5	0.86	1

Table 4-1 – Changing of parameters in model to fit killing in AuNP@PAH-RB@PSS, see text for other parameters. The best fits are shown in bold.

This reduction is in line with the results reported in 4.6.5 where the required amount of AuNP@PAH-RB@PSS to kill was significantly lower in cells containing 5,200 AuNP@PAH-RB@PSS (1,500) than in cells containing 3,300 AuNP@PAH-RB@PSS (2,600). These values are not affected by beam inhomogeneity due to the bleach of all Rose Bengal molecules, so they confirm the modelling results that cells exposed to higher concentrations of AuNP@PAH-RB@PSS require less $^1O_2$ to achieve killing than cells exposed to lower concentrations.

It is tempting to speculate that this observation is related to the suggested mechanism of cell death and mechanism of uptake by AuNPs. When AuNPs are taken up by endocytosis, higher incubation concentrations lead to more AuNPs per endosome as more AuNPs are on the cell membrane when it is taken into the cell through endocytosis.[16] This leads to higher doses of $^1O_2$ per endosome upon irradiation and as apoptosis is typically triggered through endosomal release of caspases due to endosomal destruction, endosomes containing more AuNPs, which are more likely to be destroyed than endosomes containing fewer AuNPs under the same irradiation conditions, are also more likely to trigger cell death.

4.6.7 Comparison of the Efficacy of AuNP@PAH-RB@PSS to other PS and AuNP@PS Conjugates

NP-sensitiser	Sensitiser concentration (M)	NP concentration (nM)	Incubation time (hour)	Sensitiser Uptake per cell	Light dose (J cm^{-2})
Mesoporous silica@RB [17]	1.4×10^{-5}	0.5	5	-	-
AuNP@phthalocyanine [18]	1×10^{-6}	0.5	4	-	2.2
AuNR@RB [19]	5.5×10^{-7}	-	4	400,000	15.3
AuNP@PPIX [20]	4×10^{-6}	-	4	-	10
AuNP@ALPcS$_4$ [5]	7×10^{-6}	0.5	4	-	72
RB Acetate [21]	1×10^{-6}	n/a	1	-	144
AuNP@PAH-RB@PSS	1.2×10^{-8}	0.586	3	37,500	75

Table 4-2 - Experimental conditions of NP-sensitiser and Rose Bengal acetate complexes

A wide range of nanoparticle–photosensitiser conjugates for photodynamic therapy have been previously reported in literature. Cal-27 cells were treated with 0.5 nM of electrostatically bound AuNR@PAH@RB with an estimated 2000 RBs per AuNR for 4 hours and irradiated with a total light dose of 15.3 J cm^{-2} resulted in a viability of 0.75.[19] The uptake of these AuNRs is significantly less than AuNP@PAH-RB@PSS and the total light dose is roughly a fourth of our lowest (average) dose. AuNP@PAH-

RB@PSS contains significantly less RB, which somewhat compensates for this disparity, however AuNP@PAH-RB@PSS shows more effective killing when RB uptake and the cumulative light dose are considered. This disparity may be explained by the displacement of Rose Bengal by serum proteins. As Rose Bengal makes up the outer layer of the AuNR, it may be displaced by the protein corona upon exposure to culture media – this has been observed in Rose Bengal attached liposomes where loosely bound external RB is displaced when serum is added to the solution.[22] The results contained in this paper show that AuNR@PAH@RB killing is mediated by apoptosis, this is in agreement with the results presented here that any effect on viability is delayed, which would indicate apoptosis. It is likely that a similar mechanism is used by AuNP@PAH-RB@PSS, as the AuNRs are also confined to intracellular vesicles so singlet oxygen generated by either nanoparticle is likely to damage similar parts of the cell and trigger similar apoptic pathways.

160 nm Mesoporous silica nanoparticles loaded with 4.2 $x10^4$ Rose Bengal molecules per nanoparticle showed toxicity under light against melanoma cells (SK-MEL-28) when incubated at 1.4 x 10^{-10} mol dm^{-3} for 5 hours, upon irradiation with green light (50% reduction – unknown light dose).[17] AuNPs conjugated to a phthalocyanine dye were localised within endosomes and showed a 50% reduction in viability of HeLa cells at a light dose of 1.92 J cm^{-2}, with a dark viability of 70%. [18] While the light dose was significantly less than the light dose used in our experiments, the concentration of phthalocyanine dye used in vitro was 0.55 µM in a 4 hour incubation which is significantly higher than the concentration of RB used in our experiments. Protoporphyrin IX AuNP conjugates have also been used on HeLa cells, showing significant cell killing when used with a light dose of 10 J cm^{-2}, however the concentration of dye used in vitro was in the µM range which again is much greater than the RB concentration used in the results presented here.[20] AuNRs assembled using a layer by layer process with the photosensitiser AlPcS4 as the outer layer showed high cytotoxicity under a 672 nm light dose of 72 J cm^{-2} for human breast cancer cells (MCF-7) following a 4 hour incubation with 0.5 nM AuNR@PSS@PEI@AlPcS4 (photosensitiser concentration 7 µM).[5] While the uptake of the photosensitiser may be limited as it may be displaced by serum proteins on

addition to media, the AuNR concentration is similar to the AuNP@PAH-RB@PSS and cytotoxicity is at a similar level.

In addition to photosensitiser loaded nanoparticles, we can also compare our results to Rose Bengal and Rose Bengal acetate mediated photodynamic therapy. Literature shows that free Rose Bengal can show significant toxicity under illumination to cells, however this is at concentrations above 1 μM.[19] Rose Bengal acetate features acetate groups to increase the ability of RB to cross cell membranes, upon uptake these groups are enzymatically removed and the singlet oxygen generating function is regained. HeLa cells irradiated with 144 J cm^{-2} after a 1 hour incubation of 1 μM doses of Rose Bengal acetate showed a viability of 0.35 compared to unirradiated cells.[21] This treatment induced apoptosis in HeLa cells, further work showed that Rose Bengal Acetate could trigger at least 4 different apoptic pathways.[23] As the RB contained within AuNP@PAH-RB@PSS is at a concentration of 11 nM (0.586 nM AuNP@PAH-RB@PSS concentration), the ability of AuNP@PAH-RB@PSS to successfully deliver RB within cell shows great promise.

While direct comparison to work within the literature is difficult due to a lack of quantitative uptake data, it is clear that AuNP@PAH-RB@PSS provides a therapeutic effect at similarly low laser powers to many reported PDT conjugates and Rose Bengal powers. It provides this effect at much lower concentrations of Rose Bengal when compared to both the free dye and AuNRs with Rose Bengal as an electrostatically attached outer layer.

4.7 Conclusion

The efficacy of AuNP@cit and AuNP@PAH-RB@PSS were tested for PDT against HeLa cells using a whole population assay based on MTT, and despite the necessary reduction in intensity killing was observed for both AuNPs. However, only limited killing was achieved for AuNP@cit and this could not be increased due to the increased sensitivity to light observed in wells. The irradiation conditions could not be increased further and the uptake could not be increased further without further increasing AuNP@cit toxicity alone. This is also limited by heating, as if either of these

parameters are further increased the cells would reach the photothermal heating limit and PTT would dominate.

AuNP@PAH-RB@PSS showed exceptional killing compared to AuNP@cit, with reduced toxicity and requiring much lower light doses. It was observed that the Rose Bengal bleaches, and under most conditons the key determinant of whether enough $^1O_2$ was generated to kill cells was the amount of AuNP@PAH-RB@PSS uptake.

The use of modelling allowed us to estimate the dose of singlet oxygen required to kill HeLa cells, and the use both of the cell distributions at high powers and of the full model at low powers showed that cells with a higher average AuNP@PAH-RB@PSS concentration required a lower dose of $^1O_2$ to be killed.

4.8 References

(1) Chithrani, B. D.; Ghazani, A. A.; Chan, W. C. W. Determining the Size and Shape Dependence of Gold Nanoparticle Uptake into Mammalian Cells. *Nano Lett.* **2006**, *6* (4), 662–668. https://doi.org/10.1021/nl052396o.

(2) Klingberg, H.; Oddershede, L. B.; Loeschner, K.; Larsen, E. H.; Loft, S.; Møller, P. Uptake of Gold Nanoparticles in Primary Human Endothelial Cells. *Toxicol. Res. (Camb).* **2015**, *4* (3), 655–666. https://doi.org/10.1039/c4tx00061g.

(3) Zhang, Y.; Xu, D.; Li, W.; Yu, J.; Chen, Y. Effect of Size, Shape, and Surface Modification on Cytotoxicity of Gold Nanoparticles to Human HEp-2 and Canine MDCK Cells. *J. Nanomater.* **2012**, *2012*. https://doi.org/10.1155/2012/375496.

(4) Davidson, A. M.; Brust, M.; Cooper, D. L.; Volk, M. Sensitive Analysis of Protein Adsorption to Colloidal Gold by Differential Centrifugal Sedimentation. *Anal. Chem.* **2017**, *89* (12), 6807–6814. https://doi.org/10.1021/acs.analchem.7b01229.

(5) Shi, Z.; Ren, W.; Gong, A.; Zhao, X.; Zou, Y.; Brown, E. M. B.; Chen, X.; Wu, A. Stability Enhanced Polyelectrolyte-Coated Gold Nanorod-Photosensitizer Complexes for High/Low Power Density Photodynamic Therapy. *Biomaterials* **2014**, *35* (25), 7058–7067. https://doi.org/10.1016/j.biomaterials.2014.04.105.

(6) Reibetanz, U.; Claus, C.; Typlt, E.; Hofmann, J.; Donath, E. Defoliation and Plasmid Delivery with Layer-by-Layer Coated Colloids. *Macromol. Biosci.* **2006**, *6* (2), 153–160. https://doi.org/10.1002/mabi.200500163.

(7) Zyuzin, M. V.; Cassani, M.; Barthel, M. J.; Gavilan, H.; Silvestri, N.; Escudero, A.; Scarpellini, A.; Lucchesi, F.; Teran, F. J.; Parak, W. J.; Pellegrino, T. Confining Iron Oxide Nanocubes inside Submicrometric Cavities as a Key Strategy to Preserve Magnetic Heat Losses in an Intracellular Environment. *ACS Appl. Mater. Interfaces* **2019**, *11* (45), 41957–41971. https://doi.org/10.1021/acsami.9b15501.

(8) Carnovale, C.; Bryant, G.; Shukla, R.; Bansal, V. Identifying Trends in Gold Nanoparticle Toxicity and Uptake: Size, Shape, Capping Ligand, and Biological Corona. *ACS Omega* **2019**, *4* (1), 242–256. https://doi.org/10.1021/acsomega.8b03227.

(9) Hauck, T. S.; Ghazani, A. A.; Chan, W. C. W. Assessing the Effect of Surface Chemistry on Gold Nanorod Uptake, Toxicity, and Gene Expression in Mammalian Cells. *Small* **2008**, *4* (1), 153–159. https://doi.org/10.1002/smll.200700217.

(10) Moore, K. A.; Pate, K. M.; Soto-Ortega, D. D.; Lohse, S.; van der Munnik, N.; Lim, M.; Jackson, K. S.; Lyles, V. D.; Jones, L.; Glassgow, N.; Napumecheno, V. M.; Mobley, S.; Uline, M. J.; Mahtab, R.; Murphy, C. J.; Moss, M. A. Influence of Gold Nanoparticle Surface Chemistry and Diameter upon Alzheimer's

Disease Amyloid-β Protein Aggregation. *J. Biol. Eng.* **2017**, *11* (1), 1–11. https://doi.org/10.1186/s13036-017-0047-6.

(11) Wang, L.; Liu, Y.; Li, W.; Jiang, X.; Ji, Y.; Wu, X.; Xu, L.; Qiu, Y.; Zhao, K.; Wei, T.; Li, Y.; Zhao, Y.; Chen, C. Selective Targeting of Gold Nanorods at the Mitochondria of Cancer Cells: Implications for Cancer Therapy. *Nano Lett.* **2011**, *11* (2), 772–780. https://doi.org/10.1021/nl103992v.

(12) Wang, P.; Wang, X.; Wang, L.; Hou, X.; Liu, W.; Chen, C. Interaction of Gold Nanoparticles with Proteins and Cells. *Sci. Technol. Adv. Mater.* **2015**, *16* (3), 34610. https://doi.org/10.1088/1468-6996/16/3/034610.

(13) Summers, H. D.; Brown, M. R.; Holton, M. D.; Tonkin, J. A.; Hondow, N.; Brown, A. P.; Brydson, R.; Rees, P. Quantification of Nanoparticle Dose and Vesicular Inheritance in Proliferating Cells. *ACS Nano* **2013**, *7* (7), 6129–6137. https://doi.org/10.1021/nn4019619.

(14) He, Y.; Hua, W. H.; Low, M. C.; Tsai, Y. H.; Cai, C. J.; Chiang, H. C.; Yu, J. H.; Hsiao, J. H.; Tseng, P. H.; Kiang, Y. W.; Yang, C. C.; Zhang, Z. Exocytosis of Gold Nanoparticle and Photosensitizer from Cancer Cells and Their Effects on Photodynamic and Photothermal Processes. *Nanotechnology* **2018**, *29* (23). https://doi.org/10.1088/1361-6528/aab933.

(15) Jeynes, J. C. G.; Jeynes, C.; Merchant, M. J.; Kirkby, K. J. Measuring and Modelling Cell-to-Cell Variation in Uptake of Gold Nanoparticles. *Analyst* **2013**, *138* (23), 7070. https://doi.org/10.1039/c3an01406a.

(16) Krpetić, Ž.; Nativo, P.; Sée, V.; Prior, I. A.; Brust, M.; Volk, M. Inflicting Controlled Nonthermal Damage to Subcellular Structures by Laser-Activated Gold Nanoparticles. *Nano Lett.* **2010**, *10* (11), 4549–4554. https://doi.org/10.1021/nl103142t.

(17) Gianotti, E.; Martins Estevão, B.; Cucinotta, F.; Hioka, N.; Rizzi, M.; Renò, F.; Marchese, L. An Efficient Rose Bengal Based Nanoplatform for Photodynamic Therapy. *Chem. - A Eur. J.* **2014**, *20* (35), 10921–10925. https://doi.org/10.1002/chem.201404296.

(18) Wieder, M. E.; Hone, D. C.; Cook, M. J.; Handsley, M. M.; Gavrilovic, J.; Russell, D. A. Intracellular Photodynamic Therapy with Photosensitizer-Nanoparticle Conjugates: Cancer Therapy Using a 'Trojan Horse.' *Photochem. Photobiol. Sci.* **2006**, *5* (8), 727–734. https://doi.org/10.1039/b602830f.

(19) Wang, B.; Wang, J. H.; Liu, Q.; Huang, H.; Chen, M.; Li, K.; Li, C.; Yu, X. F.; Chu, P. K. Rose-Bengal-Conjugated Gold Nanorods for Invivo Photodynamic and Photothermal Oral Cancer Therapies. *Biomaterials* **2014**, *35* (6), 1954–1966. https://doi.org/10.1016/j.biomaterials.2013.11.066.

(20) Savarimuthu, W. P.; Gananathan, P.; Rao, A. P.; Manickam, E.; Singaravelu, G. Protoporphyrin IX-Gold Nanoparticle Conjugates for Targeted Photodynamic Therapy - An in-Vitro Study. *J. Nanosci. Nanotechnol.* **2015**, *15* (8), 5577–5584. https://doi.org/10.1166/jnn.2015.10302.

(21) Panzarini, E.; Tenuzzo, B.; Palazzo, F.; Chionna, A.; Dini, L. Apoptosis Induction and Mitochondria Alteration in Human HeLa Tumour Cells by Photoproducts of Rose Bengal Acetate. *J. Photochem. Photobiol. B Biol.* **2006**, *83* (1), 39–47. https://doi.org/10.1016/j.jphotobiol.2005.11.014.

(22) Kautzka, Z.; Clement, S.; Goldys, E. M.; Deng, W. Light-Triggered Liposomal Cargo Delivery Platform Incorporating Photosensitizers and Gold Nanoparticles for Enhanced Singlet Oxygen Generation and Increased Cytotoxicity. *Int. J. Nanomedicine* **2017**, *Volume 12*, 969–977. https://doi.org/10.2147/IJN.S126553.

(23) Panzarini, E.; Inguscio, V.; Dini, L. Timing the Multiple Cell Death Pathways Initiated by Rose Bengal Acetate Photodynamic Therapy. *Cell Death Dis.* **2011**, *2* (6), 1–11. https://doi.org/10.1038/cddis.2011.51.

(24) Palamà, I. E.; Coluccia, A. M. L.; Gigli, G. Uptake of Imatinib-Loaded Polyelectrolyte Complexes by BCR-ABL+ Cells: A Long-Acting Drug-Delivery Strategy for Targeting Oncoprotein Activity. *Nanomedicine* **2014**, *9* (14), 2087–2098. https://doi.org/10.2217/NNM.13.147.

(25) Song, Y.; Zhou, Y.; Chen, L. Wood Cellulose-Based Polyelectrolyte Complex Nanoparticles as Protein Carriers. *J. Mater. Chem.* **2012**, *22* (6), 2512–2519. https://doi.org/10.1039/c1jm13735b.

(26) Palamà, I. E.; Musarò, M.; Coluccia, A. M. L.; D'Amone, S.; Gigli, G. Cell Uptake and Validation of Novel PECs for Biomedical Applications. *J. Drug Deliv.* **2011**, *2011*, 1–7. https://doi.org/10.1155/2011/203676.

(27) Jeong, Y. J.; Lee, D. Y.; Choe, K.; Ahn, H.; Kim, P.; Park, J. H.; Kim, Y. C. Polypeptide-Based Polyelectrolyte Complexes Overcoming the Biological Barriers of Oral Insulin Delivery. *J. Ind. Eng. Chem.* **2017**, *48*, 79–87. https://doi.org/10.1016/j.jiec.2016.12.022.

5 Investigation of the effect of p53 on AuNP mediated PDT

5.1 Introduction

While HeLa cells are widely used, they are not the best representation of human cancer cells due to their widespread and inconsistent properties. In order to test the efficacy of AuNP@cit and AuNP@PAH-RB@PSS, UM-SCC-1 cells were obtained, which are head and neck squamous cell carcinoma cells (HNSCC). For applications of AuNPs as PSs for PDT treatment of tumour beds in the head and neck, these cells provide a better model.

The p53 status of HNSCC is typically lost or reduced through tumorigenesis, and this plays a key role in reducing apoptosis and it has been observed in radiation treatments that the glycolytic metabolism that these adopt reduces their sensitivity to ROS.[1] It has been reported in literature that cells lacking p53 are less sensitive to ROS, and as many HNSCC cells are p53 negative, it is important to establish what effect the absence of p53 has on the treatment prosed here, this has been discussed in more detail in section 1.1.5. For this purpose three isogenic UM-SCC-1 cell lines were compared; UM-SCC-1 which has no p53 expression, UM-SCC-1 p53 WT which has p53 expression due to the reintroduction of p53 WT and UM-SCC-1 pBABE which has no p53 expression but has had a control gene reinserted at the same position as p53 WT was introduced in UM-SCC-1 p53 WT.

5.2 Experimental

5.2.1 Materials and Equipment

Dulbecco's Modified Eagle Medium (DMEM), heat inactivated fetal bovine serum, non-essential amino acids, Penicillin-Streptomycin, MTT (3-(4,5-Dimethylthiazol-2-yl)-2,5-Diphenyltetrazolium Bromide (MTT), DMSO and Dulbecco's phosphate buffered saline (Mg^{2+}, Ca^{2+}, glucose, pyruvate) (DPBS) (pH 7.4) were purchased from ThermoFisher. Corning cell culture plates and flasks were purchased from Fisher Scientific.

MTT assays were performed on a Molecular Devices F3 Filtermax plate reader.

5.2.2 AuNP Preparation

13.8 nm gold nanoparticles (AuNP@cit, AuNP@PAH-RB@PSS, AuNP@PAH@PSS) were prepared as described in chapter 2.2. The concentration of all AuNPs was determined by the size of the gold core (determined via DCS) and their absorbance at 450 nm according to literature.[2]

5.2.3 Irradiation Setup

Four wells were seeded with 4000 or 8000 UM-SCC-1, UM-SCC-1 pBABE or UM-SCC-1 p53 WT cells in 96-well plates in 100 µL DMEM (10% FBS, 1% P/S, 1% NEAA) and left overnight in an incubator (5% CO_2). AuNPs were mixed with DMEM (1:1, DMEM:AuNP/MQ-H_2O) and the DMEM was replaced with the AuNP mixture or a 1:1 DMEM:MQ-H_2O mixture and left for either 3 or 24 hours (incubation time, final AuNP concentration and AuNP type will be stated for each experiment). Following the incubation, cells were washed three times with 100 µL DPBS (Mg^{2+}, Ca^{2+}, glucose, pyruvate) and then the wells were filled with 300 µL DPBS. One of the four wells was irradiated with CW 532 nm laser with a $1/e^2$ beam width of 1.9 mm which had been expanded using a -50 mm lens to a beam diameter of 10 mm, which passed through a 6mm aperture directly below the well (see figure 4.1 for details, however the lens used was -50 mm rather than -100 mm). In order to prevent scattered light affecting the control wells they were covered during irradiation. For experiments with AuNP@cit, the beam diameter reported previously in chapter 4 was used. Following irradiation, the DPBS was replaced with 100 µL DMEM and the well plate was placed back in the incubator for 20 hours.

5.2.4 Incubation of Cells with no Irradiation

12 wells were seeded with 4000 (24 hour incubations) or 8000 (3 hour incubations) cells in a 96 well plate in 100 µL DMEM and left overnight in an incubator. AuNP solutions prepared as above were then added to 6 wells and 1:1 DMEM:MQ-H_2O was added to 6 wells. Following incubation with AuNPs or 1:1 MQ-H_2O the cells were washed as above with DPBS, 100 µL DMEM was added and placed in the incubator for a further 20 hours.

5.2.5 Determining Viability

The DMEM was replaced with 100 µL MTT solution (10% 5 mg/mL MTT, 90% DMEM), and after 4 hours the MTT solution was removed and 100 µL of dimethyl sulfoxide (DMSO) was added. This was left for 20 minutes to solubilise in the incubator before the absorbance was assessed at 595 nm and 620 nm for each well using a plate reader. Following the standard protocol for the MTT assay, viability was calculated by dividing the absorbance difference (595-620) of the irradiated wells by the absorbance difference of the control wells, which can be seen in equation 5-1.

$$Viability = \frac{Absorbance\ of\ irradiated\ cell_{595\ nm} - Absorbance\ of\ irradiated\ cell_{620\ nm}}{Average\ (Absorbance\ of\ control\ cell_{595\ nm} - Absorbance\ of\ control\ cell_{620\ nm})}$$

Equation 5-1 – Determination of viability of irradiated cell using MTT assay

5.2.6 Determining Mean Cellular Uptake of AuNPs

Cells were seeded in 100 mm dishes and left overnight to attach to the surface of the dish. Subsequently, the media was replaced with 10 mL of 1:1 media to AuNP@PAH-RB@PSS or AuNP@cit solution at a final concentration of 0.073 nM and 1 nM, respectively. After 3 hours (AuNP@PAH-RB@PSS) or 18 hours (AuNP@cit), the solution was removed and the cells were washed 3 times with fresh DPBS. The cells were then detached using 1 mL trypsin and resuspended in 9 mL media. At this stage, 0.024 mL was removed and used for cell counting in a haemocytometer. After counting, the cell suspension was centrifuged (1000 RCF, 10 minutes) and the supernatant was removed. 0.5 mL aqua regia was added to the pellet and left for 3 days. 4.5 mL MQ-H_2O was added to the solution and the concentration of gold was then determined using ICP-OES.

5.3 Uptake of AuNPs by UM-SCC-1 and Derivative Cells

UM-SCC-1 cells exposed to 1 nM AuNP@cit for 18 hours resulted in a mean AuNP per cell uptake of 178,000±21,000. The average AuNP uptake per cell of UM-SCC-1 cells when incubated with 0.073 nM AuNP@PAH-RB@PSS for 3 hours was determined to be 1900±200. The average uptake of AuNP@PAH-RB@PSS by UM-SCC1 p53 WT and UM-SCC-1 pBABE cells was determined to be 900±100 and 2900±300, respectively, see figure 5.1.

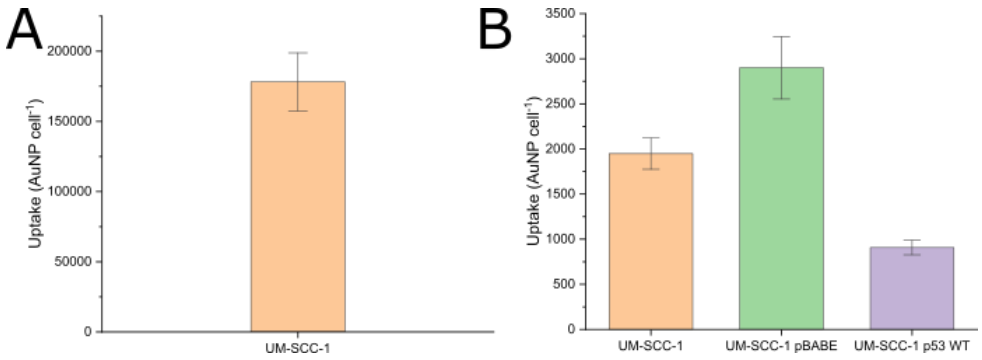

Figure 5.1 – A) Cellular uptake of UM-SCC-1 cells after incubation with AuNP@cit at a concentration of 1 nM for 18 hours. B) Cellular uptake of UM-SCC-1 (orange), UM-SCC-1 pBABE (green) and UM-SCC-1 p53 WT (purple) after incubation with 0.073 nM AuNP@PAH-RB@PSS for 3 hours. The bars represent the mean of several experiments and the error bars represent the standard deviation

The differentiation of uptake between UM-SCC-1, UM-SCC-1 pBABE and UM-SCC-1 p53 WT likely arises through shifting cellular metabolism. The shift in metabolism has been observed in UM-SCC-1 cells through the re-introduction of TP53 functionality into the cells.[1] As cells lacking p53 have Warburg metabolism and a dependence on glycolysis as opposed to respiration, they also upregulate their intake of resources from their surroundings. It has been shown that cells with a dependence on glycolysis have an increased appetite for nutrients due to their rapidly proliferating status.[3] The presence of p53 has been shown to downregulate the expression of glucose transporters GLUT1 and GLUT4, which is upregulated in the absence of p53 in order to supply enough glucose to continue glycolysis.[4] Previous work on targeting nanoparticles to tumour cells have exploited overexpression of receptors such as HER2 and folate on the surface of cancer cells to achieve enhanced cellular uptake.[5,6] HER2 expression has been shown to be dependent upon the p53 status of cells, with HeLa and SAOS cells showing reduced HER2 expression upon addition of exogenous wt p53 (HeLa contains p53 but its effects are somewhat negated by HPV-E6) or introduction of wt p53 (SAOS cells are p53 null).[7] Transferrin receptor (TfR1) silencing has been shown to increase p53 levels in FTC-133 and 8305C human thyroid cancer cells, and inducing the presence of p53 in H1299 lung cancer cells has been shown to downregulate TrF1 expression.[89] Expression of TFR was downregulated in HCT116 containing p53 following DNA damage but not in HCT116 cells without p53, this shows the significant effect that p53 has upon endocytic signalling.[10]

While the exact receptors involved in the uptake of AuNP@PAH-RB@PSS are unknown, they are likely to be mediated by serum proteins.[11] In light of the upregulation of receptors in cancer cells and in cells without p53 due to their different metabolic requirements, it is unsurprising that UM-SCC-1 p53 WT cells take up significantly less AuNPs as they primarily rely on respiration for energy and have lower nutrient requirements. As over 80% of HPV negative squamous cell carcinomas of the head and neck exhibit TP53 mutation, the increased uptake of AuNP@PAH-RB@PSS by p53 null UM-SCC-1 and UM-SCC-1 pBABE presents a route for passive targeting of cancer cells, even before active targeting of upregulated receptors is considered.

5.4 Control Experiments

5.4.1 Effect of Incubation of UM-SCC-1 and Derivative Cells with AuNPs

UM-SCC-1 cells incubated with 1 nM AuNP@cit for 18 hours and analysed after 24 hours using an MTT assay resulted in a viability of 0.73±0.03. UM-SCC-1, UM-SCC-1 pBABE and UM-SCC-1 p53 WT cells incubated with 0.073 nM AuNP@PAH-RB@PSS for 3 hours and analysed after 24 hours using a MTT assay showed viabilities of 0.83±0.20, 0.94±0.15 and 0.95±0.11, respectively. UM-SCC-1 cells treated with 0.073 nM AuNP@PAH@PSS for 3 hours and analysed after 24 hours using a MTT assay resulted in a viability of 0.73±0.28 Representative images of UM-SCC-1 and UM-SCC-1 p53 WT cells 24 hours after incubation with AuNP@PAH-RB@PSS can be seen in figure 5.2, which show no deformed cells.

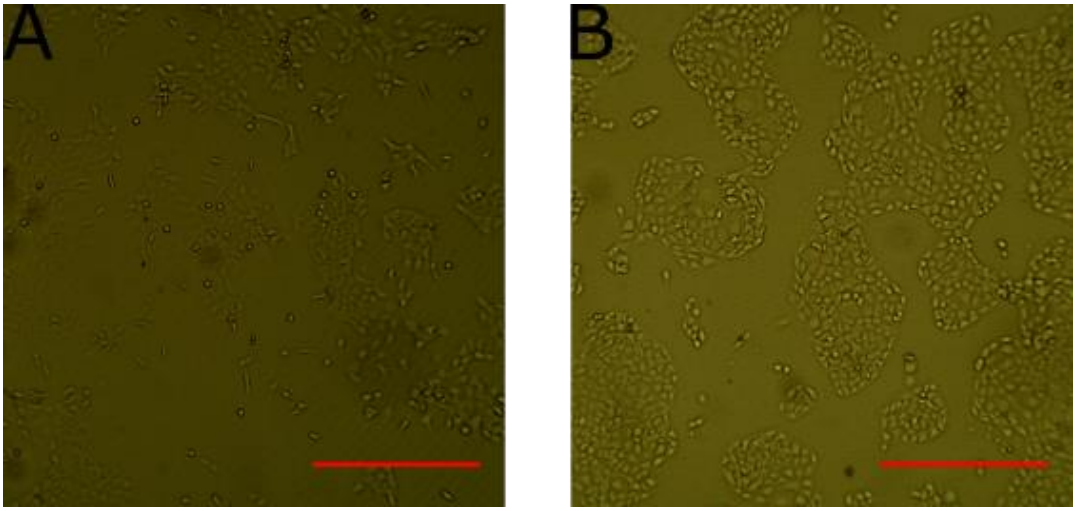

Figure 5.2 – Cells 24 hours after incubation with 0.073 nM AuNP@PAH-RB@PSS for 3 hours; A) UM-SCC-1, B) UM-SCC-1 p53 WT. Scale bar in all images represents 0.5 mm.

5.4.2 Irradiation in the of Absence of AuNP@PAH-RB@PSS and AuNP@cit of UM-SCC-1, UM-SCC-1 WTp53 and UM-SCC-1 pBABE Cells

Untreated UM-SCC-1 cells were irradiated with 3, 2, 1 and 0.05 W for 6 minutes and assessed using an MTT assay, resulting in viabilities of 0.97±0.04, 1.02±0.08, 1.05±0.05 and 1.12±0.26, respectively. Untreated UM-SCC-1 pBABE cells were irradiated with 3, 2, 1 and 0.05 W for 6 minutes and assessed using an MTT assay, resulting in viabilities of 0.85±0.12, 0.78±0.08, 0.85±0.18 and 0.92±0.12, respectively. Untreated UM-SCC-1 p53 WT were irradiated with 1 and 0.05 W and assessed using an MTT assay resulting in viabilities of 0.88±0.10 and 0.93±0.10 respectively. Representative images of UM-SCC-1 cells can be seen in figure 5.3, with no difference observable between treated and untreated cells.

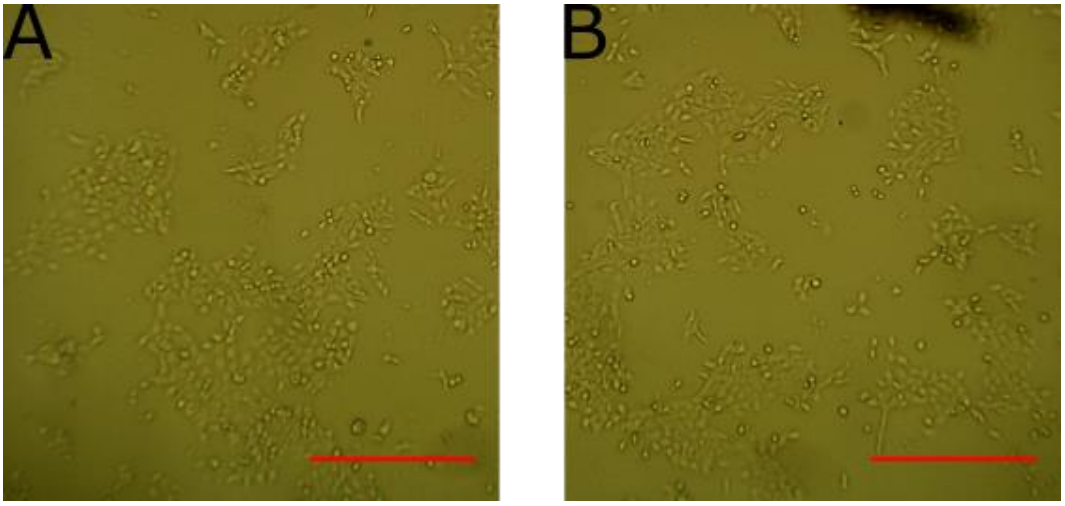

Figure 5.3 – UM-SCC-1 cells containing no AuNPs 24 hours after; A) irradiation with 50 mW for 6 minutes, B) no irradiation. Scale bar in all images represents 0.5 mm.

UM-SCC-1 cells were also irradiated with 3 W for 12 minutes, resulting in a viability of 1.00±0.12, this experiment was performed with a $1/e^2$ beam diameter of 6 mm.

AuNP@PAH-RB@PSS were centrifuged at 9000 RCF for 30 minutes, the supernatant was taken and diluted in the same way as 0.073 nM AuNP@PAH-RB@PSS. UM-SCC-1 cells were then incubated with this solution for 3 hours before being irradiated with 50 mW for 6 minutes and assessed with an MTT assay, resulting in a viability of 1.00±0.16, figure 5.4.

UM-SCC-1 cells were incubated with 0.073 nM AuNP@PAH@PSS for 3 hours before being irradiated with 0.05 W for 6 minutes and were assessed with an MTT assay resulting in a viability of 0.99±0.17, figure 5.4.

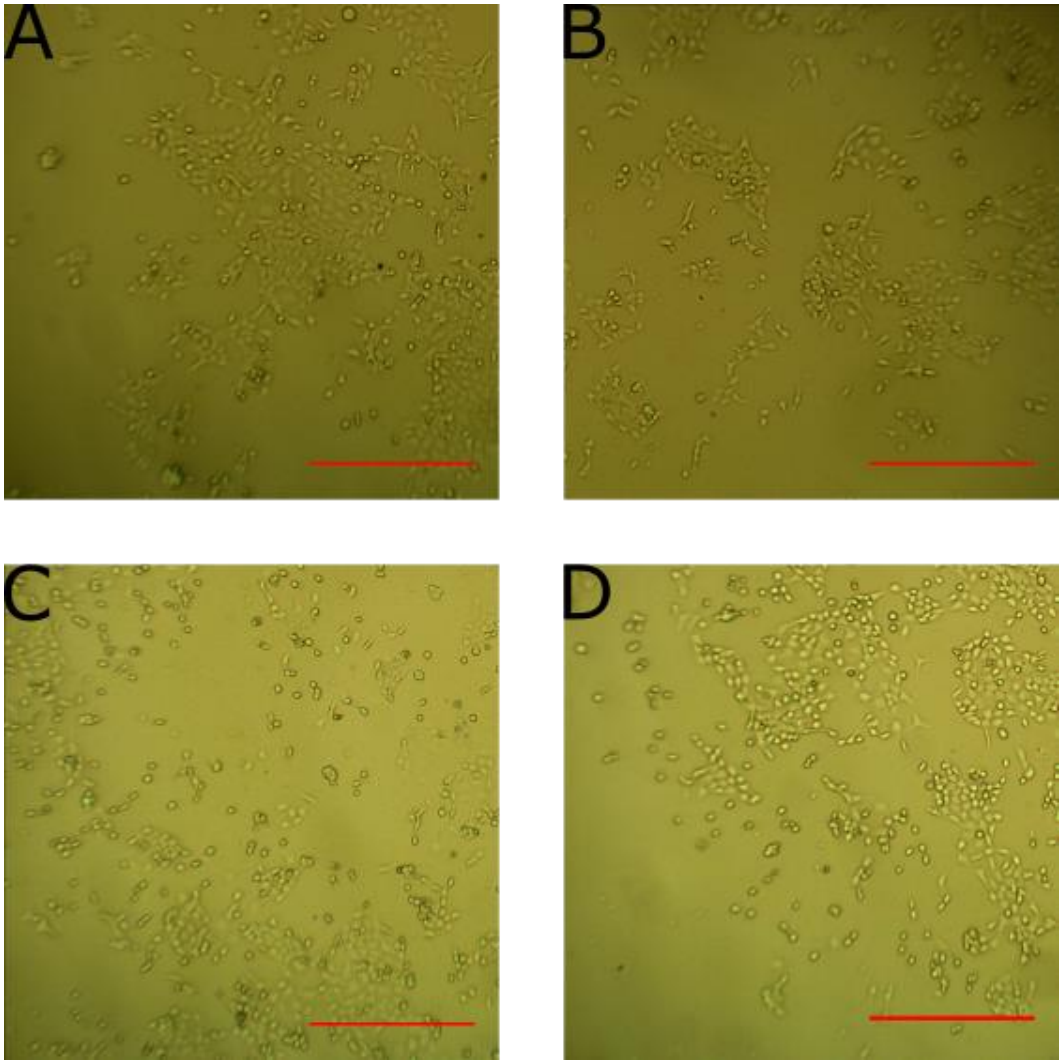

Figure 5.4 - Sections of wells containing UM-SCC-1 cells 24 hours after incubation with A, B) 0.073 nM (equivalent) supernatant for 3 hours, C, D) 0.073 AuNP@PAH@PSS for 3 hours. A, C) were irradiated with 0.05 W for 6 minutes, B, D) no irradiation. Scale bar in all images represents 0.5 mm.

While reduced viability was observed in UM-SCC-1 cells containing 1,900 AuNP@PAH-RB@PSS upon irradiation (section 5.6), it is important to rule out cell killing by light alone, or by irradiation after incubation with AuNP@PAH@PSS, or any free Rose Bengal present in the nanoparticle solution. Our results, shown in figure 5.5, clearly show that there is no killing by light alone, or by irradiation in the presence of AuNP@PAH@PSS or the Rose Bengal containing supernatant. We would not expect AuNP@PAH@PSS to create any light induced effect as without RB being incorporated into the nanoparticle at the concentrations used here not enough $^1O_2$ would be generated within the cell to damage it. It should not create any more $^1O_2$ or cell heating than AuNP@cit, section 5.5, which showed no killing even at much

higher cellular AuNP content. Literature shows that Rose Bengal alone is a poor photodynamic agent as it cannot cross the cell membrane due to its negative charge, so our results show that it is the incorporation of RB into the polyelectrolyte functionalised AuNP that provides a cytotoxic effect upon light irradiation.[12]

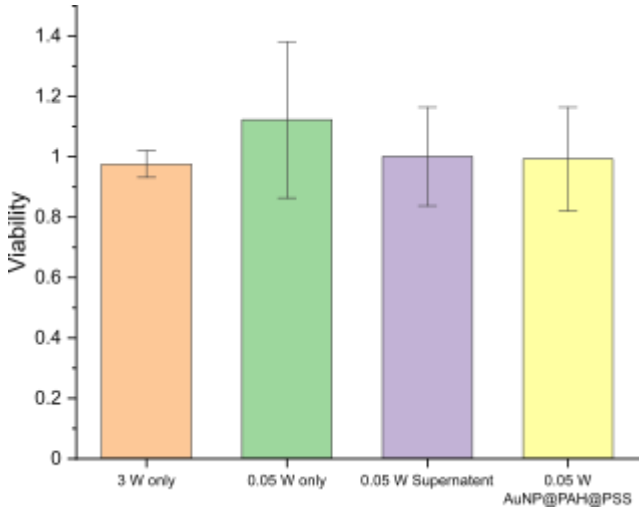

Figure 5.5 - Effect of 6 minute irradiation on UM-SCC-1 cells with power; 3 W (orange), 0.05 (green, purple, yellow) following a 3 hour incubation with 1:1 MQ-H_2O:media (orange, green), 0.073 nM supernatent (purple) or 0.073 nM AuNP@PAH@PSS (yellow). The bars represent the mean of several experiments and the error bars represent the standard deviation

5.5 Irradiation of UM-SCC-1 Cells Containing AuNP@cit

5.5.1 Temperature Increase in UM-SCC-1 Cells Containing AuNP@cit

Temperature increase, measured using a thermocouple, in experiments with cells containing 180,000 AuNP@cit, immediately following irradiation with a power of 3 W for 12 minutes, indicate that the temperature measured is never large enough to damage cells. The previously reported threshold of cell death is 45 °C, but the solvent surrounding the cells only reached 27.5 °C and this is consistent with temperature simulations reported in section 4.5.2, showing that the maximum temperature in the cell level would not exceed 37 °C for cells containing 180,000 AuNPs. Therefore, we can assume that cells are undamaged by any heating effect of AuNP@cit. In addition to the temperature not reaching the killing limit, viability of cells affected by irradiation with 3 W for 6 minutes and 12 minutes was not significantly different from the light alone controls, showing that any AuNP@cit temperature moderated effect

was insufficient to damage cells. The AuNP@cit experiments were carried out using the 6mm $1/e^2$ beam, the heating effect of this can be seen in chapter four, as the heating is independent of the cell type used and is rather determined by the amount of light absorbed by the sample, which in turn is dominated by the amount of AuNPs taken up by cells. As shown by the temperature simulations in section 4.5.2, the majority of heating takes place quickly (determined by the absorbance of the cell layer) before a gradual increase in temperature as irradiation time increases. This means that these results are in full agreement with the potential heating effect reported in chapter 4.

5.5.2 Effect of Irradiation on UM-SCC-1 Cells Containing AuNP@cit

UM-SCC-1 cells incubated with 1 nM AuNP@cit for 18 hours were exposed to 3 W irradiations for 12 minutes, resulting in a viability of 0.92±0.10, which can be seen in figure 5.6.

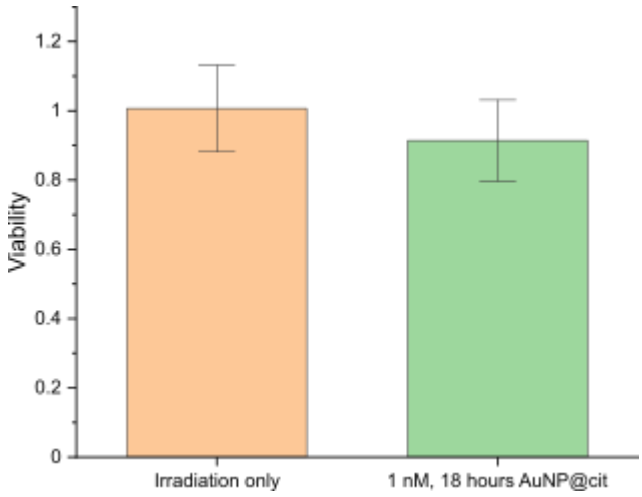

Figure 5.6 - Effect of 3 W irradiation for 12 minutes ($1/e^2$ laser diameter 6mm) on UM-SCC-1 cells following incubation with 1:1 MQ-H_2O:media (orange) or 1 nM AuNP@cit (green) for 18 hours. The bars represent the mean of several experiments and the error bars represent the standard deviation

When the AuNP@cit uptake is considered, this absence of an effect of the irradiation on cell viability is different to the results obtained in section 4.5.1 on HeLa cells using 3 W irradiation for 6 minutes. UM-SCC-1 cells contain 180,000 AuNP@cit, which is approximately half of the 320,000 AuNP@cit contained in HeLa cells in chapter 4. This means that the amount of $^1O_2$ generated is the similar in the two experiments, as the amount produced by AuNP@cit is proportional to the amount of light

absorbed by the AuNP. In HeLa cells this resulted in a viability of 0.75±0.07, which compares with the 0.92±0.10 reported here in UM-SCC-1 which shows significant killing effect. However, direct comparison is difficult because of potentially different uptake characteristics between cell lines. In HeLa cells, AuNP@cit internalised within intracellular vesicles with exceptional efficiency as shown in section 3.2.1. In the absence of TEM imaging for UM-CC-1 AuNP uptake, it is tempting to attribute the lack of PDT to poor internalisation of AuNP@cit by UM-SCC-1, similar to the reduced PDT effect in HeLa cells containing AuNP@CALNN as discussed in section 3.6.6. We were unable to further increase the AuNP@cit uptake as UM-SCC-1 cells showed poor surface attachment to the growth surface which was compounded for high concentrations of AuNPs and long incubation times.

5.6 Irradiation of UM-SCC-1 Cells Containing AuNP@PAH-RB@PSS

5.6.1 Temperature Increase in AuNP@PAH-RB@PSS

As the number of AuNPs per cell in these experiments is significantly less than in AuNP@cit experiments, it is expected that any heating is insignificant. UM-SCC-1 cells containing 1900 AuNP@PAH-RB@PSS per cell were irradiated with 1 W for 6 minutes, resulting in a maximum temperature measured in the solvent of 21.7 °C. This confirms that the solvent never reaches temperatures sufficient to kill cells and that killing must be moderated by a photodynamic mechanism rather than photothermal. In addition to this, only 55% of the light energy passes through the aperture, so even if there were larger amounts of AuNP@PAH-RB@PSS present in the cell there would be less heating than in both the HeLa experiments and the AuNP@cit experiments in this chapter.

5.6.2 Varying Irradiation Conditions

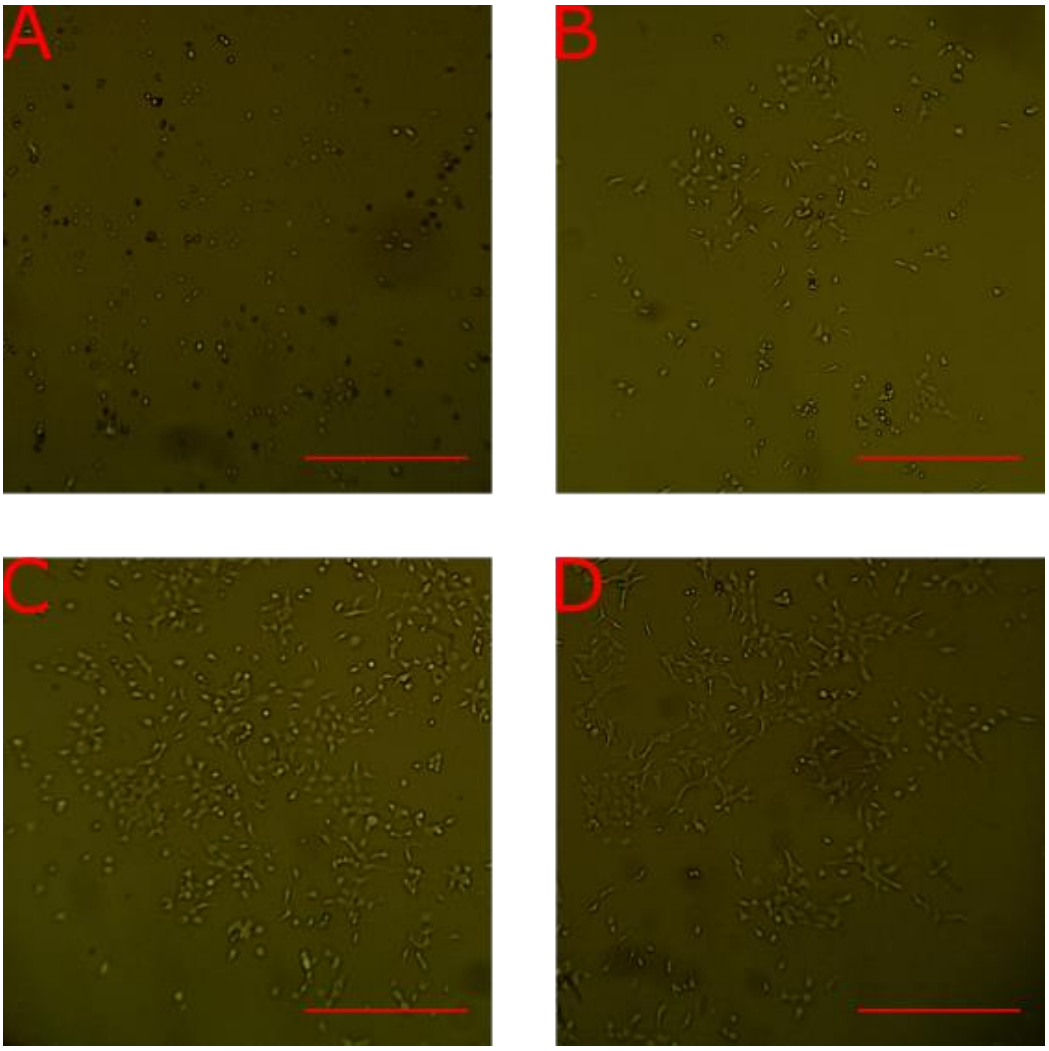

Figure 5.7 - Sections of wells containing UM-SCC-1 cells 24 hours after incubation with 0.073 nM AuNP@PAH-RB@PSS for 3 hours and irradiation with; A) 0.05 W for 6 minutes, B) 0.05 W for 2 minutes, C) 0.025 W for 2 minutes and D) no irradiation. Scale bar in all images represents 0.5 mm.

UM-SCC-1 cells incubated with 0.073 nM AuNP@PAH-RB@PSS for 3 hours, resulting in an uptake of 1,900 AuNP@PAH-RB@PSS per cell, were irradiated with 1 W for 6 minutes, 0.5 W for 6 minutes, 0.05 W for 6, 4, 2 minutes and 0.025 W for 2 minutes and assessed with a MTT assay, resulting in viabilities of 0.20±0.06, 0.23±0.05, 0.49±0.15, 0.49±0.04, 0.64±0.17 and 0.77±0.18, respectively. In addition to this, UM-SCC-1 cells were incubated with 0.073 nM AuNP@PAH-RB@PSS that had been washed immediately before incubation and irradiated with 0.05 W for 6 minutes resulting in a viability of 0.42±0.03 when assessed using MTT.

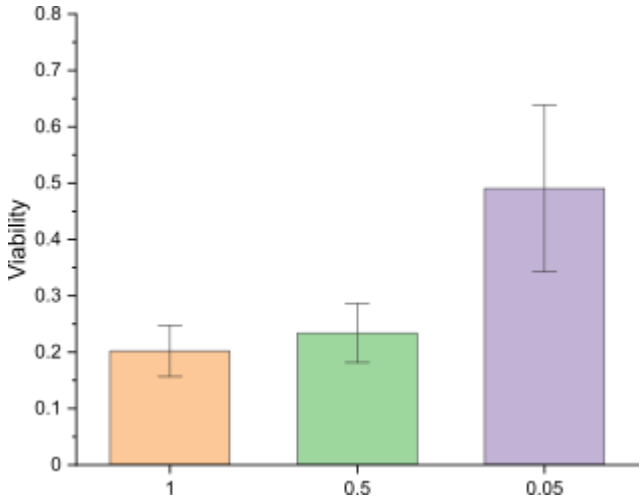

Figure 5.8 - Effect of 6 minute irradiation on UM-SCC-1 cells following incubation with 0.073 nM AuNP@PAH-RB@PSS with power; 1 W (orange), 0.5 W (green), 0.05 W (purple). The bars represent the mean of several experiments and the error bars represent the standard deviation.

UM-SCC-1 cells containing 1900 AuNP@PAH-RB@PSS show a similar saturation of killing as HeLa cells containing 3300 AuNP@PAH-RB@PSS in the previous chapter. This takes place as the maximum amount of $^1O_2$ is produced by irradiation at 0.5 W for 6 minutes, a further increase of the power to 1 W does not change the measured viability. This is due to the bleaching of Rose Bengal molecules in AuNP@PAH-RB@PSS, which limits $^1O_2$ production at higher powers. Despite a lower uptake of AuNP@PAH-RB@PSS (1900) in UM-SCC-1 vs HeLa cells (3,300) , the resulting plateau saturates at a viability of 0.2 instead of 0.55. This shows that UM-SCC-1 cells are more sensitive to reactive oxygen than HeLa cells, as despite the lower maximum singlet oxygen dose per cell more killing is observed.

When the power is lowered to 50 mW, we no longer bleach all of the Rose Bengal and as the amount of light used in the experiments is further reduced we see an increase in the viability reported, see figure 5.9. While the values for 4 and 6 minute 50 mW irradiations are similar, there is a large error associated with the 6 minute measurement, so the viability results still show the characteristic killing reduction with decreasing fluence.

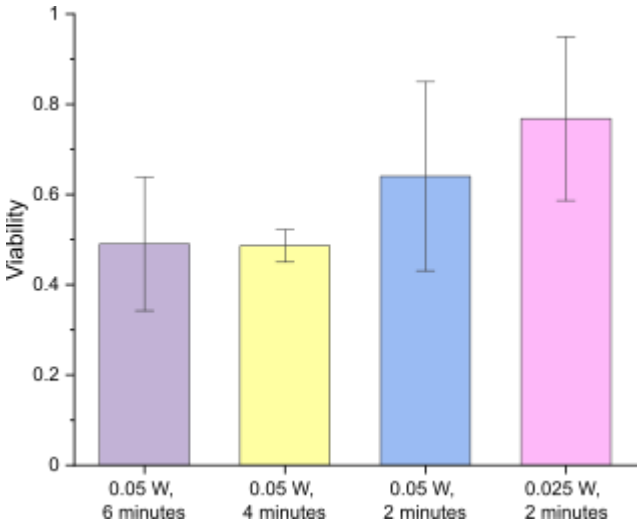

Figure 5.9 – Effect of 0.05 W (purple, yellow, blue) or 0.025 W (pink) irradiation on UM-SCC-1 cells following incubation with 0.073 nM AuNP@PAH-RB@PSS for 3 hours. Irradiation times; 6 minutes (purple), 4 minutes (yellow), 2 minutes (blue, pink). The bars represent the mean of several experiments and the error bars represent the standard deviation.

5.6.3 Varying Incubation Conditions

UM-SCC-1 cells incubated with AuNP@PAH-RB@PSS for 3 hours over a range of AuNP concentrations: 0.586, 0.293, 0.147, 0.073 nM were irradiated with 1 W for 6 minutes and assessed with MTT assays resulting in viabilities of 0.07±0.02, 0.06±0.01, 0.05±0.02 and 0.20 ±0.05, respectively. Changing the AuNP@PAH-RB@PSS concentration of the incubation solution that UM-SCC-1 cells were exposed to showed a similar trend to that seen in HeLa cells, as shown in figure 5.10.

Similarly, comparing cells incubated with 0.293 nM AuNP@PAH-RB@PSS for 3 hours to cells incubated with 0.073 nM AuNP@PAH-RB@PSS, irradiated with 50 mW for 6 minutes, shows a difference, with a factor 4 increase in concentration resulting in viability of 0.25±0.02 instead of 0.49±0.15. However, as the uptake for the higher concentration was not established, detailed conclusions cannot be drawn from this – it may be that uptake doesn't scale linearly with concentration.

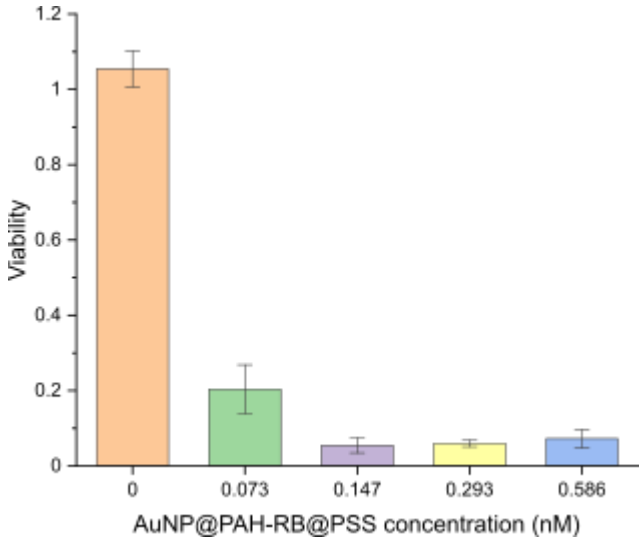

Figure 5.10 - Effect of 1 W irradiation for 6 minutes on UM-SCC-1 cells following incubation with AuNP@PAH-RB@PSS for 3 hours. Concentration used; 0 (orange), 0.073 (green), 0.147 (purple), 0.293 (yellow), 0.586 nM (blue). The bars represent the mean of several experiments and the error bars represent the standard deviation

5.7 Irradiation of UM-SCC-1 p53 WT and UM-SCC-1 pBABE Containing AuNP@PAH-RB@PSS

5.7.1 Irradiation of UM-SCC-1 p53 WT and UM-SCC-1 pBABE

UM-SCC-1 p53 WT cells incubated with 0.073 nM AuNP@PAH-RB@PSS for 3 hours were irradiated with 1, 0.5, 0.05 W for 6 minutes and 0.05 W for 4 and 2 minutes. These were then assessed using an MTT assay resulting in a viability of 0.13±0.06, 0.33±0.13, 0.45±0.10, 0.57±0.07 and 0.71±0.11 respectively, see figure 5.12. 50 mW irradiations all showed disrupted cellular morphologies observed using optical microscopy, as seen in figure 5.11. The black spots correspond to dead cells, and there is a clear sparsity of cells in 5.11A.

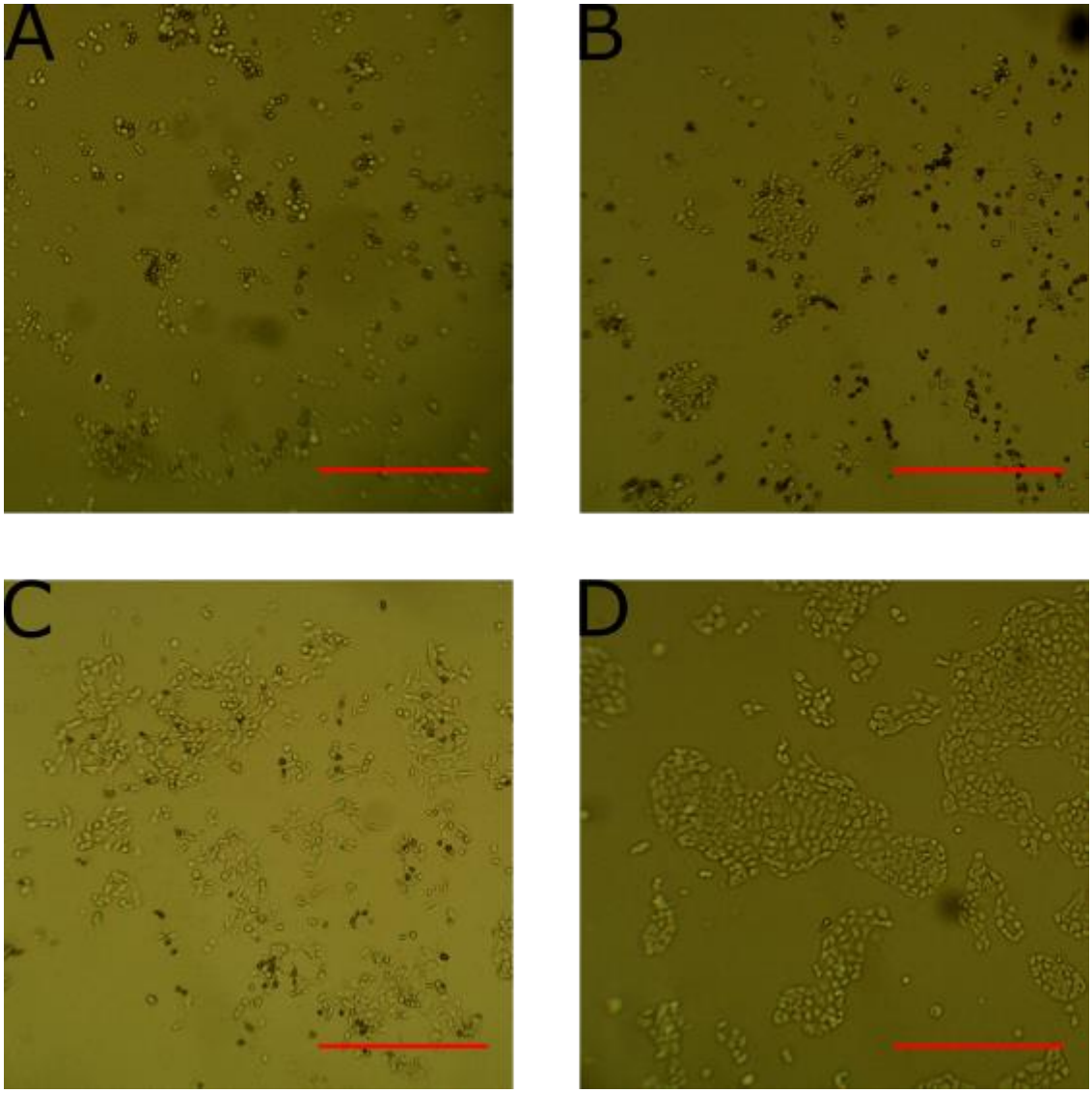

Figure 5.11 - Sections of wells containing UM-SCC-1 p53 WT cells 24 hours after incubation with 0.073 nM AuNP@PAH-RB@PSS for 3 hours and irradiation with; A) 0.05 W for 6 minutes, B) 0.05 W for 4 minutes, C) 0.05 W for 2 minutes and D) no irradiation. Scale bar in all images represents 0.5 mm.

UM-SCC-1 pBABE cells incubated with 0.073 nM AuNP@PAH-RB@PSS for 3 hours were irradiated with 0.05 W for 6, 4 and 2 minutes. These were then assessed using an MTT assay resulting in a viability of 0.33±0.12, 0.48±0.05 and 0.71±0.23, respectively.

A similar trend to that seen in UM-SCC-1 is present in its isogenic cell lines UM-SCC-1 pBABE and UM-SCC-1 p53 WT and can be seen in figure 5.12. Based upon viability alone there is no significant difference between the effect of irradiation on these cell lines at a given fluence.

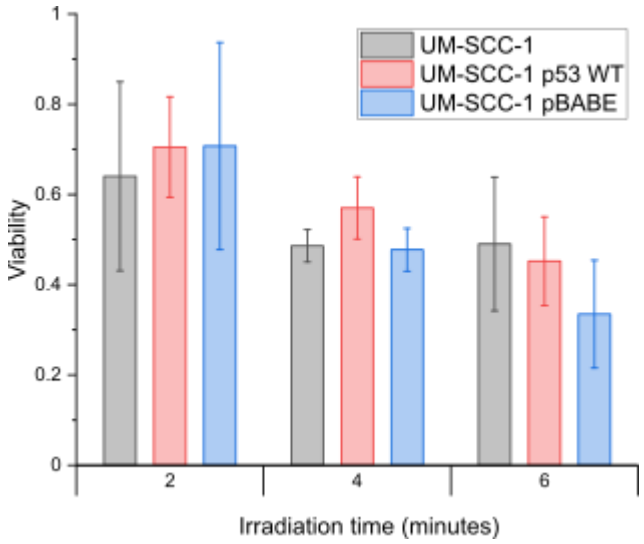

Figure 5.12 – Effect of 0.05 W irradiation on UM-SCC-1 (black), UM-SCC-1 p53 WT (red) and UM-SCC-1 pBABE cells following incubation with 0.073 nM AuNP@PAH-RB@PSS. The bars represent the mean of several experiments and the error bars represent the standard deviation.

However, it must be noted that the different cell lines have significantly different uptake of NP (figure 5.1), and hence the amount of SO generated under the same irradiation conditions varies significantly. When this is accounted for, a significant difference between cell lines emerges. As UM-SCC-1 p53 WT has the lowest uptake per cell of all the cell lines, it becomes clear that far fewer AuNP@PAH-RB@PSS are required in each cell to deliver a fatal dose. UM-SCC-1 pBABE has the highest AuNP@PAH-RB@PSS uptake and requires the most AuNP@PAH-RB@PSS per cell to deliver a toxic dose of singlet oxygen to the cell, this is graphically represented in figure 5.13, which shows (1-viability) scaled by the cellular content of AuNP@PAH-RB@PSS. It should be noted this makes the simplifying assumption that the effect of irradiation is proportional to the amount of $^1O_2$ produced, i.e. the number of AuNP@PAH-RB@PSS present, which is used here solely for the purpose of producing a simplified graph. Clearly the presence of p53 makes the cells much more sensitive to SO/PDT, whereas the "control" cell line PBABE has a similar behaviour (within the experimental uncertainties) to UM-SCC-1 itself.

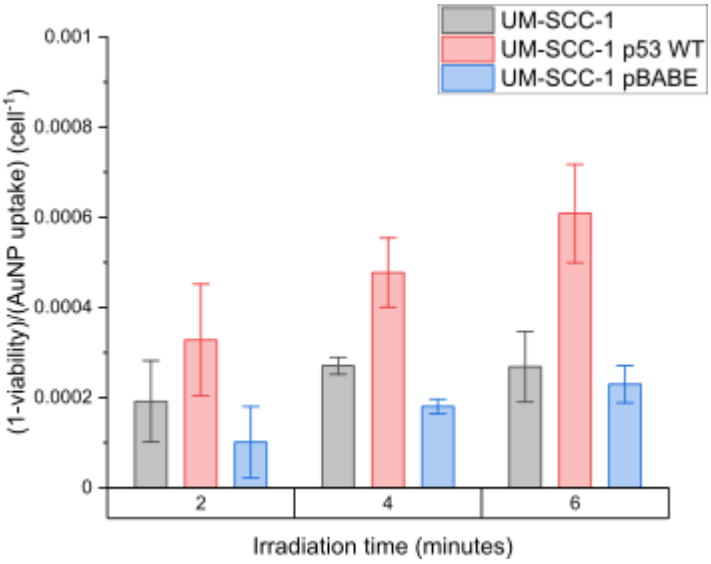

Figure 5.13 – (1-viability)/ (AuNP uptake) in 0.05 W irradiations following incubation with 0.073 nM AuNP@PAH-RB@PSS in; UM-SCC-1 (grey), UM-SCC-1 p53 WT (red) and UM-SCC-1 pBABE (blue) cells. The bars represent the mean of several experiments and the error bars represent the standard deviation.

5.7.2 Discussion

In the context of cancerous cells, the loss of p53 and the tumour supressing function it brings to cells is the most common genetic event for all cancers.[1] More specifically, the loss of the p53 gene means that cells become more reliant on aerobic glycolysis and increased glucose uptake, known as the Warburg effect.[13] This shift in metabolism enables the cell to offset the increased levels of ROS present after tumourgenesis as the glycolytic process increases production of antioxidant intermediates compared to cellular respiration. Considering this, it is not surprising that UM-SCC-1 and UM-SCC-1 pBABE, which are p53 null, are least affected by singlet oxygen mediated photodynamic therapy, requiring more AuNP@PAH-RB@PSS and consequently singlet oxygen production to overcome the increased antioxidant systems present. By contrast, the restoration of the TP53 function in UM-SCC-1 p53 WT leads to increased sensitivity to singlet oxygen as the upregulation of antioxidant systems due to glycolysis is no longer present, so the cells require less AuNP@PAH-RB@PSS to create a cytotoxic dose. This effect is in agreement with studies treating UM-SCC-1, UM-SCC-1 pBABE and UM-SCC-1 p53 WT with ionising radiation (which is ROS mediated), where cytotoxicity was increased in UM-SCC-1, but not in UM-SCC-1 p53 WT, when glycolysis was inhibited.[1]

In addition to the down-regulation of the antioxidant system compared to p53-null cells, TP53 also mediates several apoptic pathways; as the primary route of cell death proposed here is through apoptic pathways, this may play a significant role in the increased effect in cells containing restored p53 function.[14,15] However, despite the lack of p53 in UM-SCC-1 and UM-SCC-1 pBABE, it is significant that AuNP@PAH-RB@PSS mediated PDT still causes cell death, albeit requiring higher doses of singlet oxygen. While TP53 status is strongly linked to apoptosis, there are p53-independent pathways and pro-apoptic proteins can be induced independently of p53.[16–18] As AuNP@PAH-RB@PSS are directly targeted within endosomes and lysosomes, it is possible that a p53 independent apoptic pathway is triggered which is mediated by lysosome permeabilization.[19,20] It has been shown that there is both a p53 dependent and independent apoptic pathway when a lysosome localised photosensitiser is irradiated.[21] In cytotoxic treatments that damage the nucleus and DNA of cells, p53 mediates lysosome permeabilization as part of the apoptic pathway, but it is possible that the AuNP@PAH-RB@PSS PDT treatment is p53 independent.[22]

From our results it is impossible to conclude whether it is the upregulation of apoptosis or downregulation of antioxidant systems in cells containing p53 that increase the efficacy of the photodynamic treatment with AuNP@PAH-RB@PSS. However, clearly the transfection of p53 into cells significantly increases the sensitivity of UM-SCC-1 cells to photodynamic therapy which can be quantified when accounting for the differing uptake between cell lines.

The effect of TP53 status upon PDT treatment has been reported in literature previously, with most research showing that TP53 has significant effect upon cytoxicity.[23–26]. The results presented here show a significant effect by TP53, however significant killing still occurs in p53 null UM-SCC-1 and UM-SCC-1 pBABE. This is in good accordance with the literature reports, however it is significant that at the same dose of light and AuNP@PAH-RB@PSS (during incubation) the cytotoxic effect is indistinguishable and it is only when uptake has been determined that the significant role of TP53 status can be elucidated. While the $^1O_2$ sensitivity may be reduced by the loss of p53, this loss also creates an increased metabolic demand, which offsets the protection offered by the Warburg effect by allowing increased NP uptake.

The 1.9 factor increase in sensitivity to $^1O_2$ we report between UM-SCC-1 and UM-SCC-1 p53 WT in figure 5.13, is similar to values reported in literature for other cell experiments using PS dyes which showed an enhancement of killing ranging from a factor 1.3 to 2.[23–27]

It is well known that HeLa cells are exceptionally robust cells, so the increase of AuNP@PAH-RB@PSS mediated phototoxicity in UM-SCC-1 cells may simply be that the UM-SCC-1 cell line is more susceptible to damage from singlet oxygen. HeLa cells do express WTp53; however, its function is limited by the human papillomavirus HPV-E6 which explains the significant difference in killing between UM-SCC-1 p53 WT and HeLa cells.[28] Despite the differences in viability between the 4 cell lines, there is a strong cytotoxic effect present in all cells. As the HeLa genome is highly varied and in many cases distinct from the human genome due to variation since it was immortalised, it is significant that AuNP@PAH-RB@PSS displays toxicity in UM-SCC-1 cell lines.

5.7.3 Therapeutic Implications

Irradiations of UM-SCC-1 cells incubated with AuNP@PAH-RB@PSS still achieve high levels of cell killing despite the increased protection from the Warburg-type phenotype. As HNSCC cells show an 80% prevalence of TP53 mutations, it is essential that any photodynamic agent can overcome this antioxidant activity, and despite the reduced sensitivity to ROS this is offset by the increased uptake of AuNP@PAH-RB@PSS by p53 null cells. The increased uptake allows a similar effect on viability of treatments at similar AuNP concentrations and provides methods of increasing uptake in cancerous cells compared to the surrounding healthy cells. Cells with increased glycolytic function show increased GLUT transporter activity and so the potential for glucose functionalised AuNPs further enhancing uptake could provide an exceptional method to exploiting the unique dual selectivity of PDT to distinguish between cancerous and healthy cells around the edges of a tumour bed.[29,30]

5.8 Conclusion

The results presented in this chapter show that no significant killing could be observed using AuNP@cit in UM-SCC-1 cells, however a strong cytotoxic effect was reported using AuNP@PAH-RB@PSS.

When applied the treatment against isogenic cells UM-SCC-1 p53 WT and UM-SCC-1 pBABE and the amount of $^1O_2$ required to kill cells was significantly reduced when p53 status was introduced. This may be due to the upregulation of apoptosis or increased sensitivity to $^1O_2$ when cells revert from a glycolytic metabolism (with no p53 function) to a respiration-based metabolism (with reintroduction of p53). This is consistent with literature reports for other PS, however due to the increased uptake of AuNP@PAH-RB@PSS in UM-SCC-1 compared to UM-SCC-1 p53 WT, identical incubation conditions yielded roughly the same toxicity despite the reduced $^1O_2$ sensitivity in UM-SCC-1 cells.

5.9 References

(1) Wilkie, M. D. et al. TP53 Mutations in Head and Neck Cancer Cells Determine the Warburg Phenotypic Switch Creating Metabolic Vulnerabilities and Therapeutic Opportunities for Stratified Therapies. *Cancer Lett.* **2020**, *478* (February), 107–121. https://doi.org/10.1016/j.canlet.2020.02.032.

(2) Haiss, W.; Thanh, N. T. K.; Aveyard, J.; Fernig, D. G. Determination of Size and Concentration of Gold Nanoparticles from UV-Vis Spectra. *Anal. Chem.* **2007**, *79* (11), 4215–4221. https://doi.org/10.1021/ac0702084.

(3) Heiden, M. G. V.; Cantley, L. C.; Thompson, C. B. Understanding the Warburg Effect: The Metabolic Requirements of Cell Proliferation. *Science (80-.).* **2009**, *324* (5930), 1029–1033. https://doi.org/10.1126/science.1160809.

(4) Schwartzenberg-Bar-Yoseph, F.; Armoni, M.; Karnieli, E. The Tumor Suppressor P53 Down-Regulates Glucose Transporters GLUT1 and GLUT4 Gene Expression. *Cancer Res.* **2004**, *64* (7), 2627–2633. https://doi.org/10.1158/0008-5472.CAN-03-0846.

(5) Wartlick, H. et al. Highly Specific HER2-Mediated Cellular Uptake of Antibody-Modified Nanoparticles in Tumour Cells. *J. Drug Target.* **2004**, *12* (7), 461–471. https://doi.org/10.1080/10611860400010697.

(6) Zhang, Y.; Zhang, J. Surface Modification of Monodisperse Magnetite Nanoparticles for Improved Intracellular Uptake to Breast Cancer Cells. *J. Colloid Interface Sci.* **2005**, *283* (2), 352–357. https://doi.org/10.1016/j.jcis.2004.09.042.

(7) Román-Rosales, A. A.; García-Villa, E.; Herrera, L. A.; Gariglio, P.; Díaz-Chávez, J. Mutant P53 Gain of Function Induces HER2 Over-Expression in Cancer Cells. *BMC Cancer* **2018**, *18* (1), 1–12. https://doi.org/10.1186/s12885-018-4613-1.

(8) Campisi, A. et al. Gene Silencing of Transferrin-1 Receptor as a Potential Therapeutic Target for Human Follicular and Anaplastic Thyroid Cancer. *Mol. Ther. - Oncolytics* **2020**, *16* (March), 197–206. https://doi.org/10.1016/j.omto.2020.01.003.

(9) Zhang, F.; Wang, W.; Tsuji, Y.; Torti, S. V.; Torti, F. M. Post-Transcriptional Modulation of Iron Homeostasis during P53-Dependent Growth Arrest. *J. Biol. Chem.* **2008**, *283* (49), 33911–33918. https://doi.org/10.1074/jbc.M806432200.

(10) Funauchi, Y. et al. Regulation of Iron Homeostasis by the P53-ISCU Pathway. *Sci. Rep.* **2015**, *5*, 1–14. https://doi.org/10.1038/srep16497.

(11) Chithrani, B. D.; Ghazani, A. A.; Chan, W. C. W. Determining the Size and Shape Dependence of Gold Nanoparticle Uptake into Mammalian Cells. *Nano Lett.* **2006**, *6* (4), 662–668. https://doi.org/10.1021/nl052396o.

(12) Panzarini, E.; Inguscio, V.; Dini, L. Timing the Multiple Cell Death Pathways Initiated by Rose Bengal Acetate Photodynamic Therapy. *Cell Death Dis.* **2011**,

2 (6), 1–11. https://doi.org/10.1038/cddis.2011.51.

(13) Mantovani, F.; Collavin, L.; Del Sal, G. Mutant P53 as a Guardian of the Cancer Cell. *Cell Death Differ.* **2019**, *26* (2), 199–212. https://doi.org/10.1038/s41418-018-0246-9.

(14) Polyak, K.; Xia, Y.; Zweier, J. L.; Kinzler, K. W.; Vogelstein, B. Letters to Nature A Model for P53-Induced Apoptosis. *Nature* **1997**, *389* (September), 300–305.

(15) Aubrey, B. J.; Kelly, G. L.; Janic, A.; Herold, M. J.; Strasser, A. How Does P53 Induce Apoptosis and How Does This Relate to P53-Mediated Tumour Suppression? *Cell Death Differ.* **2018**, *25* (1), 104–113. https://doi.org/10.1038/cdd.2017.169.

(16) Roos, W. P.; Kaina, B. DNA Damage-Induced Cell Death by Apoptosis. *Trends Mol. Med.* **2006**, *12* (9), 440–450. https://doi.org/10.1016/j.molmed.2006.07.007.

(17) Seol, D. W. P53-Independent up-Regulation of a TRAIL Receptor DR5 by Proteasome Inhibitors: A Mechanism for Proteasome Inhibitor-Enhanced TRAIL-Induced Apoptosis. *Biochem. Biophys. Res. Commun.* **2011**, *416* (1–2), 222–225. https://doi.org/10.1016/j.bbrc.2011.11.053.

(18) Fricker, M.; Papadia, S.; Hardingham, G. E.; Tolkovsky, A. M. Implication of TAp73 in the P53-Independent Pathway of Puma Induction and Puma-Dependent Apoptosis in Primary Cortical Neurons. *J. Neurochem.* **2010**, *114* (3), 772–783. https://doi.org/10.1111/j.1471-4159.2010.06804.x.

(19) Erdal, H. et al. Induction of Lysosomal Membrane Permeabilization by Compounds That Activate P53-Independent Apoptosis. *Proc. Natl. Acad. Sci. U. S. A.* **2005**, *102* (1), 192–197. https://doi.org/10.1073/pnas.0408592102.

(20) Wang, Z. X. et al. Quercetin Induces P53-Independent Cancer Cell Death through Lysosome Activation by the Transcription Factor EB and Reactive Oxygen Species-Dependent Ferroptosis. *Br. J. Pharmacol.* **2021**, *178* (5), 1133–1148. https://doi.org/10.1111/bph.15350.

(21) Kessel, D.; Reiners, J. J. Promotion of Proapoptotic Signals by Lysosomal Photodamage. *Photochem. Photobiol.* **2015**, *91* (4), 931–936. https://doi.org/10.1111/php.12456.

(22) Yuan, X. M. et al. Lysosomal Destabilization in P53-Induced Apoptosis. *Proc. Natl. Acad. Sci. U. S. A.* **2002**, *99* (9), 6286–6291. https://doi.org/10.1073/pnas.092135599.

(23) Fisher, A. M. R.; Rucker, N.; Wong, S.; Gomer, C. J. Differential Photosensitivity in Wild-Type and Mutant P53 Human Colon Carcinoma Cell Lines. *J. Photochem. Photobiol. B Biol.* **1998**, *42* (2), 104–107. https://doi.org/10.1016/S1011-1344(97)00130-9.

(24) Fisher, A. M. R. et al. Increased Photosensitivity in HL60 Cells Expressing Wild-Type P53. *Photochem. Photobiol.* **1997**, *66* (2), 265–270. https://doi.org/10.1111/j.1751-1097.1997.tb08653.x.

(25) Zhang, W. G. et al. Wild-Type P53 Protein Potentiates Phototoxicity of 2-BA-2-DMHA in HT29 Cells Expressing Endogenous Mutant P53. *Cancer Lett.* **1999**, *138* (1–2), 189–195. https://doi.org/10.1016/S0304-3835(99)00013-0.

(26) Tong, Z.; Singh, G.; Rainbow, A. J. The Role of the P53 Tumor Suppressor in the Response of Human Cells to Photofrin-Mediated Photodynamic Therapy. *Photochem. Photobiol.* **2000**, *71* (2), 201. https://doi.org/10.1562/0031-8655(2000)071<0201:trotpt>2.0.co;2.

(27) Barberi-Heyob, M. et al. Wild-Type P53 Gene Transfer into Mutated P53 HT29 Cells Improves Sensitivity to Photodynamic Therapy via Induction of Apoptosis. *Int. J. Oncol.* **2004**, *24* (4), 951–958. https://doi.org/10.3892/ijo.24.4.951.

(28) Landry, J. J. M. et al. The Genomic and Transcriptomic Landscape of a HeLa Cell Line. **2013**, *3* (August), 1213–1224. https://doi.org/10.1534/g3.113.005777.

(29) Motiei, M. et al. Differentiating between Cancer and Inflammation: A Metabolic-Based Method for Functional Computed Tomography Imaging. *ACS Nano* **2016**, *10* (3), 3469–3477. https://doi.org/10.1021/acsnano.5b07576.

(30) Singh, S. Glucose Decorated Gold Nanoclusters: A Membrane Potential Independent Fluorescence Probe for Rapid Identification of Cancer Cells Expressing Glut Receptors. *Colloids Surfaces B Biointerfaces* **2017**, *155*, 25–34. https://doi.org/10.1016/j.colsurfb.2017.03.052.

6 Conclusion

AuNP@cit and novel AuNP@PAH-RB@PSS were synthesised and characterised using UV-vis, ζ-potential and DCS to allow precise determination of the capping layer thickness. Rose Bengal was loaded into the polyelectrolyte PAH through use of EDC chemistry. Despite extensive purification using dialysis, this was unable to separate electrostatically and covalently bound Rose Bengal. The loading of RB did not affect the layer-by-layer coating of AuNP using PAH-RB, however the electrostatically bound Rose Bengal was displaced by the addition of PSS. This resulted in AuNP@PAH-RB@PSS. The synthesis showed characteristic surface charge switching and the amount of Rose Bengal loaded on each AuNP was estimated using DCS.

The effect of 532 nm irradiation on HeLa cells exposed to AuNP@cit and AuNP@CALNN showed two distinctive pathways to cause cell death. Firstly, via photothermal heating of HeLa cells to above a threshold temperature 45-50 °C which occurred when cells contained large amounts of AuNPs. This pathway could be predicted by temperature simulations. The second route takes place when cells do not reach this temperature threshold, and the cellular localisation of AuNPs significantly affects the efficacy of the treatment for this pathway. We suggest that this route is AuNP-mediated PDT, through the generation of $^1O_2$ by AuNPs. There is a large variability of efficacy in this route which we attribute to the heterogeneous nature of cellular uptake of AuNPs. It was shown that the confluency of cell cultures significantly affected their AuNP uptake, and we present a technique for analysing the irradiation results which takes into account the local confluency of cells. It is shown that more densely packed cells, which take up less AuNPs, are less affected by PDT treatment which provides further evidence that cell size plays a key role in determining AuNP uptake.

In order to use more realistic cancer cell lines, we developed a new protocol for irradiation which used lower intensity light and was initially tested on HeLa cells containing AuNP@cit. The effect of irradiation was assessed using a more widely used viability assay, however the lower intensity light necessitated increasing the amount of AuNPs contained in cells to observe a PDT effect. The amount of $^1O_2$ required for inducing cell death was consistent between these two protocols.

The low quantum yield and high heating of these particles limited the PDT effect. In order to increase the PDT effect, AuNP@PAH-RB@PSS were used and their uptake was quantified using ICP-OES. The presence of Rose Bengal on these AuNPs significantly increased the PDT efficiency, with significantly lower irradiation and incubation conditions required for achieving cell killing. The photobleaching of Rose Bengal meant that under most irradiation conditions the key determinant of whether enough $^1O_2$ was generated was the amount of AuNP@PAH-RB@PSS uptake. We were able to successfully model these data, and it was shown that cells exposed to higher concentrations of AuNP@PAH-RB@PSS were significantly more sensitive to PDT than cells containing less AuNPs, even when using significantly higher irradiation intensity.

PDT mediated by AuNP@cit and AuNP@PAH-RB@PSS was used on isogenic cell lines UM-SCC-1, UM-SCC-1 p53 WT and UM-SCC-1 pBABE in order to investigate the role of the p53 gene on the efficacy of PDT. AuNP@cit mediated PDT was unable to affect cells in the conditions used, however AuNP@PAH-RB@PSS PDT was successfully used against all cell lines at the same incubation and irradiation conditions. However, upon determination of AuNP uptake it was shown that UM-SCC-1 p53 WT was significantly more sensitive to $^1O_2$ than UM-SCC-1 and UM-SCC-1 pBABE. We attribute this to the different p53 statuses of the cell lines, which may have implications for it use against tumours. p53 also affects uptake, in a way that counterbalances the increased $^1O_2$ sensitivity. However, this may be due to differences in sub-cellular localisation of AuNPs and so TEM analysis of cells containing these AuNPs would be useful.

The use of AuNPs, both with and without Rose Bengal, show promise for use in PDT. However, we have shown that the cellular localisation of AuNPs plays a key role in the efficacy of PDT. As such, care must be taken in selecting the correct capping layer for different applications to ensure good AuNP internalisation. This could be done via attaching biomarkers such as glucose which are overexpressed by cancerous cells, or by attaching tumour specific antibodies. This would be particularly important for AuNPs without Rose Bengal due to their low quantum yield.

AuNP@PAH-RB@PSS is a promising, cheap and easy to synthesise AuNP, however further work on optimising the synthetic protocol to maximise covalent bonding between PAH and Rose Bengal would increase its efficacy. This could be done by

introducing sulfo-NHS into the EDC coupling reaction, which has been shown to significantly increase the efficacy of coupling. While only 2 polyelectrolyte layers were used in here, it has been shown in literature that up to 20 layers can be added to AuNPs, which could drastically increase the amount of Rose Bengal on each AuNP and would allow lower concentrations or irradiation powers to be used which would be beneficial.

While the heterogeneous nature of AuNP uptake can be accounted for using models, it would be beneficial to quantify the distributions for individual cell lines and AuNPs. This could be done using single cell-ICP which would allow accurate assessment of AuNP uptake of a single cell basis. As well as providing uptake data, the measurement of AuNPs and cell death markers could be combined using mass cytometry or flow cytometry. This would allow the accurate experimental determination of the amount of AuNPs required by cells for killing, and hence the amount $^1O_2$ required to kill cells.

Appendix 1

Beam profile

Firstly, the Gaussian profile of the laser beam can be defined using equation A1, and thus the intensity at distance r from the beam centre at power P can be calculated, where d is the $1/e^2$ diameter,

$$I(r,P) = \frac{8P}{\pi d^2} e^{\frac{-8r^2}{d^2}}$$

Equation A1

Generation of Singlet oxygen by Rose Bengal

The photon flux (photons s^{-1} mm^{-2}) generated by the laser at I(r, P) can be calculated by equation A2, where E is the energy of a photon at wavelength λ, equation A3.

$$Iph(r,P) = \frac{I(r,p)}{E}$$

Equation A2

$$E = \frac{hc}{\lambda}$$

Equation A3

The absorption cross section (mm^{-2}) of Rose Bengal can be calculated by equation A4, where NA is Avogadro's number and ε is the extinction coefficient.

$$\sigma = \frac{\ln(10)}{NA}\varepsilon$$

Equation A4

Thus, the excitation rate of a Rose Bengal molecule at distance r from the beam centre and laser power P, exc(r, P) (s^{-1}), can be calculated by the product of equations A2 and A4.

$$exc(r,P) = Iph(r,P)\,\sigma$$

Equation A5

The amount of $^1O_2$ generated at (r, P) over an irradiation time t, SO(r,P) can be calculated by the product of ΦSO, the quantum yield of singlet oxygen production by Rose Bengal, the excitation rate (A5) and time t. However, the maximum number of excitations of Rose Bengal (maxexc) before it bleaches limits the amount of $^1O_2$ that can be produced, yielding the following equation for SO(r,P):

$$SO(r,P) = \Phi SO \times \min\left(exc\{r,P\}\, t, maxexc\right)$$

Equation A6

Lognormal distribution of AuNP uptake by cells

As shown in the literature, the AuNP uptake is described by a lognormal distribution of AuNPs within a cell population where the mean uptake is NP_per_cell, as defined by equations A7 and A8.[1]

$$Nmax = e^{\ln(NP\_per\_cell) - 0.5w^2}$$

Equation A7

$$f(NP) = \frac{e^{\frac{-(\ln(NP) - \ln(Nmax))^2}{2w^2}}}{NP\, w\sqrt{2\pi}}$$

Equation A8

Determination of cell death

Whether a cell with n AuNPs in it dies when irradiated for a time t at distance r from the beam centre at laser power P, can be determined by calculating the total number of Singlet oxygen produced, equation A9. This combines A6, i.e. the number of $^1O_2$ produced by a single AuNP, with the number of AuNPs within the cell (n) and the number of Rose Bengal molecules per AuNP (RBperNP). If this value exceeds the required $^1O_2$ dose for cell killing, KillingSO, then the cell dies, equation A10.

$$TotalSO(r,n,P) = n\ \ RBperNP\ \ SO(r,P)$$

Equation A9

$$kill(r,n,P) = \begin{cases} 0, & TotalSO(r,n,P) < \text{KillingSO} \\ 1, & TotalSO(r,n,P) \geq \text{KillingSO} \end{cases}$$

Equation A10

Viability

Thus, a theoretical viability can be defined, which calculates the viability of the experimental well with experimental parameters (power (P), $1/e^2$ beam diameter d, well diameter D), ε (extinction coefficient of Rose Bengal), average AuNP uptake per cell and width of the uptake distribution w, maximum excitations of Rose Bengal before bleaching, the required $^1O_2$ dose for killing, and the number of Rose Bengal molecules per AuNP, equation A11. This averages over the full well area, thus accounting for the varying beam intensity, and over all cells with different AuNP uptake.

$$Viability\ (P) = 1 - \frac{2\pi \int_0^{D/2} \int_0^{\infty} kill(r, NP, P) f(NP)\ \boldsymbol{d}NP\ r\ \boldsymbol{d}r}{\pi(\frac{D}{2})^2}$$

Equation A11

Use of this model in AuNP@cit

In order to model the effect of AuNP@cit, ε and ΦSO are changed to appropriate values for AuNP@cit. The amount of $^1O_2$ generated at (r, P) over an irradiation time t, SO(r,P) can be calculated by the product of ΦSO, the quantum yield of singlet oxygen production by AuNP@cit, the excitation rate (A5) and time t, equation A12. As AuNPs are photostable there is no limitation on the number excitations.

$$SO(r, P) = \Phi SO\ exc(r, P)\ t$$

Equation A12

As there the AuNP acts as the PS, equation A9 can be simplified as the number of Rose Bengal molecules per AuNP is no longer needed, equation A13.

$$TotalSO(r, n, P) = n\ \ SO(r, P)$$

Equation A13

This can then be applied described above in equation A10 and A11 to define a theoretical viability.

References

(1) Jeynes, J. C. G.; Jeynes, C.; Merchant, M. J.; Kirkby, K. J. Measuring and Modelling Cell-to-Cell Variation in Uptake of Gold Nanoparticles. *Analyst* **2013**, *138* (23), 7070. https://doi.org/10.1039/c3an01406a.